REPORT DOCUMENTATION PAGE		Form Approved OMB NO. 0704-0188

The public reporting burden for this collection of information is estimated to average 1 hour per response, including the time for reviewing instructions, searching existing data sources, gathering and maintaining the data needed, and completing and reviewing the collection of information. Send comments regarding this burden estimate or any other aspect of this collection of information, including suggesstions for reducing this burden, to Washington Headquarters Services, Directorate for Information Operations and Reports, 1215 Jefferson Davis Highway, Suite 1204, Arlington VA, 22202-4302. Respondents should be aware that notwithstanding any other provision of law, no person shall be subject to any oenalty for failing to comply with a collection of information if it does not display a currently valid OMB control number.
PLEASE DO NOT RETURN YOUR FORM TO THE ABOVE ADDRESS.

1. REPORT DATE (DD-MM-YYYY)	2. REPORT TYPE	3. DATES COVERED (From - To)
12-09-2010	Final Report	1-Jun-2004 - 30-Nov-2008

4. TITLE AND SUBTITLE	5a. CONTRACT NUMBER
Final Report: Development of Vector Parabolic Equation Technique for Propagation in Urban and Tunnel Environments	W911NF-04-1-0228
	5b. GRANT NUMBER
	5c. PROGRAM ELEMENT NUMBER
	611102

6. AUTHORS	5d. PROJECT NUMBER
Ramakrishna Janaswamy	
	5e. TASK NUMBER
	5f. WORK UNIT NUMBER

7. PERFORMING ORGANIZATION NAMES AND ADDRESSES	8. PERFORMING ORGANIZATION REPORT NUMBER
University of Massachusetts - Amherst Office of Grant & Contract Admin. 408 Goodell Building Amherst, MA 01003 -3285	

9. SPONSORING/MONITORING AGENCY NAME(S) AND ADDRESS(ES)	10. SPONSOR/MONITOR'S ACRONYM(S)
U.S. Army Research Office P.O. Box 12211 Research Triangle Park, NC 27709-2211	ARO
	11. SPONSOR/MONITOR'S REPORT NUMBER(S)
	45599-EL.1

12. DISTRIBUTION AVAILIBILITY STATEMENT
Approved for Public Release; Distribution Unlimited

13. SUPPLEMENTARY NOTES
The views, opinions and/or findings contained in this report are those of the author(s) and should not contrued as an official Department of the Army position, policy or decision, unless so designated by other documentation.

14. ABSTRACT

A vector version of parabolic equation (PE) was used to study the 3D propagation of electromagnetic waves in enclosed structures such as tunnels. The tunnels walls could be lossy, rough, gently curved, or branched. The PE was solved numerically by adopting the Alternate Direction Implicit finite difference technique. Extensive comparisons with experimental results conducted by other researchers were carried out to elaborate on the accuracy and limitations of the technique.

15. SUBJECT TERMS
Parabolic Equation, Electromagnetic Wave Propagation, Tunnels, Transform Techniques, Stochastic Techniques

16. SECURITY CLASSIFICATION OF:			17. LIMITATION OF ABSTRACT	15. NUMBER OF PAGES	19a. NAME OF RESPONSIBLE PERSON
a. REPORT	b. ABSTRACT	c. THIS PAGE			Ramakrishna Janaswamy
UU	UU	UU	UU		19b. TELEPHONE NUMBER
					413-545-0937

Final Report: Development of Vector Parabolic Equation Technique for Propagation in Urban and Tunnel Environments

ABSTRACT

A vector version of parabolic equation (PE) was used to study the 3D propagation of electromagnetic waves in enclosed structures such as tunnels. The tunnels walls could be lossy, rough, gently curved, or branched. The PE was solved numerically by adopting the Alternate Direction Implicit finite difference technique. Extensive comparisons with experimental results conducted by other researchers were carried out to elaborate on the accuracy and limitations of the technique.

The angular correlation of received fields in 2D multipath environments was studied through full-wave Monte Carlo simulations. The results showed that the uncorrelated scattering assumption remains valid for the discrete finite spectra when the scattering objects are distributed randomly and that the correlation among wave components from different angles increases only when the randomness of the scatterer distribution is reduced.

Separately, expressions for the transitional probabilities for a four-state random walk (FRW) that is used to solve the PE in free-space and with material boundaries were derived by using transform techniques. An absorbing boundary condition for use with the FRW was also derived using transform techniques. Appropriateness of the random walk technique for wave propagation problems was demonstrated.

List of papers submitted or published that acknowledge ARO support during this reporting period. List the papers, including journal references, in the following categories:

(a) Papers published in peer-reviewed journals (N/A for none)

R. Martelly and R. Janaswamy, ``Modeling radio transmission loss in curved, branched and rough-walled tunnels with the ADI-PE method,'' IEEE Trans. Antennas Propagat., vol. 58(6), pp. 2037-2045, June 2010.

J. Xu and R. Janaswamy, ``Angular correlation properties with random multiple scattering,'' IEEE Trans. Signal Proccessing, vol. 57(7), pp. 2651-2659, July 2009.

R. Martelly and R. Janaswamy, ``An ADI-PE approach for modeling radio transmission loss in tunnels,'' IEEE Trans. Antennas Propagat., vol. 57(6), pp. 1759-1770, June 2009.

R. Janaswamy, ``Transitional probabilities for the four-state random walk on a lattice in the presence of partially reflecting boundaries,'' J. Mathematical Physics, vol. 50(5), Pages: 053301 (11 pp), May 2009.

R. Janaswamy, ``Transparent boundary condition for the parabolic equation modeled by the 4RW,'' IEEE Antennas Wireless Propagat. Lett., vol. 8, pp. 23-26, 2009.

R. Janaswamy, ``Transitional probabilities for the 4-state random walk on a lattice,'' J. Phys. A: Math. Theor., vol. 41, Pages: 155306 (11pp), April 2008.

Number of Papers published in peer-reviewed journals: 6.00

(b) Papers published in non-peer-reviewed journals or in conference proceedings (N/A for none)

Number of Papers published in non peer-reviewed journals: 0.00

(c) Presentations

R. Janaswamy, ``A four state random walk technique for treating the parabolic equation," 2009 Joint IEEE International Symposium/URSI National Radio Science Meeting, Charleston, SC, 2009.

Number of Presentations: 1.00

Non Peer-Reviewed Conference Proceeding publications (other than abstracts):

Number of Non Peer-Reviewed Conference Proceeding publications (other than abstracts):   0

Peer-Reviewed Conference Proceeding publications (other than abstracts):

R. Martelly and R. Janaswamy, ``Propagation prediction in rough and branched tunnels by the ADI-PE techniqu,'' IEEE International Conference on Electromagnetics in Advanced Applications, ICEAA '09., Digital Object Identifier: 10.1109/ICEAA.2009.5297359, Publication Year: 2009 , Page(s): 596 - 599.

R. Martelly and R. Janaswamy, ``Propagation in tunnels using the parabolic equation and the ADI technique,'' IEEE Antennas and Propagation Society International Symposium, Digital Object Identifier: 10.1109/APS.2007.4395426, Publication Year: 2007 , Page(s): 45 - 48.

R. Janaswamy, ``Solution of BVPs in electrodynamics by stochastic methods,''
IEEE Applied Electromagnetics Conference, Digital Object Identifier: 10.1109/AEMC.2007.4638046, Publication Year: 2007 , Page(s): 1 - 4.

Number of Peer-Reviewed Conference Proceeding publications (other than abstracts):   3

(d) Manuscripts

Number of Manuscripts: 0.00

Patents Submitted

Patents Awarded

Graduate Students

NAME	PERCENT_SUPPORTED
Richard Martelly	0.80
Jie Xu	0.05
FTE Equivalent:	**0.85**
Total Number:	**2**

Names of Post Doctorates

NAME	PERCENT_SUPPORTED
FTE Equivalent:	
Total Number:	

Names of Faculty Supported

NAME	PERCENT_SUPPORTED	National Academy Member
Ramakrishna Janaswamy	0.08	No
FTE Equivalent:	**0.08**	
Total Number:	**1**	

Names of Under Graduate students supported

NAME	PERCENT SUPPORTED

FTE Equivalent:
Total Number:

Student Metrics
This section only applies to graduating undergraduates supported by this agreement in this reporting period

The number of undergraduates funded by this agreement who graduated during this period: 0.00

The number of undergraduates funded by this agreement who graduated during this period with a degree in science, mathematics, engineering, or technology fields:...... 0.00

The number of undergraduates funded by your agreement who graduated during this period and will continue to pursue a graduate or Ph.D. degree in science, mathematics, engineering, or technology fields:...... 0.00

Number of graduating undergraduates who achieved a 3.5 GPA to 4.0 (4.0 max scale): 0.00

Number of graduating undergraduates funded by a DoD funded Center of Excellence grant for Education, Research and Engineering: 0.00

The number of undergraduates funded by your agreement who graduated during this period and intend to work for the Department of Defense 0.00

The number of undergraduates funded by your agreement who graduated during this period and will receive scholarships or fellowships for further studies in science, mathematics, engineering or technology fields: 0.00

Names of Personnel receiving masters degrees

NAME

Total Number:

Names of personnel receiving PHDs

NAME
Richard Martelly
Jie Xu

Total Number: 2

Names of other research staff

NAME	PERCENT SUPPORTED

FTE Equivalent:
Total Number:

Sub Contractors (DD882)

Solution of BVPs in Electrodynamics by Stochastic Methods

(Invited Paper)

R. Janaswamy

Department of Electrical & Computer Engineering
University of Massachusetts, Amherst, MA 01002, USA. Email: janaswamy@ecs.umass.edu

Abstract—Field computation by the stochastic differential equation (SDE) method is demonstrated for electrostatic and electrodynamic propagation problems by considering simple examples. The solution to the inhomogeneous Helmholtz equation is first related to that a Schrödinger type of equation (parabolic in nature) by means of Laplace transformation. The SDE method is directly applied to this parabolic equation. Presence of the imaginary term in the parabolic equation warrants analytic continuation into the complex space that is addressed in this paper.

I. Introduction

SDE methods are alternative methods that are available for field computation and have not been explored to the full extent yet. Initial efforts for solving the Helmholtz equation are given in [1] and [2], although the approach of the latter is limited to low wavenumbers and that of the former is geared towards determining the transport amplitude, having found the eikonal by some other means. Among the principal advantages of the stochastic method considered in this paper are that (i) it requires no meshing, (ii) the field at a point can be determined without the knowledge of the field at the neighboring points, (iii) it is ideal for parallel computation, and (iv) it is very stable for low frequencies. The primary disadvantage of the method is that it is not computationally effective on serial machines compared to the traditional methods. We first discuss a brief theory of the method and demonstrate it for electrodynamic case by considering the Schrödinger type of parabolic wave equation that is encountered in wave propagation problems over terrain.

II. Theory

A. Brownian Motion

A one-dimensional normalized Brownian motion or Wiener process is a continuous stochastic process W_t (W as a function of t), $t > 0$ describing the motion of a particle in a dynamical system and satisfying (i) $W_0 = 0$, (ii) for any $0 \leq t_0 < t_1 < \cdots < t_n$, the random variables $W_{t_k} - W_{t_{k-1}}$ are independent, $1 \leq k \leq n$, and (iii) if $0 \leq s \leq t$, $W_t - W_s$ is normally distributed with $\mathcal{E}[W_t - W_s] = 0$, $\mathcal{E}[W_t - W_s]^2 = (t - s)$, where $\mathcal{E}$ stands for expectation [5]. Equivalently, the transitional probability density function for a particle starting at position x and ending up at position y in a time interval t is $p(t; x, y) = \frac{1}{(2\pi t)^{1/2}} e^{-\frac{|x-y|^2}{2t}}, x, y \in R^1, t > 0$ and $|x - y|$ is the Euclidean distance between x and y. Hence the variance of the particle displacement increases linearly with time. An r-dimensional Brownian motion $\boldsymbol{W}_t = [W_t^1, \ldots, W_t^r]'$, where $'$ denotes transpose, consisting of r independent, one-dimensional Brownian motions is defined with respect to the time-homogeneous transitional density

$$p(t; \boldsymbol{x}, \boldsymbol{y}) = \frac{1}{(2\pi t)^{r/2}} e^{-\frac{|\boldsymbol{x}-\boldsymbol{y}|^2}{2t}}, \quad \boldsymbol{x}, \boldsymbol{y} \in R^r, t > 0, \quad (1)$$

B. The Ito Formula and the Feynman-Kac Formula

If $\boldsymbol{X}_t = (X_t^1, X_t^2, \ldots, X_t^r)'$ satisfies the SDE $d\boldsymbol{X}_t = \boldsymbol{\Phi}(t, \boldsymbol{X}_t) d\boldsymbol{W}_t + \boldsymbol{\psi}(t, \boldsymbol{X}_t) dt$, where the matrix $\boldsymbol{\Phi}(t, \boldsymbol{x}) = \{\Phi_k^j(t, \boldsymbol{x})\}$ and the vector $\boldsymbol{\psi}(t, \boldsymbol{x}) = \{\psi^j(t, \boldsymbol{x})\}$, then for a function $f(t, \boldsymbol{x})$ differentiable once in t and twice in $\boldsymbol{x}$, Ito formula states that [3]

$$
\begin{aligned}
df(t, X_t) = &\left[\frac{\partial}{\partial t} + \frac{1}{2} \sum_{j,k,l=1}^{r} \Phi_l^j(t, X_t) \Phi_l^k(t, X_t) \right. \\
&\left. \frac{\partial^2}{\partial x^j \partial x^k} + \sum_{j=1}^{r} \psi^j \frac{\partial}{\partial x^j} \right] f(t, X_t) \, dt \\
&+ \sum_{j,k=1}^{r} \Phi_k^j(t, X_t) \frac{\partial f(t, X_t)}{\partial x^j} dW_t^k, \quad (2)
\end{aligned}
$$

where we have used the following results: $\mathcal{E}(dW_t^j) = 0$, $\mathcal{E}(dW_t^j dt) = 0$, $\mathcal{E}(dW_t^j)^2 = dt$, $\mathcal{E}(dW_t^j dW_t^k) = 0, j \neq k$. Ito formula applied directly to the solution

$u(t, \boldsymbol{x})$ of the initial value problem

$$
\begin{aligned}
\frac{\partial u}{\partial t} &= \frac{1}{2}\sum_{j,k=1}^{r} a_k^j(\boldsymbol{x})\frac{\partial^2 u}{\partial x^j \partial x^k} + \sum_{j=1}^{r}\psi^j(\boldsymbol{x})\frac{\partial u}{\partial x^j} \\
&+ c(\boldsymbol{x})u, \qquad u(0,\boldsymbol{x}) = f(\boldsymbol{x}),
\end{aligned} \tag{3}
$$

where the matrix $\{a_k^j\} = \boldsymbol{\Phi}\boldsymbol{\Phi}'$, together with the SDE $d\boldsymbol{X}_s^{\boldsymbol{x}} = \boldsymbol{\Phi}(\boldsymbol{X}_s^{\boldsymbol{x}})d\boldsymbol{W}_s + \psi(\boldsymbol{X}_s^{\boldsymbol{x}})dt$, $\boldsymbol{X}_0^{\boldsymbol{x}} = \boldsymbol{x} \in R^r$ leads to the Feynman-Kac formula

$$
u(t,\boldsymbol{x}) = \mathcal{E}_x\left[f(\boldsymbol{X}_t^{\boldsymbol{x}}) \exp\left\{ \int_0^t c(\boldsymbol{X}_s^{\boldsymbol{x}})\,ds \right\} \right], \tag{4}
$$

where $\mathcal{E}_x$ is the expectation operator conditioned on keeping $\boldsymbol{x}$ fixed.

C. Initial Boundary Value Problem

If the problem in (3) is supplemented with the Dirichlet condition $u(t,\boldsymbol{x}) = g(t,\boldsymbol{x})$ on the boundary ∂D of a closed domain D, then application of the Feynman-Kac formula to the extended space-time boundary $t = 0$ plus ∂D yields

$$
\begin{aligned}
u(t,\boldsymbol{x}) = \mathcal{E}_x\Bigg[&\Xi_{\tau_t = t}\, f(\boldsymbol{X}_t^{t,\boldsymbol{x}}) \exp\left\{ \int_0^t c(\boldsymbol{X}_s^{t,\boldsymbol{x}})\,ds \right\} \\
&+ \Xi_{\tau_t \neq t}\, g(\tau^{t,\boldsymbol{x}}, \boldsymbol{X}_{\tau^{t,\boldsymbol{x}}}^{t,\boldsymbol{x}}) \exp\left\{ \int_0^{\tau^{t,\boldsymbol{x}}} c(\boldsymbol{X}_s^{t,\boldsymbol{x}})\,ds \right\} \Bigg]
\end{aligned} \tag{5}
$$

where $\Xi_{[\cdot]}$ is the indicator function for the set $[\cdot]$, $\tau^{t,\boldsymbol{x}} = \min\{s : \boldsymbol{X}_s^{t,\boldsymbol{x}} \in \partial D\}$, $\tau_t = \min(t, \tau^{t,\boldsymbol{x}})$, $\boldsymbol{X}_0^{t,\boldsymbol{x}} = \boldsymbol{x}$, and the time counter for the stochastic process is taken as $t_s^{t,\boldsymbol{x}} = t - s$. The conditions under which formulas (4) and (5) hold are discussed in detail in [3]. It is also reasonable to expect these formulas to be valid for complex spatial coordinates assuming analyticity of fields [1]. Essentially, what (5) says is that one first starts a random process $\boldsymbol{X}_t^{t,\boldsymbol{x}}$ at $(t,\boldsymbol{x})$ having a drift component dictated by ψ and a Brownian component dictated by the matrix $\boldsymbol{\Psi}$. If the process hits the boundary ∂D at $\tau^{t,\boldsymbol{x}}$ before the time t at which the solution in sought, a partial contribution comes from the boundary value $g(\tau^{t,\boldsymbol{x}}, \boldsymbol{X}_{\tau^{t,\boldsymbol{x}}}^{t,\boldsymbol{x}})$. On the other hand, if the boundary is not intercepted before t, then a partial contribution comes from the initial value $f(\boldsymbol{X}_t^{t,\boldsymbol{x}})$. The process is then repeated for multiple realizations starting at $(t,\boldsymbol{x})$ and an average taken to yield the solution $u(t,\boldsymbol{x})$. Even though the governing equations encountered in electrostatics and electrodynamics do not necessarily take the form of (3), they can be made to resemble it [4] by employing Laplace

transformation. For example, the electrostatic potential $u(\boldsymbol{x})$ that satisfies the Poisson equation $\nabla^2 u = -f(\boldsymbol{x})$ together with the boundary value $\psi(\boldsymbol{x})$ can be written in terms of an auxiliary function $K(t,\boldsymbol{x})$ as $u(\boldsymbol{x}) = \int_0^\infty K(t,\boldsymbol{x})\,dt$. The equation satisfied by K for $t > 0$ and its initial, boundary values are

$$
\frac{\partial K}{\partial t} = \frac{1}{2}\nabla^2 K, \quad K(t, \boldsymbol{x} \in \partial D) = \psi(\boldsymbol{x}) \tag{6}
$$

$$
K(t = 0^+, \boldsymbol{x}) = \frac{1}{2}f(\boldsymbol{x}). \tag{7}
$$

In this case, formula (5) yields the solution of the Poisson equation as

$$
u(\boldsymbol{x}) = \mathcal{E}_x\left[\psi(\boldsymbol{X}_{\tau_D^x}^x) + \int_0^{\tau_D^x} f(\boldsymbol{X}_t^x)\,dt \right], \tag{8}
$$

where $\tau_D^{\boldsymbol{x}}$ is the first exit time of $X_t^{\boldsymbol{x}}$ from the domain D (see Fig. 1). Similarly, solution of the inhomogeneous
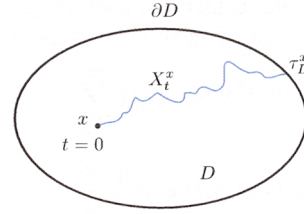

Fig. 1. Interior domain D bounded by a boundary ∂D.

Helmholtz equation $\nabla^2 u + k^2 u = -f$ can be related to the propagator K via

$$
u(\boldsymbol{x}) = \int_0^\infty K(t,\boldsymbol{x})e^{\alpha k^2 t/2}\,dt, \tag{9}
$$

where the propagator satisfies the equation

$$
\frac{\partial K}{\partial t} = \frac{\alpha}{2}\nabla^2 K, \; t > 0, \qquad K(0,\boldsymbol{x}) = \frac{\alpha}{2}f(\boldsymbol{x}) \tag{10}
$$

and α is an appropriately chosen complex constant.

III. Example Calculations

A. Electrostatic Potential

Figure 2 shows the electrostatic potential distribution inside a rectangular region where the potential on the left wall is specified as 10 volts and the potential at the other walls is specified as 0 volts. Comparison is shown between the analytical solution and the stochastic

solution that is obtained with $N_r = 3,000$ realizations. The random process is approximated as $X^x_{t+\Delta t} = X^x_t + \sqrt{\Delta t}\,\gamma$, where γ is a zero mean, unit variance Gaussian random variable. A good agreement is seen between the two. The electrostatic solution is rather insensitive to the time step Δt and the solution shown uses $\Delta t = 0.25$ units.[1]

(a) Analytical Solution

$N_r = 3,000, \Delta t^{1/2} = \min [\Delta x(r), \Delta y(r), 0.5]$
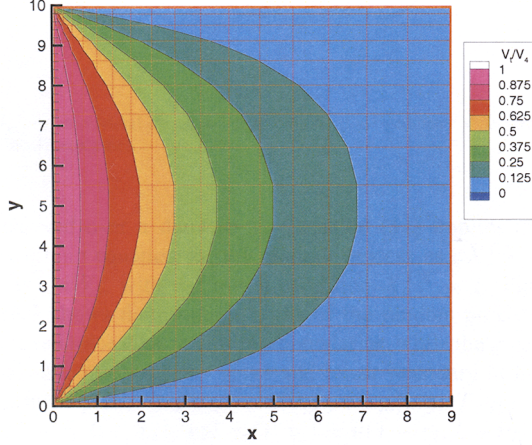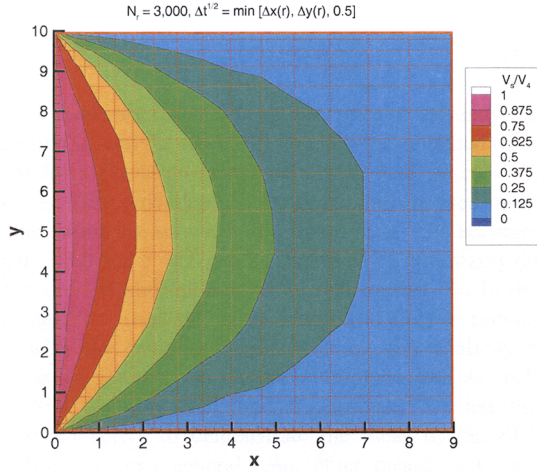
(b) Stochastic Solution

Fig. 2. Potential distribution inside a square region.

B. Propagation Inside a Parallel Plate Waveguide

For the electrodynamic case, we will consider a problem where an equation of the type (10) occurs naturally when (i) paraxial propagation is considered, and (ii) back scattering is neglected. Consider propagation of time-harmonic waves inside an infinite parallel plate waveguide with perfectly conducting boundaries at $x = 0$ and $x = L$. This model problem approximately describes propagation over a conducting ground with a periodic condition enforced at a large height L. The more general case of an impedance boundary condition [6] can be handled using the same ideas. Let the axis of the waveguide be designated as t. Assuming an $e^{i\omega\tau}$ convention in the time variable τ and paraxial propagation, the reduced field $u(t,x) = v(t,x)\exp\left(-ik_0 t\right)$ satisfies the standard parabolic equation

$$\frac{\partial u}{\partial t} = \frac{i}{2k_0}\frac{\partial^2 u}{\partial x^2}, \tag{11}$$

where $v(t,x)$ is the true field and k_0 is the wavenumber. If $u(0,x) = u_0(x)$, then the field at any distance along the guide with $k_n = n\pi/L$ is given by

$$u(t,x) = \sum_{n=0}^{\infty} U_0(k_n)e^{-ik_n^2 t/2k_0}\sin(k_n x), \tag{12}$$

$$U_0(k_n) = \frac{2}{L}\int_0^L u_0(x)\sin(k_n x)\,dx. \tag{13}$$

If the upper limit in the summation in (12) is truncated to N and the integral is approximated by a Riemann sum on a uniform grid of size $\Delta x = L/N$, then the relation between $u_0(n\Delta x)$ and $U_0(k_n)$ will be that of Fourier sine series [6]. The expression for $u(t,x)$ in (12) can be analytically continued to complex space by writing $x = \xi + i\eta$. The boundaries $x = 0$ and $x = L$ can also be analytically continued to $x = 0 + i\eta$, $x = L + i\eta$ respectively. The field on the analytically continued upper and lower boundaries is then

$$u(t, 0 + i\eta) = i\sum_{n=0}^{\infty} U_0(k_n)e^{-ik_n^2 t/2k_0}\sinh(k_n\eta) \tag{14}$$

$$u(t, L + i\eta) = i\sum_{n=0}^{\infty}(-1)^n U_0(k_n)e^{-ik_n^2 t/2k_0}\sinh(k_n\eta) \tag{15}$$

which are seen to depend on the axial distance t. Also note that the field is no longer the same on the upper and lower boundaries in the complex plane. For the current problem it is desirable to find the solution $u(T,\xi)$ (see Fig. 3). The random process is started at (ξ, T) and is
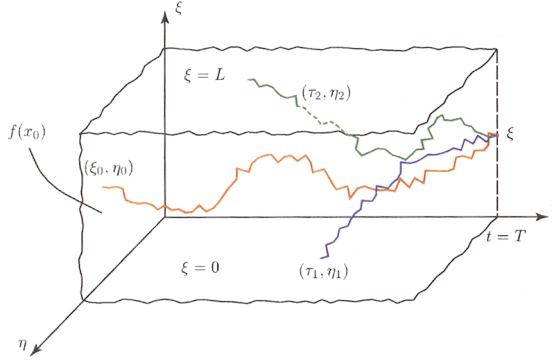
Fig. 3. Analytical continuation of parallel plate geometry with three typical trajectories.

Fig. 4. Field at a distance of 50λ from an aperture source.

observed over a duration T. Equation (11) implies the governing equation for the random process as $dX_s^{T,\xi} = \sqrt{i/k_0}dW_s$, with the initial condition $X_0^{T,\xi} = \xi$. Figure 3 shows three sample paths of the random process. The red trace does not hit any boundaries, while the green and blue traces hit the upper and lower boundary in the complex plane. If $f(x_0) = u(0, \xi_0 + i\eta_0)$, $g_1(T, \eta_1) = u(T - \tau_1, 0 + i\eta_1)$, and $g_2(T, \eta_2) = u(T - \tau_2, L + i\eta_2)$, then the solution can be expressed as

$$u(T,x) = \mathcal{E}_x \left\{ \Xi_{s \in T} f(x_0) + \Xi_{s \in \tau_1} g_1(T, \eta_1) + \Xi_{s \in \tau_2} g_2(T, \eta_2) \right\} \quad (16)$$

Fig. 4 shows the real and imaginary parts of the analytical solution u_e and the stochastic solution, u_n obtained using (16) for a Gaussian initial field with peak at $x = H_t$ and standard deviation σ_x. Other parameters used in the computation are shown in the figure inset. The accuracy near $\xi = 0$ and $\xi = L$ can be improved by optimizing the time step Δt and the number of realizations N_r. In this example, we used the exact solution in (12) to provide us with the boundary conditions on the analytically continued geometry in the complex plane, and as such, the SDE solution is redundant. However, we use this approach solely to demonstrate the ideas of the SDE method. In more general case, other means may have to be found for specifying the boundary conditions on the analytically continued boundaries.

IV. Summary

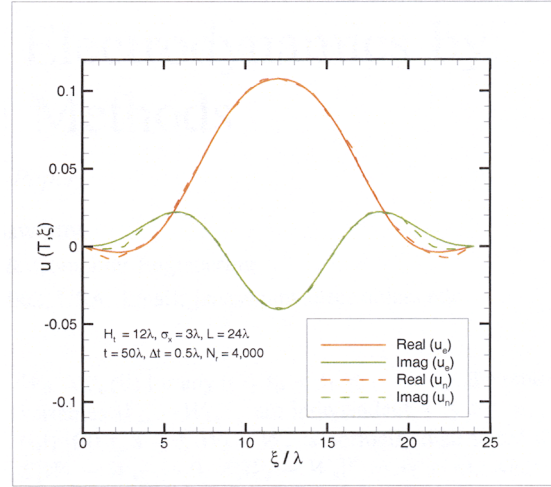A theory of solving the Laplace and Helmholtz equations using the SDE approach has been presented. Favorable comparisons for potential calculations in electrostatics and field calculations in electrodynamics have been shown by analytical continuation methods. The electrostatic solution is rather insensitive to the time-stepping Δt used for Brownian motion, but the electrodynamic case needs more careful choice. More complex problems will be considered in the future.

Acknowledgment

References

[1] B. V. Budaev and D. B. Bogy, "Application of random walk methods to wave propagation," *Quart. J. Appl. Math.*, vol. 55(2), pp. 206-226, 2002.

[2] M. K. Chati, M. D. Grigoriu, S. S. Kulkarni, and S. Mukherjee, "Random walk method for the two- and three-dimensional Laplace, Poisson and Helmholtz equations," *Int. J. Num. Meth. Engr.*, vol. 51, pp. 1133-1156, 2001.

[3] M. Freidlin, *Functional Integration and Partial Differential Equation*, Princeton, NJ: Princeton University Press, 1985.

[4] S. W. Lee, "Path integrals for solving some electromagnetic edge diffraction problems," *J. Math, Phys.*, vol. 19(6), pp. 1414-1422, June 1978.

[5] I. Karatzas and S. E. Shreve, *Brownian Motion and Stochastic Calculus,*, 2nd Ed., New York: Springer, 1998.

[6] J. R. Kuttler and R. Janaswamy, "Improved Fourier transform methods for solving the parabolic wave equation," *Radio Science*, vol. 37(2), RS002488, pp. 5.1-5.11, 2002.

Propagation in Tunnels Using the Parabolic Equation and the ADI Technique

Richard Martelly and Ramakrishna Janaswamy

The University of Massachusetts, Amherst, MA, 01003,

rmartell,janaswamy@ecs.umass.edu

Introduction

The parabolic equation has been shown to accurately model electromagnetic fields in tunnels for waves which travel within $\pm 15^o$ to the axis of propagation [1]. The Crank-Nicolson method is a popular finite difference method that has been used to numerically model radio wave propagation in tunnels. The popularity of the CN method is due to the fact that it is stable for any discretization in the transverse plane or along the propagation axis [2]. The major limitation of the CN method is that it requires the solution of sets of simultaneous equations that may become too large to efficiently solve for problems with dense meshes. The alternate direction implicit (ADI) technique is another unconditionally stable FDM which addresses the problem of computational efficiency. This paper presents results showing the accuracy of the ADI technique when used to model the parabolic equation for (a) square (b) circular and (c) semi-circular cylindrical PEC tunnels. For each tunnel, we compare the numerical solution with the known anlytical solution for different descretizations along the transverse plane and propagation axis.

Alternate Direction Implicit Method

The alternate direction implicit method is a modification of the Crank-Nicolson method that can be used to numerically solve for the scalar parabolic equation [2]

$$\frac{\partial u}{\partial z} = \frac{1}{2jk_o}\left(\frac{\partial^2}{\partial x^2} + \frac{\partial^2}{\partial y^2}\right)u \tag{1}$$

where $u(x,y,z)$ is the reduced plane wave solution and is related to the scalar potential, given by $\Psi(x,y,z) = u(x,y,z)e^{-jk_oz}$ [3].The ADI method reduces the discretized two dimensional problem into a succession of many one dimensional problems [2] with the formulation

$$\left(1 - \frac{r}{4jk_o}\delta_x\right)\tilde{u}^{n+1/2} = \left(1 + \frac{r}{4jk_o}\delta_y\right)u^n \tag{2}$$

$$\left(1 - \frac{r}{4jk_o}\delta_y\right)u^{n+1} = \left(1 + \frac{r}{4jk_o}\delta_x\right)\tilde{u}^{n+1/2} \tag{3}$$

where $(\delta_x u_{m,l} = u_{m+1,l} - 2u_{m,l} + u_{m-1,l})$, $(\delta_y u_{m,l} = u_{m,l+1} - 2u_{m,l} + u_{m,l-1})$ and u^n represents the known field, $\tilde{u}^{n+1/2}$ is the unknown virtual field, and u^{n+1} is the unknown physical field located at $m\Delta x$ and $l\Delta y$ in a cartesian mesh. Combined, Equations (2) and (3) are known as the Peaceman-Rachford equations. The unknowns of the intermediate plane can be solved using Ny-1 matrices of rank (N_x+1), and the unknowns of the $n+1^{th}$ plane can be solved using Nx-1 matrices of rank

$(N_y + 1)$. Using the Crank-Nicolson method, the size of the matrix generated will be $(N_x + 1)(N_y + 1)$ and its elements will not be in tridiagonal or in banded form. As a result, the ADI technique will be more efficient and solve dense mesh problems faster. One difficulty with the ADI technique is that the virtual $\tilde{u}^{n+1/2}$ field has special boundary conditions which may not be the same as the physical boundary conditions. For our following examples, however, we employ the same boundaries for the virtual and physical fields.

Waveguide examples using the ADI method

In the following sections, we will use the ADI method to solve for fields in square, circular and semi-circular cylindrical waveguide type tunnels with Dirichlet and Neumann boundary conditions. The waveguides operate at a frequency of $3GHz$ and have a unit strength gaussian initial field placed at the center with a standard deviation of 3.5λ. The square waveguides have $40\lambda \times 40\lambda(4 \times 4m)$ cross sections and the radius of the circular waveguides are $20\lambda(2m)$. The distance of propagation for each example is $1000\lambda(100m)$. Due to the Nyquist sampling theorem, and the limitation of the PE, our resolution must be bounded by $\Delta x = \Delta y = 2\lambda$ [4]. The figures show pseudocolor plots of the magnitudes of the analytical and numerical scalar potentials for waveguides with Dirichlet and Neumann boundary conditions. The spacings along the transverse plane are $\Delta x = \Delta y = 0.4\lambda$ and the propagation step size is $\Delta z = 10\lambda$. Table 1 displays the rms error, defined

$$E_{rms} = \frac{\sqrt{\frac{1}{N} \sum_m \sum_l |u_{m,l}^{FDM} - u_{m,l}^{anal}|^2}}{\sqrt{\frac{1}{N} \sum_m \sum_l |u_{m,l}^{anal}|^2}}, \tag{4}$$

where $u_{m,l}^{FDM}$ is the approximated discretized field, $u_{m,l}^{anal}$ is the known analytical field and N is the total number of unknowns. Figures 1 and 2 show good agreement between the analytical and numerical fields for the rectangular and circular tunnels with both Dirichlet and Neumann boundary conditions. For the rectangular tunnel, the Neumann boundary conditions were approximated using 2nd order accurate one-sided approximations and for the circular tunnel, the Neumann boundary conditions were approximated by first order interior interpolation. In Figure 3, the Neumann boundary condition were approximated with first order one sided approximations. As with the previous two cases, the field patterns are closely matched, however for the Neumann case the rms error is larger.

Acknowledgments

Conclusions

The ADI technique for the electromagnetic propagation in PEC waveguides for Dirichlet and Neumann boundary conditions is studied and it is found that the field

patterns of the numerical solutions are closely matched with that of the analytical solutions. Future work will involve the more irregular shapes and mixed boundary conditions.

References

[1] Alexei V. Popov and Ning Yan Zhu, *Modeling Radio Wave Propagation in Tunnels with a Vectorial Parabolic Equation*, IEEE, pp. 1403-1412, September 2000.

[2] John C. Strikwerda, *Finite Difference Schemes and Partial Differential Equations* 2nd *Ed*, Philadelphia, PA:Siam, 2004.

[3] Mireille Levy, *Parabolic Equation Method for Electromagnetic Wave Propagation*, London: Institution of Electrical Engineers, 2000.

[4] Chris A. Zelly, *A Three-Dimensional Parabolic Equation Applied to VHF/UHF Propagation over Irregular Terrain*, IEEE Trans. Antennas Propagat., **47**, pp.1586-1596, October 1999.

Table 1: The normalized rms error.

E_{rms} (%)		Rectangular WG		Circular WG		Semi-circular WG	
$\Delta x, \Delta y$	Δz	Dirichlet	Neumann	Dir.	Neu.	Dir.	Neu.
0.8λ	$5\ \lambda$	11.9	10.3	11.4	25.2	12.1	56.4
0.8λ	$10\ \lambda$	13.7	12.2	13.2	24.2	14.0	55.1
0.8λ	$20\ \lambda$	19.5	18.0	18.7	21.9	19.7	51.0
0.4λ	$5\ \lambda$	4.9	4.7	5.0	12.9	5.2	29.1
0.4λ	$10\ \lambda$	7.3	7.1	7.0	11.9	7.6	27.5
0.4λ	$20\ \lambda$	14.4	14.2	13.8	12.0	14.6	24.3
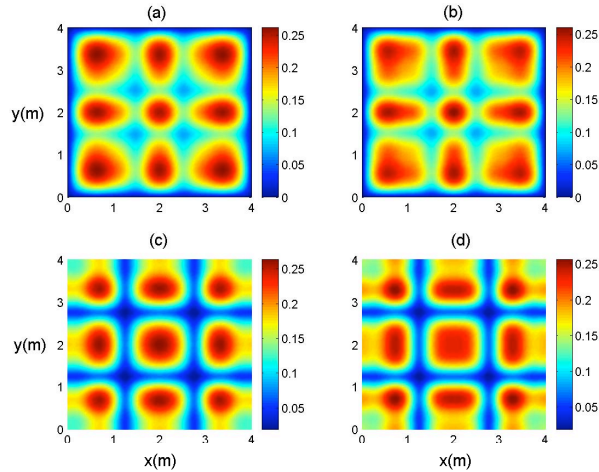
Figure 1: The (a) Analytical solution and (b) Numerical approximation of the rectangular waveguide with Dirichlet boundary conditions (RMS error = 7.3%) and the (c) Analytical solution and (d) Numerical approximation of the rectangular waveguide with Neumann boundary conditions (RMS error = 7.1%) .
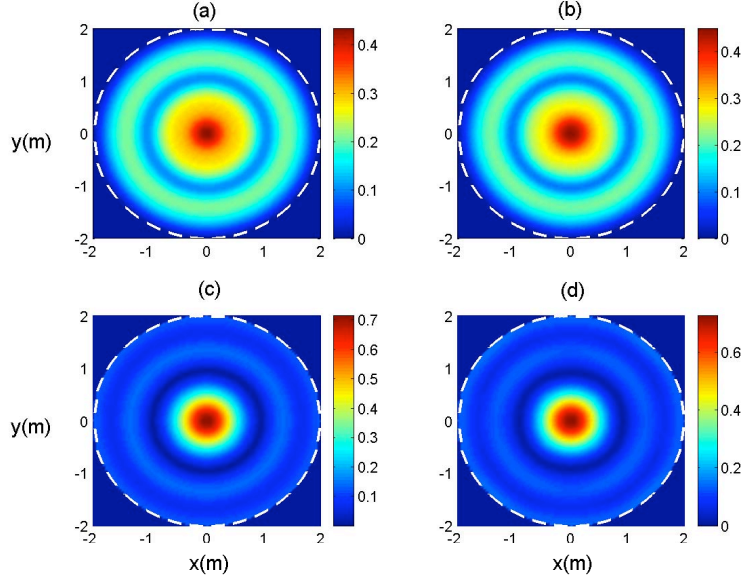
Figure 2: The (a) Analytical solution and (b) Numerical approximation of the circular waveguide with Dirichlet boundary conditions (RMS error = 7.0%) and the (c) Analytical solution and (d) Numerical approximation of the circular waveguide with Neumann boundary conditions (RMS error = 11.9%).
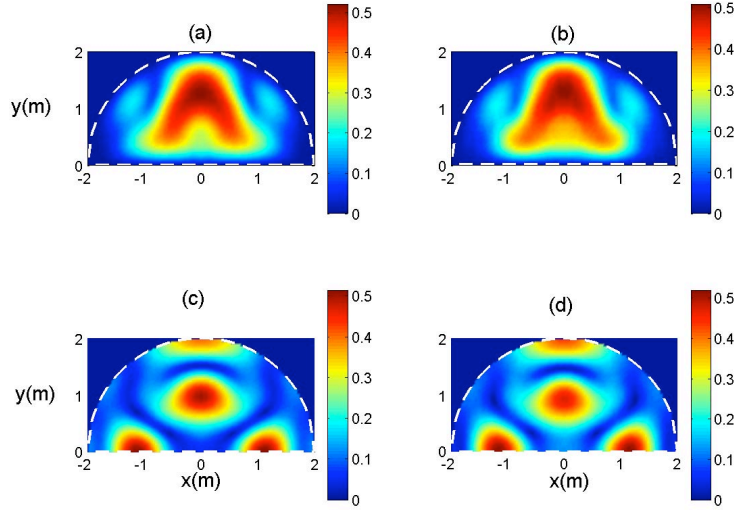

Figure 3: The (a) Analytical solution and (b) Numerical approximation of the semi-circular waveguide with Dirichlet boundary conditions (RMS error = 7.6%) and the (c) Analytical solution and (d) Numerical approximation of the semi-circular waveguide with Neumann boundary conditions (RMS error = 27.5%).

Propagation Prediction in Rough and Branched Tunnels by the ADI-PE Technique

R. Martelly[*]   R. Janaswamy[†]

Abstract — **The study of radiowave propagation in tunnels is important for the development of telecommunication systems. The vector Parabolic Equation (PE) and the alternate direction implicit (ADI) technique are used to study radiowave propagation in branched tunnels and in tunnels with rough walls. Previous work has shown that the ADI-PE method can accurately predict transmission loss in straight tunnels with smooth walls and with known electrical parameters. We extend the analysis of this method by including the realistic cases of branching tunnels and tunnels with rough walls. We breifly discuss the boundary conditions used in each case as well as compare our results with known numerical or analytical models. The numerical results obtained for the branched tunnel case were compared with the results produced by HFSS and the results for the rough wall case were compared with known analytical loss factors. The results show excellent agreement in both cases.**

1 INTRODUCTION

The alternate direction implicit (ADI) method coupled with the vector parabolic equation (PE) has previously been shown to model radiowave propagation in straight tunnels with smooth walls [1, 2]. The PE model assumes the propagating fields are slowly varying in the direction of propagation and backscattered fields are ignored. In realistic tunnels, over a long distance, higher order propagating modes attenuate and the lowest order, slowly varying modes, dominate [3]. The vector PE can accurately solve for the lower order dominate modes which travel within $\pm 15^o$ to the axis of propagation.

The vector PE, as formulated by Popov [2], characterizes the electrical parameters of the tunnel walls with an equivalent surface impedance and enforces the impedance boundary condition [2]. The Crank-Nicolson method has been traditionally used to numerically solve the vector PE because it is an unconditionally stable FDM; but it can also be computationally intensive [1]. The ADI technique is also an unconditionally stable implicit FDM that is significantly more computationally efficient

[*]Department of Electrical and Computer Engineering, University of Massachusetts, Amherst, MA, 01003, US, e-mail: `rmartell@ecs.umass.edu`.
[†]Department of Electrical and Computer Engineering, University of Massachusetts, Amherst, MA, 01003, US, e-mail: `janaswamy@ecs.umass.edu`, tel.: 413-545-0937.

than the Crank-Nicolson method [1]. ADI introduces slightly more error than the Crank-Nicolson method but previous work has shown that, for modest discretizations, the ADI and Crank-Nicolson solutions are nearly identical [1]. After a brief discussion on the ADI-PE formulization (section 2), we continue our analysis of radiowave propagation in tunnels using the ADI-PE by considering the special cases of branched tunnels (section 3) and tunnels with rough walls (section 4).

2 ADI-PE Theory

The vector PE, as formulated by Popov [2], defines the transverse electric fields in terms of a vector function, $\bar{W}$, as shown in equation (1) [2]

$$(E_x, E_y)^T = \bar{W} e^{-jk_o z}, \qquad (1)$$

where k_o is the free space wave number and z is the direction of propagation. The vector function, $\bar{W}$, describes the complex wave amplitude of the plane wave. The vector PE can then be defined as

$$2k_o j \frac{\partial \bar{W}}{\partial z} = \frac{\partial^2 \bar{W}}{\partial x^2} + \frac{\partial^2 \bar{W}}{\partial y^2}. \qquad (2)$$

When the impedance boundary condition is enforced on the tunnel wall, the transverse E fields are coupled and the value of $\bar{W}$ at the boundary is shown to be

$$\bar{W} = \frac{j}{k_o} \begin{pmatrix} n_x & n_y \\ n_y & -n_x \end{pmatrix} \begin{pmatrix} 1/Z_s & 0 \\ 0 & Z_s \end{pmatrix} \begin{pmatrix} n_x & n_y \\ n_y & -n_x \end{pmatrix} \frac{\partial \bar{W}}{\partial n}. \quad (3)$$

where n_x and n_y are the x and y components of the normal vector on the boundary and Z_s is the normalized surface impedance.

As shown in [1], the ADI-PE can be summarized by

$$\left(1 - \frac{r_x}{4jk_o}\delta_x\right)\bar{W}^{n+1/2} = \left(1 + \frac{r_y}{4jk_o}\delta_y\right)\bar{W}^n$$

$$\left(1 - \frac{r_y}{4jk_o}\delta_y\right)\bar{W}^{n+1} = \left(1 + \frac{r_x}{4jk_o}\delta_x\right)\bar{W}^{n+1/2}, (4)$$

where $r_{x(y)}$ is the mesh ratio and the difference quotient, $\delta_{x(y)}$, represent the second order discretization of the x and y derivatives.

3 Branched Tunnels

3.1 Branched Tunnel Model

A typical branch tunnel geometry is shown in Figure 1, where the main tunnel axis is shown as a solid bold line and the branch tunnel axis is shown as the long dashed line. The branch angle, θ_b, is the angle between the axis of the straight and branch tunnel. Using this geometry, the branch angle must be less than 30° to ensure that reflected rays entering the branch are within our PE limit of $\pm 15^o$. Considering also the rays diffracted from the corners at the junction, we can arrive at a much more stringent requirement of $\theta_b < 15$. Figures 1 and 2 show the incident and reflected ray as it enters the branch tunnel. The short dashed line markes the input plane of the branch tunnel. The grazing angle, Ψ, and the angle of the ray entering the branch, α, are also shown.
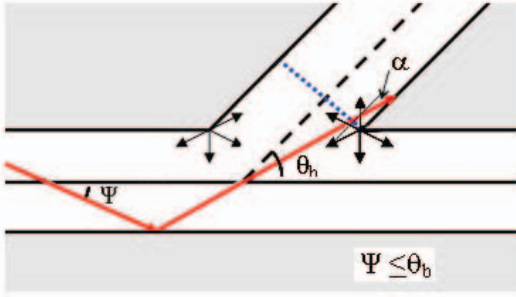
Figure 1: The incident and reflected ray entering the branch tunnel when $\Psi \leq \theta_b$.
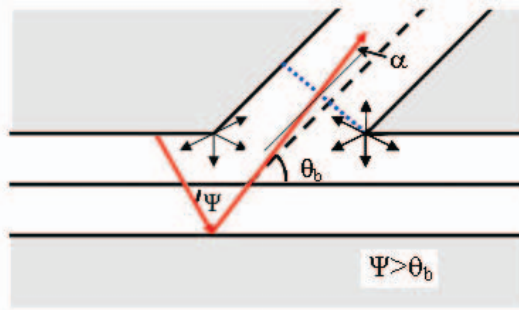
Figure 2: The incident and reflected ray entering the branch tunnel when $\Psi < \theta_b$.

The slope of the branching wall is modeled using a staircase approximation (see Figure 3a) and the impedance boundary condition is enforced on all four walls as outlined in [1] and [2]. The fields along the planes marking the entrance of the main tunnel (line C) and the branch tunnel (line B) are solved simultaneously and then used as the initial fields for the two separate diverging tunnels. We simulate a $0.9\,\mathrm{m} \times 1.0\,\mathrm{m}$ rectangular tunnel with a branch angle of 15° and operating at a frequency of 900 MHz. We used the far zone field of a unit strength Gaussian field source as our initial field. The source, with standard deviation of $0.75\,\lambda$(wavelength), is placed at the center of the tunnel entrance. This means we are only using the lowest order modes as our initial field [1, 3]. The fundamental mode propagates near our PE limit at 14.17^o.

3.2 Comparison of numerical results to HFSS

For our ADI simulation, we used discretizations (within the tunnel junction) of $\Delta x = 0.060\,\lambda$, $\Delta y = 0.054\,\lambda$ and $\Delta z = 0.013\,\lambda$. The cross-sectional coordinates are indicated by x and y, while the axial coordinate in the main tunnel is denoted by the z-axis. To validate our results, we compared our solutions with HFSS [6] and plot the magnitude of the E_y field along the main and branch tunnel axis. In the HFSS simulation, we used radiation boundary conditions to terminate the tunnel and symmetry planes to reduce computational labor.

HFSS is a full wave simulator and, unlike the ADI-PE, solves for backscattered waves as well as waves traveling in the forward direction. The backscattering is seen as fluctuations in the axial field in Figure 3b near the diverging tunnels. The tunnel has a dielectric constant of 5 and conductivity of $0.1\,\mathrm{S/m}$. A high conductivity was chosen so there will be appreciable loss in the small tunnel dimensions allowed in HFSS. As we can see from Figure 3b, there is strong agreement in the axial field intensity along the main and branch tunnel axis between the ADI and HFSS. The figure also shows that there is about a $10\,\mathrm{dB}$ drop when going from the main to the branch tunnel (at the point marked C in Figure 3b).

Although the ADI-PE was used to simulate a tunnel with a relatively small electrical cross-section ($2.7\lambda \times 3\lambda$), the ADI-PE is capable of handling larger tunnels at higher frequencies without running into memory problems on an average (2 GB RAM) PC [1].

4 Tunnels with Rough walls

4.1 Surface roughness model

Surface roughness is the local variation of the tunnel wall relative to a mean surface level [4, 5]. In this study we consider random surface deviations in an otherwise smooth wall. For the purpose of
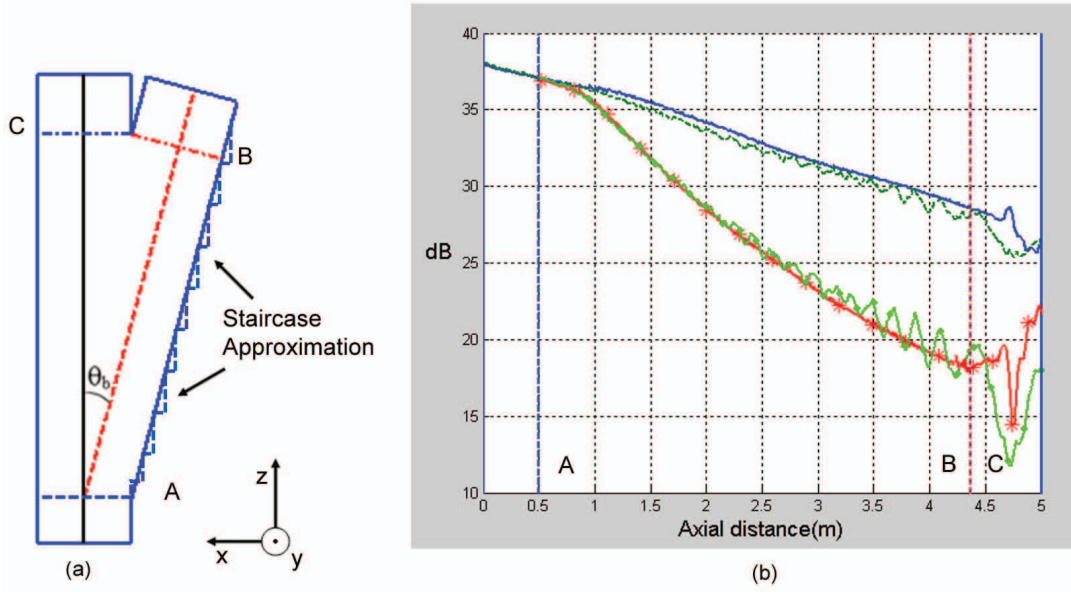
Figure 3: (a) Geometry of the branch tunnel. (b) The axial field intensity of the main tunnel from ADI (blue, solid), HFSS (dark green, dashed), the branch tunnel from ADI (red,*) and HFSS (light green, dot).

numerical computations we assume the random deviations to be Gauassian distributed. A Gaussian distribution of the surface level can be characterized by a root-mean-square height deviation σ_h and correlation length, l [4, 5]. Smooth tunnels have a typical RMS height deviation of $0.01\,\mathrm{m}$ and rough surfaces, such as those found in coal mine tunnels, have a RMS height deviation of $0.1\,\mathrm{m}$ [4]. The loss of the E_x field in a rectangular tunnel is given by equation (5) [4]

$$L_{rough} = 4.343\pi^2 h^2 \lambda^2 \left(\frac{1}{d_1^4} + \frac{1}{d_2^4} \right) z \quad (\mathrm{dB}) \quad (5)$$

where d_1 and d_2 are the tunnel dimensions in the x and y axis, respectively.

Small scale roughness can be characterized by replacing the rough surface with a flat impedance surface that produces an equivalent specular reflection coefficient. The equivalent impedance for horizontal polarization is given by [5]

$$Z_{eq} = \begin{cases} Z_s - j(k_o\sigma_h)^2 \frac{\sqrt{\pi}}{2k_o l}, & k_o l \ll 1 \\ Z_s + (k_o\sigma_h)^2 \sin\Psi, & k_o l \gg 1, \Psi \gg \frac{1}{\sqrt{k_o l}} \\ Z_s + (k_o\sigma_h)^2 \Gamma\left(\frac{3}{4}\right)\sqrt{\frac{-2j}{\pi k_o l}}, & k_o l \gg 1, \Psi \ll \frac{1}{\sqrt{k_o l}} \end{cases}$$
$$(6)$$

where Z_s is the surface impedance for the smooth wall, $\Gamma(\cdot)$ is the Gamma function, and Ψ is the grazing angle. Due to the PE angle limitation of $\pm 15^o$, the maximum slope angle θ of the rough surface

and the grazing angle must satisfy the following relationship

$$2\theta + \Psi \le 15^o \quad (7)$$

where Ψ is defined as shown in Figure 4. As we can see from Figure 4, the angle of the specular reflection of the incident ray, denoted by ξ, will depend on the height deviation of the roughness. The roughness angle, θ, is related to σ_h and l by $\tan\theta = \sigma_h/l$.
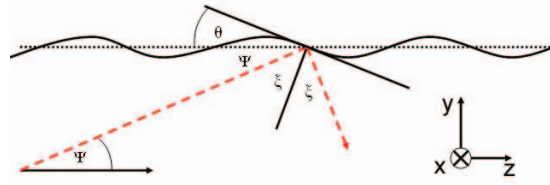

Figure 4: The geometry of the rough surface.

4.2 Comparison of numerical and analytical solutions

We consider a rectangular $4.26\,\mathrm{m} \times 2.10\,\mathrm{m}$ tunnel and a circular tunnel with radius of $2\,\mathrm{m}$. The fundamental EH_{11}^x mode is used as the initial field of the rectangular tunnel and the fundamental TE_{01} mode generated by a loop ring excitation is used as the initial field for the circular tunnel. Both tunnels

operate at a frequency of 1 GHz and the dielectric constant and conductivity of the tunnel wall are taken as ϵ_r=12 and $\sigma_o = 0.02$ S/m, respectively.

Tables 1 and 2 summarize the mode attenuation factors (MAFs), or the loss in dB/km, of the smooth and rough tunnels with rectangular and circular cross-sections, respectively. In real tunnels, as in our simulations, the lowest order mode will determine the MAF over a long distance. We used equation (5) as our analytical loss factor for both the rectangular and circular tunnel. As we can see from equation (5), the loss due to roughness is a function of wavelength. To notice an appreciable loss at 1 GHz, we need to assume the walls are as rough as cave walls. Therefore, we used a RMS height of 0.1 m $(0.33\,\lambda)$ and a correlation length of 2.5 m $(8.33\,\lambda)$ for both tunnels.

The grazing angle of the fundamental mode of the rectanglular and circular tunnel is 4.56^o and 5.25^o, respectively. The roughness angle is 2.29^o and equation (7) is satisfied. The ADI is simulated using discretizations of $\Delta x = 0.284\,\lambda$, $\Delta y = 0.14\,\lambda$ and $\Delta z = 4\ \lambda$ for the rectangular tunnel and $\Delta x = \Delta y = 0.44\,\lambda$ and $\Delta z = 1.67\,\lambda$ for the circular tunnel. As we can see from Table 1, the excess loss due to roughness for the rectangular tunnel is about 7 dB when using either equation (5) or the ADI-PE. Similarly, Table 2 shows the same close agreement in numerical and theoretical excess loss for the tunnel with circular cross-section. In this case, the excess loss due to roughness is about 16 dB.

	Rectangular Tunnel (dB/km) 4.26 m×2.10 m	
	Analytical	ADI-PE
w/o Roughness	31.0	29.5
Roughness	38.0	36.6

Table 1: Analytical and Numerical MAFs.

	Circular Tunnel (dB/km) Radius = 2.0 m	
	Analytical	ADI-PE
w/o Roughness	11.0	10.1
Roughness	27.0	26.1

Table 2: Analytical and Numerical MAFs.

The accuracy of the results suggests that the equivalent surface impedance, along with ADI-PE, is an adequate model for determining loss due to surface roughness. Unlike the ADI-PE, a finite element method would be limited to low frequencies and electrically small tunnel cross-sections and the equivalent Crank-Nicolson code would require significantly larger matrices [1].

5   Conclusions

The ADI-PE method has been shown to accurately model branch tunnels and tunnels with rough walls. For branch tunnels, even at the PE limit, there is good agreement between the ADI-PE and with commerical simulation codes such as HFSS. Also, the additional loss created by tunnels with rough walls is correctly modeled using equivalent impedances. The ADI-PE method compares well with known theoretical roughness loss factors.

References

[1] R. Martelly and R. Janaswamy,"An ADI-PE Approach for Modeling Radio Transmission Loss in Tunnels", IEEE Transactions on Antennas and Propagation, **57**, 6, June 2009.

[2] A.V. Popov and N.Y. Zhu, "Modeling Radio Wave Propagation in Tunnels with a Vectorial Parabolic Equation", IEEE Transactions on Antennas and Propagation, **48**, 9, pp. 1403-1412, September 2000.

[3] D.G. Dudley, M. Lienard, S.F. Mahmoud, and P. Degauque, "Wireless Propagation in Tunnels", IEEE Antennas and Propagation Magazine, **49**, 2, pp. 11-26, April 2007.

[4] A.G. Emslie, R.L. Lagace and P.F. Strong, "Theory of the Propagation of UHF Radio Waves in Coal Mine Tunnels", IEEE Transactions on Antennas and Propagation, **AP-23**, No. 2, pp. 192-205, March 1975.

[5] R. Janaswamy, "Radiowave Propagation and Smart Antennas for Wireless Communications", New York: Sringer, 2000.

[6] Ansoft Corporation, "User's Guide: High Frequency Structure Simulator V. 9.2", Ansoft Documentation, 2003.

Transitional probabilities for the 4-state random walk on a lattice

R Janaswamy

Department of Electrical and Computer Engineering, University of Massachusetts,
215-D Marcus Hall, 100 Natural Resources Road, Amherst, MA 01003, USA

E-mail: janaswamy@ecs.umass.edu

Abstract
The diffusion and Schrödinger propagators have been known to coexist on a
lattice when a particle undergoing random walk is endowed with two states of
spin in addition to the two states of direction in a 1+1 spacetime dimension.
In this paper we derive explicit expressions for the various transitional
probabilities by employing generating functions and transform methods. The
transitional probabilities are all expressed in terms of a one-dimensional integral
involving trigonometric functions and/or Chebyshev polynomials of the first
and second kind from which the spacetime continuum limits of the diffusion
equation and Schrödinger equation follow directly.

PACS numbers: 03.65.−w, 05.40.Fb

1. Introduction

There has been a lot of interest in the recent past to understand quantum mechanics in the
context of classical statistical mechanics. On the one hand, Brownian motion provides a
microscopic model of diffusion and provides an unambiguous interpretation of the diffusion
equation. On the other hand, a similar physical interpretation is lacking for the Schrödinger
equation, whose wave solution is a complex quantity without a physical reality. Because
classical diffusion cannot account for the self-interference pattern that is so intrinsic to quantum
behavior, several theories have been put forward recently to understand the microphysics of
quantum behavior. Nelson [1] derived the Schrödinger equation starting from Newtonian
mechanics and by assuming that a particle is subject to an underlying Brownian motion
described by a combined forward-in-time and a backward-in-time Wiener processes. A
detailed account of Nelson's original idea of stochastic mechanics and its subsequent
refinement is given in [2–5]. Nottale [6] and Ord [7] advanced the idea that spacetime is
not differentiable but is of a fractal nature, suggesting that an infinity of geodesics lie between
any two points and, thereby, providing a fundamental and universal origin for the double

Wiener process of Nelson. These ideas are elaborated in the monograph [8]. El Naschie [9] too considered a fractal spacetime with a Cantorial structure and argued that quantum behavior could be mimicked by combining this fractal spacetime with a diffusion process. A totally different paradigm was recently introduced by Ord [10], who by considering a symmetric random walk on a lattice, showed that both the diffusion equation and the Schrödinger equation occur as approximate descriptions of different aspects of the same classical probabilistic system. By considering a 4-state random walk (4RW) on a discrete lattice, wherein a particle is endowed with two states of direction and two states of spin, Ord [10–12] has shown that both diffusion and Schrödinger propagators coexist on a lattice and that either can be obtained from a distinct projection of the same random walk. It is too early to speculate as to which of Nelson's or Ord's model will duplicate the true quantum behavior under a variety of situations. This can only be ascertained through additional work on both models. It may be mentioned that the combination of displacement and spin have also been used previously in [13, 14] to study dynamics of a quantum particle in spacetime. However, the important distinction between the Ord model and the one considered in [13, 14] is that the states describing the direction of motion are independent of those describing the spin states in the former model. There is also an intrinsic notion of *memory* embedded in the Ord's model.

The Schrödinger type of equation is encountered under the guise of *parabolic wave equation*, or simply parabolic equation in the solution of boundary-value problems in several branches of applied physics such as acoustics [15], optics and classical electromagnetic wave propagation [16]. In such boundary-value problems, inhomogeneities of the propagating medium caused by the varying index of refraction of the intervening material take the place of the potential field experienced by a quantum particle. The standard parabolic equation is resulted when one extracts paraxial propagation along a preferred direction from the full Helmholtz equation. In addition to providing a microscopic model for the Schrödinger equation, the 4RW model considered by Ord is also attractive in the solution of stochastic differential equations associated with these parabolic type of equations, carried out by employing only real random processes. Because walks modeling the Schrödinger equation in the 4RW model traverse only real space, no analytical continuation of boundary data into complex space is required that would otherwise be demanded [17, 18] when solving these boundary-value problems.

Ord does not provide explicit expressions for the various transitional probabilities, but, instead, discusses the continuum limits directly from the governing difference equations. For a variety of reasons, it is desirable to obtain closed-form expressions (or those involving integrals) for these transitional probabilities. In this paper, we provide analytical expressions for the transitional probabilities associated with the 4-state random walk in 1+1 dimension in spacetime by using a transform approach. Our work here is partly motivated by the desire to have expressions for the transitional probabilities while solving the aforementioned boundary-value problems using the parabolic equation in a homogeneous medium. Using these expressions, it is further shown that in the continuum limits as the mesh size shrinks to zero in both space and time, one directly recovers the diffusion equation and the Schrödinger equation. Thus, the main contributions of the paper are to (i) elucidate methodology for obtaining the closed-form expressions for the various transitional probabilities of the 4RW, and (ii) establish the continuum limits of the diffusion and Schrödinger equations describing the dynamics of particles obeying the 4RW. The methodology presented in this paper is most suitable for describing quantum dynamics of a free-particle, although the 4RW model itself has been extended in the presence of a potential field [19]. The paper is organized as follows: section 2 gives a brief introduction of the random walks considered in [10, 12]. Section 3 introduces the generating functions and the 2D transforms considered in this paper.

Table 1. Various states in random walk.

State	Direction	Spin
1	Right	+1
2	Left	+1
3	Right	−1
4	Left	−1

Section 4 provides expressions for the various transitional probabilities as well as discusses the derivation of the diffusion equation and the Schrödinger equation as continuum limits of these probabilities.

2. Multistate random walks

Consider the 4RW model proposed by Ord and Deakin [12], where a particle undergoes random motion in discrete spacetime ($x = m\Delta, t = s\epsilon$), with x denoting space and t denoting time, and Δ and ϵ denoting the spatial and temporal steps, respectively. At every point the particle is endowed with two independent binary properties, its direction of motion (right or left) and its spin or parity (± 1). The particle is assumed to change its direction with every collision, but change its spin only every other collision. The four states of the particle corresponding to the four combinations of direction and spin are indicated in table 1. Note that the particle can execute any direction of motion irrespective of the spin, in contrast to the model used in [13, 14]. However, there is an intrinsic assumption of *memory* in Ord's model that arises from keeping track of the parity of collisions. If $p_\mu(m\Delta, s\epsilon)\Delta, \mu = 1, \ldots, 4$, is the probability that a particle is in state μ at the spacetime point $(m\Delta, s\epsilon), m = 0, \pm 1, \pm 2, \ldots, s = 0, 1, \ldots$, then the transitional relations considered in [12] were of the form

$$p_1[m\Delta, (s+1)\epsilon)] = \alpha p_1[(m-1)\Delta, s\epsilon] + \beta p_4[(m+1)\Delta, s\epsilon]$$

$$p_2[m\Delta, (s+1)\epsilon)] = \alpha p_2[(m+1)\Delta, s\epsilon] + \beta p_1[(m-1)\Delta, s\epsilon]$$

$$p_3[m\Delta, (s+1)\epsilon)] = \alpha p_3[(m-1)\Delta, s\epsilon] + \beta p_2[(m+1)\Delta, s\epsilon] \tag{1}$$

$$p_4[m\Delta, (s+1)\epsilon)] = \alpha p_4[(m+1)\Delta, s\epsilon] + \beta p_3[(m-1)\Delta, s\epsilon],$$

where $\alpha + \beta = 1$. Here, α is the probability that a particle maintains its direction at the next time step, whereas β is the probability that it will change its direction at the next time step. The Markov-chain character of the transitional probabilities is evident from definitions in (1). From the total probability theorem, the probability that a particle is somewhere on the lattice at a given time is equal to 1 and is represented mathematically by

$$\sum_{\mu=1}^{4} \sum_{m=-\infty}^{\infty} p_\mu(m\Delta, s\epsilon)\Delta = 1. \tag{2}$$

Ord [10] has shown that the diffusion and Schrödinger propagators coexist on the lattice and that both behaviors are embedded in equations (1). To affect a separation of the diffusive behavior from the wave-like behavior, the following linear transformation is used: $q_1(m\Delta, s\epsilon) = 2^{s/2}[p_1(m\Delta, s\epsilon) - p_3(m\Delta, s\epsilon)], q_2(m\Delta, s\epsilon) = 2^{s/2}[p_2(m\Delta, s\epsilon) - p_4(m\Delta, s\epsilon)], w_1(m\Delta, s\epsilon) = [p_1(m\Delta, s\epsilon) + p_2(m\Delta, s\epsilon) + p_3(m\Delta, s\epsilon) + p_4(m\Delta, s\epsilon)]$, and $w_2(m\Delta, s\epsilon) = [p_1(m\Delta, s\epsilon) + p_3(m\Delta, s\epsilon)] - [p_2(m\Delta, s\epsilon) + p_4(m\Delta, s\epsilon)]$. The quantity $q_1\Delta$ (without the weight factor $2^{s/2}$) indicates the expected difference in the number of

particles of opposite spin arriving at $(m\Delta, s\epsilon)$ while moving to the right. Similarly, $q_2\Delta$ refers to the expected number of particles arriving at $(m\Delta, s\epsilon)$ while moving to the left. Also, $w_1(m\Delta, s\epsilon)\Delta$ is the probability that a particle leaves $(m\Delta, s\epsilon)$ in either direction and in any spin state, and $w_2(m\Delta, s\epsilon)\Delta$ is the difference in the probabilities that a particle leaves $(m\Delta, s\epsilon)$ to the right and the left. Introducing the shift operator $E_x^{\pm 1} p_\mu(m\Delta, s\epsilon) = p_\mu[(m \pm 1)\Delta, s\epsilon]$, a time-advancing operator $E_t p_\mu(m\Delta, s\epsilon) = p_\mu[m\Delta, (s + 1)\epsilon]$, and the vector $\mathbf{p} = [p_1, p_2, p_3, p_4]^T$, where the superscript T denotes transpose, the transitional relations in (1), which are of the form $E_t\mathbf{p} = \mathbf{S}_x\mathbf{p}$, get transformed into

$$E_t \begin{pmatrix} w_1 \\ w_2 \end{pmatrix} = \frac{1}{2} \begin{pmatrix} (E_x + E_x^{-1}) & -(E_x - E_x^{-1}) \\ (\alpha - \beta)(E_x - E_x^{-1}) & (\alpha - \beta)(E_x + E_x^{-1}) \end{pmatrix} \begin{pmatrix} w_1 \\ w_2 \end{pmatrix}, \qquad (3)$$

$$E_t \begin{pmatrix} q_1 \\ q_2 \end{pmatrix} = \frac{1}{\sqrt{2}} \begin{pmatrix} 2\alpha E_x^{-1} & -2\beta E_x \\ 2\beta E_x^{-1} & 2\alpha E_x \end{pmatrix} \begin{pmatrix} q_1 \\ q_2 \end{pmatrix}. \qquad (4)$$

Thus the variables (w_1, w_2) get decoupled from (q_1, q_2). Essentially, this decoupling results from block-diagonalizing the matrix $\mathbf{S}_x$ and describing the system in terms of its eigenstates. The physical significance of this transformation is touched upon in [11, 12]. Note that w_j and q_j need not strictly be probabilistic quantities (meaning $\geqslant 0$), but we will continue to describe them as 'transitional probabilities' with the understanding that the actual probabilistic quantities, namely, p_μ, can be easily recovered from these using the inverse relations.

3. Generating functions and transforms

We are interested in the solutions of (3) and (4) for the special case of a symmetric random walk with $\alpha = \beta = 0.5$. In this case we have a set of linear difference equations and the solution can be obtained conveniently using transform methods [20, 21] and appropriate generating functions. The key step here is to pick a suitable transform consistent with the nature and domain of definition of the problem. We denote the 2D transform $\mathcal{L}$, consisting of a Fourier transform in space (owing to the unbounded nature of the spatial coordinate) and the z-transform [22] in time (the z-transform can be arrived from the discretized version of a Laplace transform and is suitable for discrete functions defined on a half-line), of a discrete function $v(m\Delta, s\epsilon)$ as $V(k_x, z)$ and define

$$V(k_x, z) = \Delta \sum_{m=-\infty}^{\infty} \sum_{s=0}^{\infty} v(m\Delta, s\epsilon) z^s \, \mathrm{e}^{-imk_x\Delta} \equiv \mathcal{L}v(m\Delta, s\epsilon). \qquad (5)$$

The inverse relation can then be obtained as

$$v(m\Delta, s\epsilon) = \frac{1}{4\pi^2 \mathrm{i}} \int_{k_x=-\pi/\Delta}^{\pi/\Delta} \oint_{C_z} \frac{V(k_x, z)}{z^{s+1}} \, \mathrm{e}^{imk_x\Delta} \, \mathrm{d}k_x \, \mathrm{d}z \equiv \mathcal{L}^{-1} V(k_x, z), \quad (6)$$

where the identities

$$\int_{k_x\Delta=-\pi}^{\pi} \mathrm{e}^{\mathrm{i}(n-m)k_x\Delta} \, \mathrm{d}k_x\Delta = 2\pi \delta_m^n \qquad (7)$$

$$\oint_{C_z} z^{r-s-1} \, \mathrm{d}z = 2\pi \mathrm{i}\delta_s^r \qquad (8)$$

are used to derive (6). Here δ_m^n is the Kronecker's delta and C_z is a closed contour around the origin in the complex z-plane that encloses only the singularities at the origin. The present

analysis, consisting of the z-transform along the time axis and Fourier transform along the spatial axis, is most suitable for studying linear difference equations with constant coefficients such as encountered in the study of free-Schrödinger equation by the 4RW model. Other suitable methods must be devised for studying particle motion in the presence of a potential field. Note that $V(k_x, z)$ is periodic in k_x with a period $2\pi/\Delta$. Using the definition in (5), it can also be shown that

$$\mathcal{L}v[m\Delta, (s+1)\epsilon] = z^{-1}[V(k_x, z) - V_0(k_x)] \tag{9}$$

$$\mathcal{L}v[(m \pm 1)\Delta, s\epsilon] = \mathrm{e}^{\pm ik_x\Delta}V(k_x, z), \tag{10}$$

where $V_0(k_x)$ is the Fourier transform of the initial distribution $v(m\Delta, 0)$:

$$V_0(k_x) = \Delta \sum_{m=-\infty}^{\infty} v(m\Delta, 0)\,\mathrm{e}^{-imk_x\Delta}. \tag{11}$$

Note that the periodicity property of $V_0(k_x)$ implies that $V_0(\pi/\Delta) = V_0(-\pi/\Delta)$.

4. Transitional probabilities

Having defined the required transforms, we will now derive expressions for the transitional probabilities w_1, w_2, q_1 and q_2. Because of the decoupling afforded in (3) and (4), it is sufficient to consider the diffusive and wave-like behaviors separately.

4.1. Diffusive behaviour

The diffusive part of the particle motion is governed by the discrete functions w_1 and w_2 as will be evident shortly. Let $W_1(k_x, z)$ and $W_2(k_x, z)$ be the 2D transforms of $w_1(m\Delta, s\epsilon)$ and $w_2(m\Delta, s\epsilon)$ and $\Upsilon_1(k_x)$ and $\Upsilon_2(k_x)$ be the transforms of the initial distributions $w_1(m\Delta, 0)$ and $w_2(m\Delta, 0)$, respectively. From the definition of w_1 in terms of $p_\mu, \mu = 1, \ldots, 4$, and relation (2), it is seen that $\Upsilon_1(0) = 1$. On applying the transform $\mathcal{L}$ to the set (3) and making use of the properties (9) and (10), it is easy to see that $W_2(k_x, z) = \Upsilon_2(k_x)$ and

$$W_1(k_x, z) = \frac{\Upsilon_1(k_x) - iz\sin(k_x\Delta)\Upsilon_2(k_x)}{1 - z\cos(k_x\Delta)} \tag{12}$$

$$= \sum_{n=0}^{\infty} z^n \cos^n(k_x\Delta)\left[\Upsilon_1(k_x) - iz\sin(k_x\Delta)\Upsilon_2(k_x)\right] \tag{13}$$

where (13) has been obtained by using the series expansion of $[1 - z\cos(k_x\Delta)]^{-1}$. Such a series converges uniformly provided that $|z\cos(k_x\Delta)| < 1$ and this can always be insured by choosing an appropriate C_z in (6). In other words, the contour C_z is chosen such that the zeroes of the function $1 - z\cos(k_x\Delta)$ lie outside it. Substituting this into (6) and making use of (8), we finally arrive at

$$w_1(m\Delta, s\epsilon) = \frac{1}{2\pi}\int_{-\pi/\Delta}^{\pi/\Delta}\cos^s(k_x\Delta)[\Upsilon_1(k_x) - i\Theta(s-1)\tan(k_x\Delta)\Upsilon_2(k_x)]\,\mathrm{e}^{imk_x\Delta}\,\mathrm{d}k_x, \tag{14}$$

where $\Theta(\cdot)$ is the Heaviside step function. For a given $\Upsilon_1(k_x)$ and $\Upsilon_2(k_x)$, integral (14) may be computed efficiently by the application of the inverse fast Fourier transform (iFFT) algorithm [22]. However, for special values of $\Upsilon_1(k_x)$ and $\Upsilon_2(k_x)$, the integral may be evaluated in
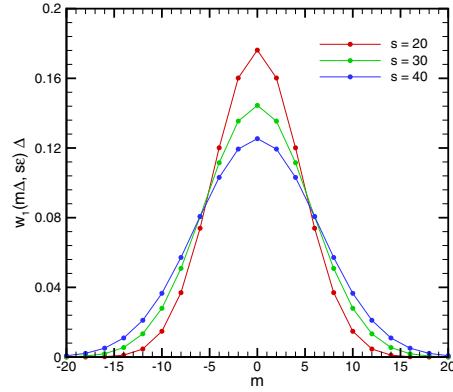
Figure 1. Calculated values of $w_1(m\Delta, s\epsilon)$ for $\Upsilon_1(k_x) = 1$, $\Upsilon_2(k_x) = 0$.

a closed form. For example, with $w_1(m\Delta, 0) = \frac{1}{\Delta}\delta_m^0$, $w_2(m\Delta, 0) = 0 (\Longrightarrow \Upsilon_1(k_x) = 1, \Upsilon_2(k_x) = 0)$ and m and s even, (14) reduces to ([23], 3.631–17)

$$w_1(m\Delta, s\epsilon)\Delta = \frac{1}{2^s}\binom{s}{(s-m)/2}, \qquad m \leqslant s. \tag{15}$$

The right-hand side of (15) gives the probability of finding a particle at m in s steps, given that it started at the origin at $s = 0$, in a symmetric, discrete-time, 1D random walk. The result can be obtained directly from combinatorial analysis and is available in standard texts ([24], p 75), ([25], p 16). Figure 1 shows a plot of $w_1(m\Delta, s\epsilon)\Delta$ for $s = 20$, 30 and 40, where the data at discrete m has been connected by smooth lines for the sake of visual clarity. The plots clearly exhibit the diffusive behavior of w_1, wherein w_1 spreads out in space with a diminishing peak value as s increases. Using the identity $\sum_{m=-\infty}^{\infty} \exp(\pm imx) = 2\pi\delta(x)$, $-\pi \leqslant x \leqslant \pi$, where $\delta(\cdot)$ is the delta function, it may be easily verified from (14) that $\sum_{m=-\infty}^{\infty} w_1(m\Delta, s\epsilon)\Delta = 1$. Also note that $w_1 > 0$. Hence $w_1\Delta$ behaves like a true probability mass function.

We are also interested in the continuum limits $\Delta \to 0$, $\epsilon \to 0$, $m \to \infty$, and $s \to \infty$ such that $\Delta^2/2\epsilon = D > 0$, $m\Delta \to x$, $s\epsilon \to t$. Using the results $\lim_{\substack{\Delta \to 0 \\ s \to \infty}} [\cos^s(k_x\Delta)] = \exp\left(-k_x^2 Dt\right)$, $\lim_{\substack{\Delta \to 0 \\ s \to \infty}} [\cos^s(k_x\Delta)\tan(k_x\Delta)] = 0$ in (14), we arrive at

$$w_1(x, t) = \frac{1}{2\pi}\int_{-\infty}^{\infty} \Upsilon_1(k_x)\, e^{-k_x^2 Dt}\, e^{ik_x x}\, dk_x. \tag{16}$$

This is the well-known solution of the diffusion equation $\partial w_1/\partial t = D\partial^2 w_1/\partial x^2$ in an unbounded medium with an initial spectral content $\Upsilon_1(k_x)$ (see, for example, [26]). For an impulsive initial condition, $\Upsilon_1(k_x) = 1$, and one recovers the Green's function $w_1(x, t) = \exp(-x^2/4Dt)/\sqrt{4\pi Dt}$. The function $w_1(m\Delta, s\epsilon)$ given in equation (14) is the discrete version of $w_1(x, t)$ and is seen to depend not only on $\Upsilon_1(k_x)$, but also on $\Upsilon_2(k_x)$. The latter contribution arises entirely from the discrete nature of space and vanishes in the continuum limit. To summarize, the quantity $w_1(m\Delta, s\epsilon)\Delta$ that describes the probability that a particle leaves $(m\Delta, s\epsilon)$ in either direction and in any spin state describes the diffusion process for a symmetric 4RW.

4.2. Wave-like behaviour

The wave-like behavior of the particle motion is governed by the discrete functions q_1 and q_2. The governing equations in this case are repeated below from (4):

$$E_t \begin{pmatrix} q_1 \\ q_2 \end{pmatrix} = \frac{1}{\sqrt{2}} \begin{pmatrix} E_x^{-1} & -E_x \\ E_x^{-1} & E_x \end{pmatrix} \begin{pmatrix} q_1 \\ q_2 \end{pmatrix}. \tag{17}$$

Our objective here is to derive closed-form expressions for the transitional probabilities q_1 and q_2. Let $Q_j(k_x, z)$ be the $\mathcal{L}$ transforms of $q_j(m\Delta, s\epsilon)$, and let $\Gamma_j(k_x)$ be the Fourier transforms of the initial distribution $q_j(m\Delta, 0)$, $j = 1, 2$. On applying the $\mathcal{L}$ transform to (17) and making use of properties (9) and (10) and carrying out some algebraic manipulations, we get

$$\begin{bmatrix} Q_1(k_x, z) \\ Q_2(k_x, z) \end{bmatrix} = \frac{1}{(1 - \sqrt{2}z\cos(k_x\Delta) + z^2)} \begin{bmatrix} 1 - \frac{z}{\sqrt{2}} e^{ik_x\Delta} & -\frac{z}{\sqrt{2}} e^{ik_x\Delta} \\ \frac{z}{\sqrt{2}} e^{-ik_x\Delta} & 1 - \frac{z}{\sqrt{2}} e^{-ik_x\Delta} \end{bmatrix} \begin{bmatrix} \Gamma_1(k_x) \\ \Gamma_2(k_x) \end{bmatrix}. \tag{18}$$

To permit evaluation of the integral with respect to z in the inverse transform, we need to express Q_1 and Q_2 in a separable form with respect to k_x and z. To this end, we make use of the identity ([23], 8.945.2)

$$\frac{1}{1 - 2tx + t^2} = \sum_0^\infty U_n(x)t^n, \tag{19}$$

where $U_n(\cdot)$ is the Chebyshev polynomial of the second kind of order n, in (18) to arrive at

$$Q_1(k_x, z) = \sum_{n=0}^\infty U_n\left(\frac{\cos k_x\Delta}{\sqrt{2}}\right) z^n \left[\left(1 - \frac{z}{\sqrt{2}} e^{ik_x\Delta}\right)\Gamma_1(k_x) - \frac{z}{\sqrt{2}} e^{ik_x\Delta}\Gamma_2(k_x)\right] \tag{20}$$

$$Q_2(k_x, z) = \sum_{n=0}^\infty U_n\left(\frac{\cos k_x\Delta}{\sqrt{2}}\right) z^n \left[\frac{z}{\sqrt{2}} e^{-ik_x\Delta}\Gamma_1(k_x) + \left(1 - \frac{z}{\sqrt{2}} e^{-ik_x\Delta}\right)\Gamma_2(k_x)\right]. \tag{21}$$

As with the diffusive case, the contour C_z in the inverse transform is chosen such that the zeroes of the denominator function $(1 - \sqrt{2}z\cos(k_x\Delta) + z^2)$ lie outside it. Equations (20) and (21) may be substituted into the definition of the inverse transform (6) and the integral with respect to z evaluated by making use of (8). For reasons that will become clear shortly, we are interested in the composite discrete function $\psi_d(m\Delta, s\epsilon) = q_2(m\Delta, s\epsilon) + iq_1(m\Delta, s\epsilon)$, which will be compared directly with the solution of the Schrödinger equation. The expression for ψ_d is

$$\psi_d(m\Delta, s\epsilon) = \frac{1}{2\pi} \int_{-\pi/\Delta}^{\pi/\Delta} \left\{ U_s\left(\frac{\cos k_x\Delta}{\sqrt{2}}\right)[\Gamma_2 + i\Gamma_1(k_x)] \right.$$

$$+ U_{s-1}\left(\frac{\cos k_x\Delta}{\sqrt{2}}\right)[(e^{-i\pi/4}\Gamma_1(k_x) - e^{i\pi/4}\Gamma_2(k_x))\cos(k_x\Delta)$$

$$\left. + (e^{-i\pi/4}\Gamma_1(k_x) + e^{i\pi/4}\Gamma_2(k_x))\sin(k_x\Delta)] \right\} e^{imk_x\Delta}\, dk_x. \tag{22}$$

As in section 4.1, the integral in (22) may be evaluated efficiently by employing the iFFT algorithm. In the special case of $\Gamma_1(k_x) = 0, \Gamma_2(k_x) = K_2$, a constant, the expression provided in (22) can be further simplified. Making a change of variable $y = \cos(k_x\Delta)$

and using $\mathrm{d}y/\sqrt{1-y^2} = -\mathrm{d}k_x\Delta$, $\cos(m\cos^{-1}y) = T_m(y)$, where $T_m(\cdot)$ is the Chebyshev polynomial of the first kind of order m, we can show that

$$\psi_d(m\Delta, s\epsilon)\Delta = \frac{K_2}{\pi}\int_{-1}^{1}\frac{1}{\sqrt{1-y^2}}\left\{U_s\left(\frac{y}{\sqrt{2}}\right)T_m(y) - \frac{1}{\sqrt{2}}U_{s-1}\left(\frac{y}{\sqrt{2}}\right)\right.$$

$$\left. \times [T_{m-1}(y) + \mathrm{i}T_{m+1}(y)]\right\}\mathrm{d}y. \tag{23}$$

From the even and odd properties of Chebyshev polynomials, it can be deduced that for $s = 2r$ and $m = 2n - 1$ (or vice versa), the integral in (23) vanishes implying that $\psi_d[(2n-1)\Delta, 2r\epsilon] = 0$ in this special case.

Other interesting identities can be derived starting from (22). Using the relation $U_s(1/\sqrt{2}) = U_s[\cos(\pi/4)] = \sin(s\pi/4) + \cos(s\pi/4)$, one can readily see that

$$\sum_{m=-\infty}^{\infty}\psi_d(m\Delta, s\epsilon)\Delta = \mathrm{e}^{-\mathrm{i}\pi s/4}\left[\Gamma_2(0) + \mathrm{i}\Gamma_1(0)\right]. \tag{24}$$

Hence, unlike $w_1\Delta$, the quantities $q_1\Delta$ and $q_2\Delta$ can be of alternating signs and do not represent true probability mass functions.

Ord [11] has shown that eight different continuous functions are embedded into the discrete functions q_1 and q_2. We will focus on the continuous function that would result from choosing $x = 2n\Delta$, $n = 0, \pm1, \pm2, \ldots$, and $t = 8r\epsilon$, $r = 0, 1, 2, \ldots$, in the discrete functions q_1 and q_2. We show that ψ_d satisfies the Schrödinger equation for $m = 2n$, $s = 8r$ in the limit as $\Delta \to 0$, $\epsilon \to 0$, $n \to \infty$, $r \to \infty$ such that $\Delta^2/2\epsilon = D$. The following identities [23, 27] involving Chebyshev polynomials will be utilized in subsequent development:

$$zU_{s-1}(z) = U_s(z) - T_s(z) \tag{25}$$

$$\frac{\mathrm{d}}{\mathrm{d}z}T_s(z) = sU_{s-1}(z) \tag{26}$$

$$T_s\left(\frac{1}{\sqrt{2}}\right) = \cos\left(\frac{\pi s}{4}\right), \qquad (1-z^2)T_s''(z) - zT_s'(z) + s^2T_s(z) = 0 \tag{27}$$

$$U_{s-1}\left(\frac{1}{\sqrt{2}}\right) = \sqrt{2}\sin\left(\frac{\pi s}{4}\right), \qquad (1-z^2)U_s''(z) - 3zU_s'(z) + s(s+2)U_s(z) = 0, \tag{28}$$

where a prime denotes differentiation with respect to the argument. For the purpose of investigating the continuum limits, we would like to cast (22) in a form more suitable for asymptotic analysis. The last term in (22) involving $U_{s-1}(\cdot)$ can be replaced with $\mathrm{d}T_s(\cdot)/\mathrm{d}k_x$ on using the second relation (26) to yield

$$\frac{\sin k_x\Delta}{\sqrt{2}}U_{s-1}\left(\frac{\cos k_x\Delta}{\sqrt{2}}\right) = \frac{-1}{s\Delta}\frac{\mathrm{d}}{\mathrm{d}k_x}T_s\left(\frac{\cos k_x\Delta}{\sqrt{2}}\right). \tag{29}$$

This term is then integrated by parts and simplified using the periodicity condition $\Gamma_j(\pi/\Delta) = \Gamma_j(-\pi/\Delta)$, $j = 1, 2$. A convenient expression for the evaluation of $\psi_d(m\Delta, s\epsilon)$ is then obtained as

$$\psi_d(m\Delta, s\epsilon) = \frac{1}{2\pi}\int_{-\pi/\Delta}^{\pi/\Delta}\mathrm{e}^{\mathrm{i}mk_x\Delta}\left\{[\Gamma_1(k_x) - \mathrm{i}\Gamma_2(k_x)]U_s\left(\frac{\cos k_x\Delta}{\sqrt{2}}\right)\right.$$

$$+ (1+\mathrm{i})\left(\left[1 + \mathrm{i}\frac{m}{s}\right]\Gamma_2(k_x) + \left[\mathrm{i} + \frac{m}{s}\right]\Gamma_1(k_x)\right)T_s\left(\frac{\cos k_x\Delta}{\sqrt{2}}\right)$$

$$\left. + \frac{1+\mathrm{i}}{s\Delta}[\Gamma_2'(k_x) - \mathrm{i}\Gamma_1'(k_x)]T_s\left(\frac{\cos k_x\Delta}{\sqrt{2}}\right)\right\}\mathrm{d}k_x, \tag{30}$$

8

which is also more amenable to asymptotic analysis than (22). In the special case of $\Gamma_1(k_x) = 0, \Gamma_2(k_x) = K_2$ and for $m/s \to 0$ (small spatial locations and large times) we move on using (25) that

$$\psi_d(m\Delta, s\epsilon) = \frac{K_2}{2\pi} \int_{-\pi/\Delta}^{\pi/\Delta} e^{imk_x\Delta} \left[T_s\left(\frac{\cos k_x\Delta}{\sqrt{2}}\right) - i\frac{\cos k_x\Delta}{\sqrt{2}} U_{s-1}\left(\frac{\cos k_x\Delta}{\sqrt{2}}\right) \right] dk_x. \quad (31)$$

We now perform an asymptotic analysis for small $k_x\Delta$ in (31) and show that $\psi_d(2n\Delta, 8r\epsilon)$ satisfies the Schrödinger equation. To this end, we note the following Taylor series expansions which are obtained by making use of (26)–(28):

$$\cos k_x\Delta \sim 1 - \frac{k_x^2\Delta^2}{2} + \frac{(k_x\Delta)^4}{4!} + \cdots \quad (32)$$

$$T_s\left(\frac{\cos k_x\Delta}{\sqrt{2}}\right) \sim \cos\left(\frac{\pi s}{4}\right) - \frac{k_x^2\Delta^2 s}{2}\sin\left(\frac{\pi s}{4}\right) - \frac{(k_x\Delta)^4 s^2}{4!}$$

$$\times \left[3\cos\left(\frac{s\pi}{4}\right) - \frac{4}{s}\sin\left(\frac{s\pi}{4}\right) \right] + \cdots \quad (33)$$

$$\frac{1}{\sqrt{2}} U_{s-1}\left(\frac{\cos k_x\Delta}{\sqrt{2}}\right) \sim \sin\left(\frac{\pi s}{4}\right) + \frac{k_x^2\Delta^2 s}{2}\left[\cos\left(\frac{\pi s}{4}\right) - \frac{1}{s}\sin\left(\frac{\pi s}{4}\right)\right]$$

$$+ \frac{(k_x\Delta)^4}{4!}\left[(10 - 3(s^2 - 1))\sin\left(\frac{\pi s}{4}\right) - 10s\cos\left(\frac{\pi s}{4}\right)\right] + \cdots \quad (34)$$

Inserting (32)–(34) into (31) and choosing $s = 8r, \Delta^2 = 2D\epsilon, s\epsilon = t, m\Delta = x, s \to \infty$, $m \to \infty, \Delta \to 0, \epsilon \to 0$, we arrive at the desired result:

$$\psi_d(x, t) = q_2(x, t) + iq_1(x, t) \sim \frac{K_2}{2\pi} \int_{-\infty}^{\infty} \left(1 - iDk_x^2 t - \frac{k_x^4 D^2 t^2}{2!} + \cdots\right) e^{ik_x x} \, dk_x$$

$$= \frac{K_2}{2\pi} \int_{-\infty}^{\infty} e^{-iDk_x^2 t} e^{ik_x x} \, dk_x. \quad (35)$$

Equation (35) is the spectral representation of the Green's function corresponding to the Schrödinger equation $\partial\psi/\partial t = iD\partial^2\psi/\partial x^2$ with the impulsive initial condition $\psi(x, t = 0^+) = K_2\delta(x)$. It has the exact solution

$$\psi(x, t) = \frac{K_2}{\sqrt{4\pi iDt}} e^{ix^2/4Dt}. \quad (36)$$

To reinforce to the reader that the plots of the transitional probabilities (q_1, q_2) do resemble the solutions of the free Schrödinger equation, we show in figure 2*a* comparison of the real, $\Re$, and imaginary, $\Im$, parts of the exact solution (36) of the Schrödinger equation with the partial solution (q_1, q_2) of the 4RW. The numerical solutions shown in the figure for ψ_d are on a discrete spacetime $(x = m\Delta, t = s\epsilon)$ and have been computed using (31) with the iFFT algorithm [22] with size $s = 2^{13} = 8192$. It is seen that the 4RW produces solutions of oscillatory type with both positive and negative excursions for the expectations q_1 and q_2, which are in excellent agreement with the analytical results for small $\frac{m}{s}$. This is in contrast to the quantity w_1 shown in figure 1, which, behaving like the solution of the diffusion equation, decays exponentially in space and always remains positive.
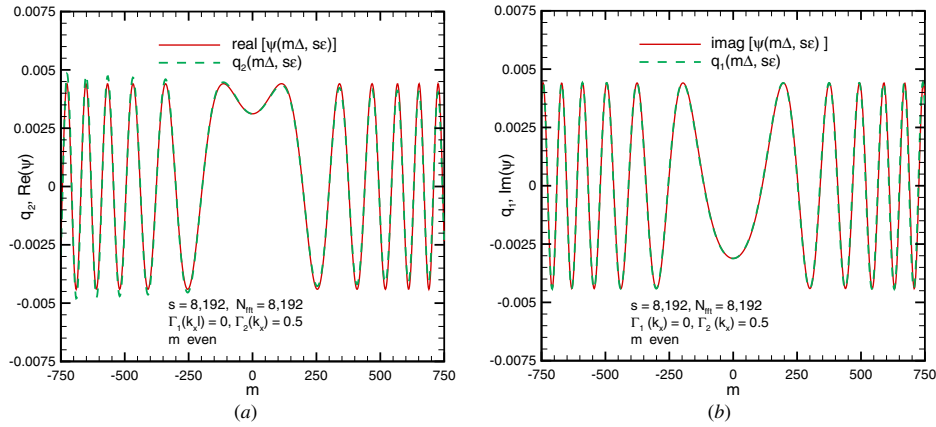
9

Figure 2. Comparison of the exact solution of Schrödinger equation with the discrete solution of a 4RW for an impulsive initial condition. (*a*) $q_2(m\Delta, s\epsilon)$, $\Re\{\psi(m\Delta, s\epsilon)\}$ and (*b*) $q_1(m\Delta, s\epsilon)$, $\Im\{\psi(m\Delta, s\epsilon)\}$.

5. Summary

By considering a multistate random walk on a discrete lattice, expressions have been derived for the various transitional probabilities using the concept of generating functions. A 2D transform involving Fourier transformation in space and the *z*-transformation in time is employed to accomplish this. The transitional probabilities governing particle motion are expressed in terms of integrals involving trigonometric functions in the case of the diffusion equation, and involving Chebyshev polynomials of the first and second kinds in the case of the Schrödinger equation. Closed-form expressions have been given for particular cases of the initial conditions. The continuum limits of the diffusion equation and Schrödinger equation have been shown to follow directly from these transitional probabilities through the performance of appropriate asymptotic analysis. The present analysis consisting of the *z*-transform along the time axis and Fourier transform along the spatial axis is most suitable for studying linear difference equations with constant coefficients. In the 4RW model, this would correspond to the free Schrödinger equation. The important extension of this analysis to higher dimensions is worth exploring and would be taken up in the future. The incorporation of a smooth potential field in the Schrödinger equation into the 4RW model has already been addressed by Ord in [19] and the study of its transitional probabilities will be taken up in a separate paper using a different approach.

Acknowledgments

References

[1] Nelson E 1966 Derivation of the Schrödinger equation from Newtonian mechanics *Phys. Rev.* **150** 1079–85

[2] Nelson E 2001 *Dynamical Theories of Brownian Motion* 2nd edn (Princeton, NJ: Princeton University Press)
     web edition at http://www.math.princeton.edu/nelson/books.html
[3] Nelson E 1985 *Quantum Fluctuations* (Princeton, NJ: Princeton University Press)
[4] Nagasawa M 1993 *Schrödinger Equations and Diffusion Theory* (Boston: Birkhauser)
[5] Nagasawa M 2000 *Stochastic Processes in Quantum Physics* (Boston: Birkhauser Verlag)
[6] Nottale L and Schneider J 1984 Fractals and non-standard analysis *J. Math. Phys.* **25** 1296–300
[7] Ord G N 1983 Fractal spacetime: a geometric analogue of relativistic quantum mechanics *J. Phys. A: Math. Gen.*
     16 1869–84
[8] Nottale L 1995 Scale relativity, fractal space-time and quantum mechanics *Quantum Mechanics, Diffusion and
     Chaotic Fractals* ed M S El Naschie, O E Rossler and I Prigogine (New York: Elsevier)
[9] El Naschie M S 1995 Quantum measurement, information, diffusion and cantorian geodesics *Quantum
     Mechanics, Diffusion and Chaotic Fractals* ed M S El Naschie, O E Rossler and I Prigogine (New York:
     Elsevier Science)
[10] Ord G N 1996 The Schrödinger and diffusion propagators coexisting on a lattice *J. Phys. A: Math. Gen.*
     29 L123–8
[11] Ord G N and Deakin A S 1996 Random walks, continuum limits, and Schrödinger's equation *Phys. Rev.*
     A **154** 3772–78
[12] Ord G N and Deakin A S 1997 Random walks and Schrödinger's equation in (2+1) dimensions *J. Phys. A:
     Math. Gen.* **30** 819–30
[13] Aharonov Y, Davidovich L and Zagury N 1993 Quantum random walks *Phys. Rev.* A **48** 1687–90
[14] Aslangul C 2005 Quantum dynamics of a particle with a spin-dependent velocity *J. Phys. A: Math. Gen.* **38** 1–16
[15] Jensen F B, Kuperman W A, Porter M B and Schmidt H 1994 *Computational Ocean Acoustics* (New York:
     Springer)
[16] Levy M F 2000 *Parabolic Equation Methods for Electromagnetic Wave Propagation* (London: IEE Press)
[17] Budaev B V and Bogy D B 2002 Application of random walk methods to wave propagation *Quart. J. Mech.
     Appl. Math.* **55** 206–26
[18] Janaswamy R 2007 Solution of BVPs in electrodynamics by stochastic methods *IEEE Applied Electromagnetics
     Conf.* vol 1 *(Kolkata, India, 19–20 Dec. 2007)*
[19] Ord G N 1996 Schrödinger's equation and discrete random walks in a potential field *Ann. Phys.* **250** 63–8
[20] Montroll E W 1965 Random walks on lattices-II *J. Math. Phys.* **6** 167–81
[21] Barber M N and Ninham B W 1970 *Random and Restricted Walks* (New York: Gordan and Breach)
[22] Rabiner R R and Gold B 1975 *Theory and Application of Digital Signal Processing* (Englewood Cliffs, NJ:
     Prentice-Hall)
[23] Gradshteyn L S and Ryzhik I S 2000 *Table of Integrals, Series, and Products* 6th edn (New York: Academic)
[24] Feller W 1970 *An Introduction to Probability Theory and Its Applications* vol II 2nd edn (New York: Wiley)
[25] van Kampen V G 2007 *Stochastic Processes in Physics and Chemistry* 3rd edn (New York: North-Holland)
[26] Barton G 1989 *Elements of Green's Functions and Propagation* (New York: Oxford University Press)
[27] Abramowitz M and Stegun I A 1970 *Handbook of Mathematical Functions* (New York: Dover)

Transparent Boundary Condition for the Parabolic Equation Modeled by the 4RW

Ramakrishna Janaswamy, *Fellow, IEEE*

Abstract—Transparent boundary condition in a 2D-space is presented for the four-state random walk (4RW) model that is used in treating the standard parabolic equation by stochastic methods. The boundary condition is exact for the discrete 4RW model, is of explicit type, and relates the field in the spectral domain at the boundary point in terms of the field at a previous interior point via a spectral transfer function. In the spatial domain, the domain of influence for the boundary condition is directly proportional to the "time" elapsed. By performing various approximations to the transfer function, several approximate absorbing boundary conditions can be derived that have much more limited domain of influence.

Index Terms—Generating function, parabolic equation, random walk, Schrödinger equation, transform methods, transparent boundary condition.

I. INTRODUCTION

PARABOLIC EQUATION (PE) is used widely in several areas—including radiowave propagation, underwater acoustics, fiber optic propagation, etc.—to study propagation of unidirectional waves in a variety of environments [5], [8], [11]. Its form is very similar to the Schrödinger equation in which the wavefunction, temporal variable, and the potential take the respective places of the reduced field, the axial coordinate, and the modified refractive index of the PE. When solving the PE or Schrödinger equation in unbounded regions by differential or difference equation methods, one has to first restrict the region to a finite size and simulate an unbounded region by imposing boundary conditions on the truncated domain. If these boundary conditions exactly simulate an unbounded exterior region as far as the interior problem is concerned, they are termed as exact or transparent boundary conditions. Transparent boundary conditions can be devised for the original partial differential equation or to its discretized version, and this has been done by several works in the past: [2], [4], [9], [10], [13], and [1]. ([1] and [4] contain many works outside the traditional electromagnetic area where such development took place.) For a number of reasons, there is an interest to treat the PE by stochastic techniques, wherein the desired field is obtained by performing averages

over several realizations of Brownian motion or its discrete counterpart of random walk traversing the problem domain [6]. A direct application of stochastic techniques to the PE as done in [3] necessitates analytical continuation of fields and boundary data, only possible for very limited problems, that is highly undesirable. The four-state random walk (4RW) model, originally developed by Ord [12] to provide a macroscopic model for the Schrödinger equation, alleviates this limitation and results in the same second-order accurate discretization scheme for the PE as the Crank–Nicolson scheme. Numerical schemes are currently being developed using the 4RW model to study wireless propagation problems in open domains, and it is the purpose of this letter to derive transparent boundary conditions for this model by considering 2D propagation in a 1 + 1-dimensional space. Detailed numerical solutions for propagation over terrain and rough surfaces, and in inhomogeneous atmosphere by the 4RW model will be presented in a future paper. In the next section, we begin with a brief introduction of the 4RW model, followed by the development of the exact boundary condition.

II. TRANSPARENT BOUNDARY CONDITION FOR 4RW

Consider the standard parabolic equation in the reduced field variable $\psi(x, t)$:

$$\frac{\partial \psi}{\partial t} = \frac{i}{2k_0} \frac{\partial^2 \psi}{\partial x^2} + ik_0 V \psi \qquad (1)$$

which constitutes a narrow angle approximation to the Helmholtz equation for time-harmonic waves ($e^{-ik_0\tau}$ time convention in the normalized time variable τ) with wavenumber $k_0 = 2\pi/\lambda$ propagating in the t-x plane, where λ is the operating wavelength and $V(x, t)$ is a complex-valued function proportional to the modified refractive index (or potential for the Schrödinger equation) of the medium. Because this work relies heavily on the random walk literature pertaining to the Schrödinger equation, we shall refer to t as the "time" coordinate even though it represents the axial space coordinate in wave propagation problems. The variable x represents the lateral spatial coordinate and $i = \sqrt{-1}$. Presence of the first-order derivative in time enables the solution of (1) to proceed with the specification of initial conditions at $t = 0$. It is assumed that all sources at initial time are confined to the region $x < 0$ (Region I) and that the potential V assumes a constant value $V(x, t) = V_c$ for $x \geq 0$ (Region II). Our interest is to derive an artificial boundary condition imposed at $x = 0$ for a discretized version of (1) that simulates free space as far as Region I is concerned. For simplicity and no loss in generality, we first consider the case of $V_c = 0$ and discuss the solution for the nonzero case at the end. For treatment by stochastic

The author is with the Department of Electrical and Computer Engineering, University of Massachusetts, Amherst, MA 01003 USA (e-mail: janaswamy@ecs.umass.edu).

methods, (1) is discretized as per the 4RW model, which, like the Crank-Nicolson finite-difference scheme, results in a second-order accurate (in space and time) scheme [12]. For a particle moving on a discrete lattice and subject to random collisions, the transitional probabilities in the 4RW at the discrete space–time point ($x = m\Delta, t = s\epsilon$) are of the form [7], [12]

$$E_t \begin{pmatrix} q_1 \\ q_2 \end{pmatrix} = \frac{1}{\sqrt{2}} \begin{pmatrix} E_x^{-1} & -E_x \\ E_x^{-1} & E_x \end{pmatrix} \begin{pmatrix} q_1 \\ q_2 \end{pmatrix} \quad (2)$$

where $q_1(m\Delta, s\epsilon) = 2^{s/2}[p_1(m\Delta, s\epsilon) - p_3(m\Delta, s\epsilon)]$, $q_2(m\Delta, s\epsilon) = 2^{s/2}[p_2(m\Delta, s\epsilon) - p_4(m\Delta, s\epsilon)]$, and $p_\mu(m\Delta, s\epsilon)\Delta, \mu = 1, \ldots, 4$, is the probability that a particle is in state μ at the space-time point $(m\Delta, s\epsilon), m = 0, \pm1, \pm2, \ldots,$ $s = 0, 1, \ldots$. The particle changes its direction of motion with every collision but changes its parity or spin at every other collision. The combination of two directions of motion and two states of spin constitutes the four states in the model. It has been shown in [12] that such a 4RW encompasses the diffusion as well as Schrödinger equations and that $\psi = q_2 + iq_1$ is the Schrödinger wave function in the discrete case. The relationship between the temporal and spatial steps of the form $\epsilon = k_0\Delta^2$ implied in the 4RW model assures the aforementioned second-order accuracy in space. For waves propagating within $\pm15°$ about the axial direction, the lateral space step is usually restricted to $\Delta \lesssim 2\lambda$ [8], resulting in $\epsilon \lesssim 8\pi\lambda$, values which are consistent with those used in the normal finite-difference or Fourier split-step schemes [8] used to solve the PE.

The operators E_x and E_t in (2) are, respectively, the spatial and temporal advancing operators and are defined mathematically as $E_x^{\pm1} p_\mu(m\Delta, s\epsilon) = p_\mu[(m \pm 1)\Delta, s\epsilon]$ and $E_t p_\mu(m\Delta, s\epsilon) = p_\mu[m\Delta, (s + 1)\epsilon]$. It is assumed in (2) that the random walk is nonpersistent and the probabilities that a particle maintains or changes its direction at the next time step are the same. For brevity we will denote $\psi(m\Delta, s\epsilon)$ as simply $\psi(m, s)$. As in our previous studies, we will assume that the number of right-going particles is the same as those going to the left at time $t = 0$ and focus on deriving transparent boundary conditions for the wave function $\psi(m, s)$. The boundary at $m = 0$ separates Region I from Region II and it is further assumed for convenience that $\psi(m, 0) \equiv 0$ for $m \geq -2$. Consider a discrete function $v(m, s)$ and its temporal transform $\hat{v}(m, z)$ as defined in [7]

$$\hat{v}(m, z) = \sum_{s=0}^{\infty} v(m, s)z^s \equiv \mathcal{Z}v. \quad (3)$$

The quantity $\hat{v}(m, z)$ may be thought of as the discrete version of the Laplace transform of v. The inverse relation is defined as

$$v(m, s) = \frac{1}{2\pi i} \oint_{C_z} \frac{\hat{v}(m, z)}{z^{s+1}} dz \equiv \mathcal{Z}^{-1}\hat{v} \quad (4)$$

where C_z is a closed contour around the origin in the complex z-plane that encloses only the singularities at the origin. The symbols $\mathcal{Z}$ and $\mathcal{Z}^{-1}$ denote the temporal transform and its inverse respectively. The transformed variable $\hat{v}(m, z)$ is also referred to as the *generating function* within the random walk community [14]. If $v_1(m, s)$ and $v_s(m, s)$ are two temporal (and

causal) functions with respective generating functions $\hat{v}_1(m, z)$ and $\hat{v}_2(m, z)$, the following shift and convolution properties, respectively, can be readily established:

$$\mathcal{Z}[E_t v_1] = z^{-1}[\hat{v}_1(m, z) - v_1(m, 0)] \quad (5)$$

$$\mathcal{Z}^{-1}[\hat{v}_1 \hat{v}_2] = \sum_{k=0}^{s} v_1(m, s - k)v_2(m, k). \quad (6)$$

Applying the temporal transform to (2) and making use of the shift property (5), and carrying out some algebraic manipulations, we arrive at the following equations for the generating function in terms of initial data:

$$[1 - \sqrt{2}zD_x + z^2]\hat{\psi}(m, z) = \psi(m, 0)$$
$$- \frac{z}{\sqrt{2}}\left[\left(E_x^{-1} + iE_x\right)q_2(m, 0) + \left(iE_x - E_x^{-1}\right)q_1(m, 0)\right] \quad (7)$$

where $D_x = (E_x + E_x^{-1})/2$ is the discrete averaging operator. The right-hand side in (7) is identically zero for Region II, and a knowledge of the general solution in this region permits the derivation of transparent boundary condition. A general solution of (7) in Region II will be of the form $\hat{\psi}(m, z) = A[\hat{\nu}(z)]^m$ with A constant. The function $\hat{\nu}(z)$ is then determined from (7) as

$$\hat{\nu}(z) = \frac{1}{\sqrt{2}z}[1 + z^2 + \sqrt{1 + z^4}]. \quad (8)$$

We are interested in the solution that remains bounded for large m in Region II, which imposes the condition $|\hat{\nu}(z)| \leq 1$. Due to the presence of the radical sign, the function defined by (8) will be multiple-valued, resulting in two branches of the solution. These two solutions will cross over in the complex plane unless care is taken to define each analytically by considering a double-sheeted complex plane. The two sheets intersect at the branch cuts defined by the curve $|\hat{\nu}(z)| = 1$ so as to separate the proper solution $|\hat{\nu}(z)| \leq 1$ from the improper one $|\hat{\nu}(z)| > 1$. It is more illuminating to first study the branch cuts in a transformed complex plane $\zeta = \zeta_r + i\zeta_i = z^2$, in which the branch points occur at $\zeta = \pm i$. In the z-plane, the branch points occur at $z_k = \exp[i(2k - 1)\pi/4], k = 1, \ldots, 4$. With these branch cuts, the top sheet of the complex z-plane is chosen such that $\sqrt{1 + z^4} = \sqrt{\prod_{k=1}^{4}(z - z_k)} = -1$ at $z = 0$. A straightforward but tedious analysis reveals that the branch cut in the ζ-plane is given by the semicircle $|\zeta| = 1$, with the real part $\zeta_r < 0$. The branch cuts in the ζ- and z- planes are shown in Fig. 1. We denote the proper branch by the symbol $\hat{\nu}_1(z)$ and the other branch by the symbol $\hat{\nu}_2(z)$. For the purpose of numerical calculations, one may set $\hat{\nu}_{\frac{1}{2}}(z) = [1 + z^2 \mp \sqrt{1 + z^4}]/\sqrt{2}z$. Clearly $\hat{\nu}_1(z)\hat{\nu}_2(z) = 1$. The proper solution in Region II is now given by $\hat{\psi}(m, z) = A[\hat{\nu}_1(z)]^m$, which implies that

$$\hat{\psi}(0, z) = \hat{\nu}_1(z)\hat{\psi}(-1, z). \quad (9)$$

Equation (9) is the frequency domain representation of the transparent boundary condition that simulates free space for the interior region $m < 0$. The function $\hat{\nu}(z)$ may be interpreted as a *transfer function*, which relates the input and output functions $\hat{\psi}(-1, z)$ and $\hat{\psi}(0, z)$, respectively. For the purpose of numerical implementations, it is necessary to prescribe the boundary condition in the temporal domain. From Fig. 1, it is clear that

the function $\hat{\nu}_1(z)$ is analytic near the origin. The inverse transform of $\hat{\nu}_1(z)$ involves integration around the closed contour C_z and is facilitated by performing a Taylor series expansion of $\sqrt{1+z^4}$ near the origin. The infinite series representation of $\hat{\nu}_1(z)$ can then be easily determined as

$$\hat{\nu}_1(z) = \frac{z}{\sqrt{2}} - \frac{z^3}{2\sqrt{2}} + \sum_{r=0}^{\infty} a_r z^{4r+7} \qquad (10)$$

where

$$a_r = \frac{(-1)^r (2r+1)!}{4^{r+1} r! (r+2)! \sqrt{2}} = O(r^{-3/2}), \quad r \to \infty. \qquad (11)$$

Making use of the relation

$$\oint_{C_z} z^k / z^{s+1} dz = 2\pi i \delta_s^k$$

where δ_s^k is the Kronecker's delta, we arrive at the corresponding temporal function

$$\nu_1(s) = \frac{1}{\sqrt{2}} \delta_s^1 - \frac{1}{2\sqrt{2}} \delta_s^3 + \sum_{r=0}^{\infty} a_r \delta_s^{4r+7}. \qquad (12)$$

Finally, a "time"-domain transparent boundary condition is obtained by using the convolution property (6) in (9)

$$\psi(0,s) = \frac{1}{\sqrt{2}} \psi(-1, s-1) - \frac{1}{2\sqrt{2}} \psi(-1, s-3)$$
$$+ \sum_{r=0}^{R} a_r \psi(-1, s-7-4r) \qquad (13)$$

where $R = \lfloor (s-7)/4 \rfloor$ is the interger-valued floor function of $(s-7)/4$. Obviously, the summation term will only exist when $s \geq 7$. Note that the presence of a term z^k in the series representation of $\hat{\nu}_1(z)$ results in a delayed field $\psi(-1, s-k)$ in the temporal representation of the boundary condition. Equation (13), consisting of a finite series, is the exact discrete boundary condition for terminating the computational domain of the 4RW model and is based on an infinite series representation of the transfer function in a region analytic about the origin. Furthermore, it is of explicit type wherein the field at $(0,s)$ is expressed in terms of the historical field at $(-1, s-k)$, $k > 0$. It is also seen that the number of terms in (13) will increase linearly with s. To reinforce to the reader its accuracy, we place initial sources $q_1(m,0)\Delta = \Gamma_1 \delta_m^{m_0}$, $q_2(m,0)\Delta = \Gamma_2 \delta_m^{m_0}$ with constant Γ_1 and Γ_2 and compare the exact solution of the field $\psi_e(0,s)$ as determined from the expressions in [7] with the solution $\psi_b(0,s)$ obtained by substituting the exact solution into the right hand side of (13). Note that the earliest "time" at which an impulse placed initially at $m_0 = -28$ will arrive at $m = 0$ is $s = 28$. The two solutions plotted in Fig. 2 for $s \geq 32$ are seen to be virtually on top of each other.

It is possible to derive a hierarchy of approximate boundary conditions by considering various approximations to the transfer function $\hat{\nu}_1(z)$. For example, one may perform a rational approximation to the function $\hat{\nu}_1(z)$ and obtain successively higher order boundary conditions. A zeroth order boundary condition is obtained by using $\hat{\nu}_1(z) = z/\sqrt{2}$ and
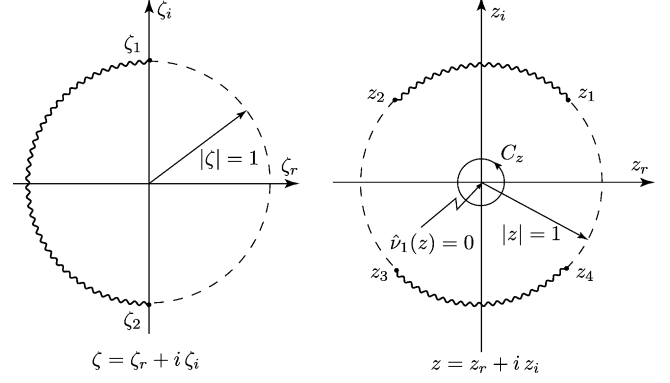

Fig. 1. Branch cuts in the complex $\zeta = z^2$ and z planes defining $|\hat{\nu}_1(z)| = 1$. The branch points in the ζ-plane occur at $\zeta_1 = i$ and $\zeta_2 = -i$ and those in the z-plane at $z_k = e^{i(2k-1)\pi/4}$, $k = 1, \ldots, 4$. Branch cuts are shown as wiggly lines.
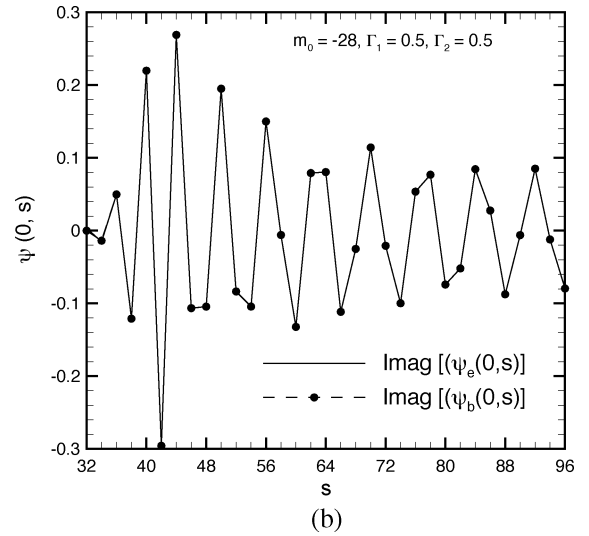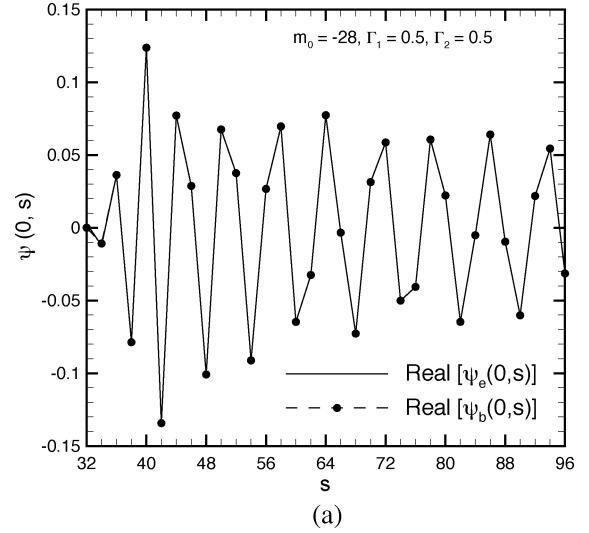

(a)

(b)

Fig. 2. True field in unbounded medium and that obtained from (13). (a) Real part of $\psi(0,s)$. (b) Imaginary part of $\psi(0,s)$.

reads $\sqrt{2}\psi(0,s) = \psi(-1, s-1)$. A better approximation uses $\hat{\nu}_1(z) = \sqrt{2}z/(2+z^2)$ and results in the boundary condition $2\psi(0,s) + \psi(0, s-2) = \sqrt{2}\psi(-1, s-1)$. Approximations

in terms of special functions such as Legendre polynomials are also possible.

It is straightforward to handle the case with nonzero V_c by writing the solution $\phi(x, t)$ of (1) as $\phi(x, t) = \psi(x, t) \exp(ik_0 V_c t)$, resulting in $\phi(m, s) = r_1^s \psi(m, s)$ with $r_1 = \exp(ik_0 \epsilon V_c)$. The boundary condition (9) continues to be valid for the quantity $\hat{\psi}$. The spectral domain boundary condition in terms of the actual field becomes $\hat{\phi}(0, z) = \hat{\nu}_1(r_1 z)\hat{\phi}(-1, z)$. In the temporal domain we get the corresponding equation

$$\phi(0, s) = \frac{r_1}{\sqrt{2}}\phi(-1, s - 1) - \frac{r_1^3}{2\sqrt{2}}\phi(-1, s - 3)$$
$$+ \sum_{r=0}^{R} a_r r_1^{4r+7}\phi(-1, s - 7 - 4r). \quad (14)$$

Obviously, (14) reduces to (13) for $V_c = 0$ (or $r_1 = 1$).

III. Conclusion

Transparent boundary condition has been presented for the 4RW model used to represent a PE in stochastic methods. The boundary condition, given in the form of a finite series, involves specification of the field at a boundary point in terms of the historical field at immediate interior points. Several approximate boundary conditions can be derived from it based on a rational or other approximations to the transfer function.

References

[1] A. Arnold, M. Ehrhardt, and I. Sofronov, "Discrete transparent boundary conditions for the Schrödinger equation: Fast calculation, approximation, and stability," *Commun. Math. Sci.*, vol. 1, no. 3, pp. 501–556, 2003.

[2] V. A. Baskakov and A. V. Popov, "Implementation of transparent boundaries for numerical solution of the Schrödinger equation," *Wave Motion*, vol. 14, no. 1, pp. 123–128, Jan. 1991.

[3] B. V. Budaev and D. B. B. Bogy, "Application of random walk methods to wave propagation," *Q. J. Mech. Appl. Math.*, vol. 55, no. 2, pp. 209–226, 2002.

[4] M. Ehrhardt and A. Arnold, "Discrete transparent boundary conditions for the Schrödinger equation," *Riv. Mat. Univ. Parma*, vol. 6, pp. 57–108, 2001.

[5] V. A. Fock, *Electromagnetic Diffraction and Propagation Problems*. New York: Pergamon Press, 1965.

[6] R. Janaswamy, "Solution of BVPs in electrodynamics by stochastic methods," in *Proc. IEEE Appl. Electromagn. Conf.*, Kolkata, India, Dec. 19–20, 2007 [Online]. Available: http://ieeexplore.ieee.org

[7] R. Janaswamy, "Transitional probabilities for the 4-state random walk on a lattice," *J. Phys. A: Math. Theor.*, vol. 41, Apr. 2008, 155306, (11 pp.).

[8] F. B. Jensen, W. A. Kuperman, M. B. Porter, and H. Schmidt, *Computational Ocean Acoustics*. New York: Springer-Verlag, 1994.

[9] M. F. Levy, "Transparent boundary conditions for parabolic equation solutions of radiowave propagation problems," *IEEE Trans. Antennas Propag.*, vol. 45, no. 1, pp. 66–72, Jan. 1997.

[10] S. W. Marcus, "A generalized impedance method for application of the parabolic approximation to underwater acoustics," *J. Acoust. Soc. Amer.*, vol. 90, no. 1, pp. 391–398, Jul. 1991.

[11] K. Okamoto, *Fundamentals of Optical Waveguides*, 2nd ed. San Diego, CA: Academic, 2006.

[12] G. N. Ord and A. S. Deakin, "Random walks and Schrödinger's equation in $(2 + 1)$ dimensions," *J. Phys. A: Math. Gen.*, vol. 30, pp. 819–830, 1997.

[13] J. S. Papadakis, P. Taroudakis, P. J. Papadakis, and B. Mayfield, "A new method for a realistic treatment of the sea bottom in the parabolic approximation," *J. Acoust. Soc. Amer.*, vol. 92, no. 4, pp. 2030–2038, Oct. 1992.

[14] G. H. Weiss, *Aspects and Applications of the Random Walk*. New York: North-Holland, 1994.

An ADI-PE Approach for Modeling Radio Transmission Loss in Tunnels

Richard Martelly and Ramakrishna Janaswamy, *Fellow, IEEE*

Abstract—Alternate direction implicit (ADI) method is used to study radio wave propagation in tunnels using the parabolic equation (PE). We formulate the ADI technique for use in tunnels with rectangular, circular and arched cross sections and with lossy walls. The electrical parameters of the lossy walls are characterized by an equivalent surface impedance. A vector PE is also formulated for use in tunnels with lossy walls. It is shown that the ADI is more computationally efficient than the Crank Nicolson method. However, boundary conditions become more difficult to model. The boundary conditions of the ADI intermediate planes are given the same boundary conditions as the physical plane and the overall accuracy is reduced. Also, when implementing the ADI in tunnels with circular cross sections the order at which the line by line decomposition occurs becomes important. To validate the ADI-PE, we show simulation results for tunnel test cases with known analytical solutions. Furthermore, the ADI-PE is used to simulate real tunnels in order to compare with experimental data. It is shown that the PE models the electric fields most accurately in real tunnels at large distances, where the lower order modes dominate.

Index Terms—Alternate direction implicit (ADI), parabolic equation, radio wave propagation in tunnels.

I. INTRODUCTION

THE growth of mobile communication systems in recent years has led to increasing interest in the research of radio wave propagation in tunnels. The methods that have been traditionally used to model radiowave propagation in tunnels are modal analysis, geometrical optics and the parabolic equation (PE) approximation.

The modal analysis method and the geometrical optics method both have unacceptable limitations and cannot always be used to solve for the fields in real tunnels [3]–[5]. The modal approach uses a simple field representation comprised of one dominate mode and an infinite number of higher order modes. This representation is not always applicable to real tunnel environments with arbitrary geometries. Also, it is difficult to determine eigenfunctions for real tunnels [4]. The geometrical optics method approximates the field as rays reflected along the direct path of propagation. The geometrical optics method becomes difficult to use for problems at long range because of the large number of reflected waves, and the method fails
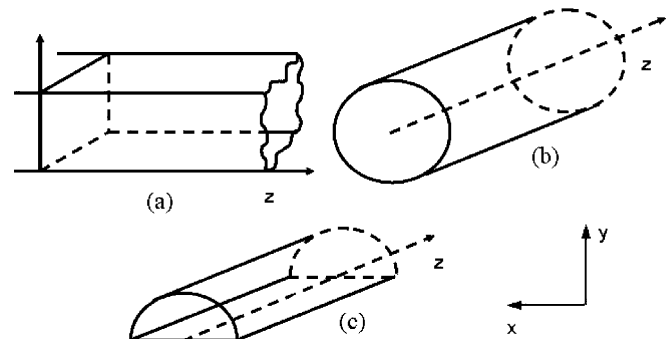
Fig. 1. Tunnels with (a) rectangular, (b) circular and (c) arched profiles.

completely in caustic regions. By comparison, the standard parabolic equation has been shown to accurately model electromagnetic fields in tunnels for waves which travel within $\pm 15°$ to the axis of propagation [2].

Research has been done on the parabolic approximation of radiowave propagation in tunnels by Popov and Zhu [4] and Noori *et al.* [5]. The traditional numerical technique used in previous works is the Crank Nicolson method. The popularity of the Crank Nicolson method is due to the fact that it is stable for any discretization in the transverse plane or along the propagation axis [2]. The major limitation of the CN method is that it requires the solution of sets of simultaneous equations that may become too large to efficiently solve for problems with dense meshes. The alternate direction implicit (ADI) technique was developed to address the problem of computational efficiency. The ADI method has been used extensively in previous works to solve the PE in the form of the heat transfer equation [19]–[22] and in electromagnetics to directly solve Maxwell's equation using the FDTD method [23]–[25].

In this paper we use PE together with the ADI technique to study transmission loss inside tunnels. In Section II, we show how the PE can be used to solve for fields in tunnels with perfectly conducting walls. In this case, we can use a scalar PE and enforce simple Dirichlet or Neumann boundary conditions on the wall. To model waves in tunnels with lossy walls, we must use a vector parabolic equation, as discussed in Section III. A brief introduction of the CN method is given in Section IV. As discussed in Section V, the ADI maintains the unconditional stability of the CN method while reducing computional labor. We develop the ADI to deal with straight tunnels with rectangular, circular and arched profiles, as shown in Fig. 1.

For validation purposes, in Section VI, we examine the accuracy of the scalar parabolic equation when used to solve for fields in (a) square (b) circular (c) semi-circular cylindrical PEC tunnels. Then we examine the accuracy of the vector parabolic

equation when used to solve for fields in (d) square and (e) circular cylindrical tunnels with impedance walls in Section VII. Finally, in Section VIII we compare the ADI simulation results with published measured data for the case of (f) arched cylindrical tunnels.

II. SCALAR PARABOLIC EQUATION

The parabolic equation is an approximation of the Helmholtz equation that assumes wave propagation in predominantly one direction [2]. The PE can be obtained from the Helmholtz equation

$$\left(\frac{\partial^2}{\partial x^2} + \frac{\partial^2}{\partial y^2} + \frac{\partial^2}{\partial z^2} + k_o^2\right)\Psi(x,y,z) = 0 \qquad (1)$$

where Ψ is either the electric or magnetic scalar potential and k_o is the free space wave number. We choose a solution for the scalar potential with a fast varying phase term in the z direction factored out

$$\Psi(x,y,z) = u(x,y,z)e^{-jk_o z}. \qquad (2)$$

where $u(x,y,z)$ is the reduced plane wave solution. The reduced plane wave is slowly varying along the z direction and we can make the following assumption,

$$\left|\frac{\partial^2 u}{\partial z^2}\right| \ll k_o \left|\frac{\partial u}{\partial z}\right|. \qquad (3)$$

Physically, the reduced plane wave represents the lower order modes which travel predominantly along the z-axis. Substituting the plane wave solution into (1), the standard PE follows:

$$\frac{\partial u}{\partial z} = \frac{1}{2jk_o}\left(\frac{\partial^2}{\partial x^2} + \frac{\partial^2}{\partial y^2}\right)u. \qquad (4)$$

The PE reduces the 2nd order z derivative into a first order derivative and, as a result, the PE is easier to implement numerically using finite differences. As shown in [7], the relative error epression of the PE can be shown to be

$$e_{3DPE} = 1 - \cos(\theta) - \frac{\sin^2\theta}{2} \qquad (5)$$

where the angle θ is the angle of propagation measured from the z axis. The level of accuracy will determine the range of angles over which the PE is valid. For this paper, we adopt the traditional angle range of $\pm 15°$. For the angle of $15°$ the relative error is 0.00058. The PE is only valid for waves traveling in the positive z direction at angles within $\pm 15°$ and back scattered waves are ignored [2].

In Section VI, we use the PE to solve for fields in PEC wavegiudes. For these examples, we choose our initial fields so that only modes propagating within $\pm 15°$ are significant. The scalar PE can only be used for tunnels with PEC walls. In Section III, we discuss the modifications that must be made to the PE to deal with tunnels with non-PEC walls.

III. VECTOR PARABOLIC EQUATION

The scalar PE is only valid in cases where the transverse magnetic and electric fields can propagate independantly of each other. This is the case when studying perfect electrically conducting (PEC) waveguides. If Dirichlet boundary conditions are enforced on the waveguide wall, the propagating field will be of the *TM* type, and if Neumann boundary conditions are enforced, then the field will be of the *TE* type.

In realistic tunnels, the walls are typically made up of some lossy material such as concrete and rock. The PE approximation has been shown to model realistic tunnels very accurately over large distances [4]. This is because higher order modes are more severely attenuated over large distances due to multiple reflections. Lower order modes, which propagate at small angles relative to the axis, make the most significant contribution to the field over large distances.

Also, in the case of realistic tunnels, there will exist, in general, coupling between the *TM* and *TE* modes. Unlike the PEC case, we cannot solve the *TE* and *TM* modes independently. We must now develop a vector PE that will take coupling effects into account. Formulation of a vector PE for tunnels with lossy walls and a radius of curvature, ρ, was done by Popov and Zhu [4]. For this paper, we consider only straight tunnels with infinite radius of curvature. Although we will not repeat the details here, we will briefly discuss the vector PE derivation. In [4], the electrical parameters on the tunnel walls are approximated by the Leontovich impedance boundary condition [27]

$$\hat{n} \times \bar{E} = -\bar{Z}\hat{n} \times \left(\hat{n} \times \bar{H}\right) \qquad (6)$$

where $\hat{n}$ is the outward normal on the tunnel wall and Z is the relative surface impedance. For a wall with relative permittivity ϵ_r and conductivity σ_o (in S/m), Z is approximately [18]

$$Z = \frac{\sqrt{\epsilon_{rc} - 1}}{\epsilon_{rc}} \qquad (7)$$

where $\epsilon_{rc} = \epsilon_r - j\sigma_r, \sigma_r = \sigma_o/\omega\epsilon_o$, is the complex permittivity and relative conductivity, respectively. Here we use the grazing angle approximation for the surface impedance because the rays that make the significant contributions to the field at large distances propagate at small angles relative to the axis of propagation.

Starting with normalized Maxwell's equations

$$\nabla \times \eta_o\bar{h} = \nabla \times \bar{H} = jk_o\bar{E}$$

and

$$\nabla \times \bar{E} = -jk_o\eta_o\bar{h} = -jk_o\bar{H} \qquad (8)$$

where η_o is the intrinsic impedance, $\bar{E}$ is in V/m, $\bar{h}$ is in A/m and $\bar{H}$ is the normalized magnetic field and is in $A\Omega/m$. We can define a six component vector

$$\Pi = [E_x, E_y, E_z, H_x, H_y, H_z]^T. \qquad (9)$$

We can then use the following asymptotic ansatz

$$\Pi = \bar{U} \exp\left(\frac{-j\zeta\Phi}{\nu^3}\right) \qquad (10)$$

where

$$\zeta = \sqrt{\frac{k_o^2 D^3}{\rho}} \text{ and } \nu = \sqrt{\frac{D}{\rho}} \ll 1 \qquad (11)$$

and D is the tunnel width [26]. The eikonal Φ is a general second order polynomial of ν and the vector amplitude U is an asymptotic series in powers of ν. Directly substituting the ansatz into Maxwell's equation and equating terms of the same order of ν, we can define the eikonal and find the vector PE [4] for the straight waveguide

$$2k_o j \frac{\partial \bar{W}}{\partial z} = \frac{\partial^2 \bar{W}}{\partial x^2} + \frac{\partial^2 \bar{W}}{\partial y^2} \qquad (12)$$

where $\bar{W}$ is the attenuation function which describes the complex wave amplitude of the approximate plane wave $\exp(-jk_o z)$ propagating along the waveguide axis. $\bar{W}$ is related to the electric field transverse to the direction of propagation by

$$E_{\text{trans}} = (E_x, E_y)^T = \bar{W} e^{-jk_o z}. \qquad (13)$$

Substituting the ansatz into the IBC [see (6)], and equating like terms, we get [4], [28]

$$\bar{W}|_{\text{boundary}} = \frac{j}{k_o} \bar{\bar{T}}_o \bar{\bar{G}}_o \bar{\bar{T}}_o \frac{\partial \bar{W}}{\partial n}|_{\text{boundary}} \qquad (14)$$

where $\bar{\bar{T}}_o$ and $\bar{\bar{G}}_o$ are matrices defined by

$$\bar{\bar{T}}_o = \begin{pmatrix} n_x & n_z \\ n_y & -n_x \end{pmatrix} \text{ and } \bar{\bar{G}}_o = \begin{pmatrix} \frac{1}{Z} & 0 \\ 0 & Z \end{pmatrix} \qquad (15)$$

where n_x and n_y are the unit normal vectors. The impedance boundary condition describes the effects of grazing angle reflection, selective mode absorption and depolarization on the waveguide walls [4]. The Crank–Nicolson method has been widely used to model both the scalar and vector PE. In Section IV, we will briefly introduce the Crank–Nicolson method as it will directly lead to the ADI technique.

IV. CRANK–NICOLSON METHOD

The Crank–Nicolson method has been widely used to model electromagnetic wave propagation in tunnels [3]–[5]. The main feature of the Crank–Nicolson method is its stability for any mesh ratio [11], [17]. The enumeration scheme of the marching planes for the Crank–Nicolson method is shown in Fig. 2. The coordinates of the mesh points on the x, y and z axes are denoted by $m\Delta x$, $l\Delta y$ and $n\Delta z$, respectively. The field points on the n and the $n+1$ marching planes are explicitly solved, but the field points on the intermediate plane are never explicitly calculated. The Crank–Nicolson descretization of the standard PE is given by (16), shown at the bottom of the page, which can be re-written as

$$\left(1 - \frac{r_x}{4jk_o}\delta_x - \frac{r_y}{4jk_o}\delta_y\right) u^{n+1}$$
$$= \left(1 + \frac{r_x}{4jk_o}\delta_x + \frac{r_y}{4jk_o}\delta_y\right) u^n \qquad (17)$$

where $r_x = \Delta z/\Delta x^2$ and $r_y = \Delta z/\Delta y^2$ are the mesh ratios, and

$$\delta_x u_{m,l} = u_{m+1,l} - 2u_{m,l} + u_{m-1,l} \qquad (18)$$
$$\delta_y u_{m,l} = u_{m,l+1} - 2u_{m,l} + u_{m,l-1}. \qquad (19)$$

The Crank–Nicolson method is implicit, unconditionally stable, and second order accurate in x, y and z [9]. The Crank–Nicolson difference scheme is centered about the midpoint between the $z = n\Delta z$ and $z = (n+1)\Delta z$ marching planes. The field points of each successive marching plane must be solved in consecutive order at propagation steps of Δz until the field at the desired range is solved. The major limitation of the Crank–Nicolson method is that it becomes computationally intensive in cases that require a very large mesh. As Equation (16) shows, the size of the matrix generated for a problem with N_x mesh points along the x axis and N_y, mesh points along the y axis will be $N_x N_y - 4$ (in Fig. 2, $N_x = N_y = 4$). The elements of the matrix will not be in tridiagonal form. Furthermore, even though the matrix will be sparse, the elements cannot be arranged in such a way to confine the elements to a narrow region [10]. Although the computation time will depend on the speed of the computer, in general the technique may be too time consuming when dealing with problems that require high resolution and a large number of propagation steps. The alternate direction method was developed to address this difficulty [9].

V. ALTERNATE DIRECTION IMPLICIT METHOD

The alternate direction implicit method is a modification of the Crank–Nicolson method that uses smaller tridiagonal matrices. The ADI method can be derived directly from the

$$\frac{u_{m,l}^{n+1} - u_{m,l}^n}{\Delta z} = \left(\frac{1}{2jk_o}\right) \left(\frac{u_{m+1,l}^{n+1} - 2u_{m,l}^{n+1} + u_{m-1,l}^{n+1}}{2\Delta x^2} + \frac{u_{m+1,l}^n - 2u_{m,l}^n + u_{m-1,l}^n}{2\Delta x^2}\right)$$
$$+ \left(\frac{1}{2jk_o}\right) \left(\frac{u_{m,l+1}^{n+1} - 2u_{m,l}^{n+1} + u_{m,l-1}^{n+1}}{2\Delta y^2} + \frac{u_{m,l+1}^n - 2u_{m,l}^n + u_{m,l-1}^n}{2\Delta y^2}\right) \qquad (16)$$
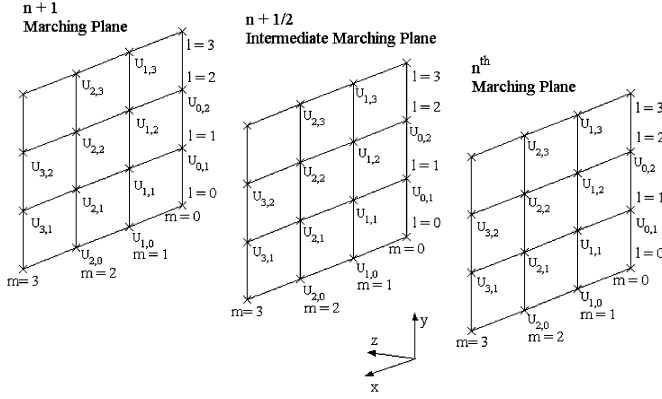
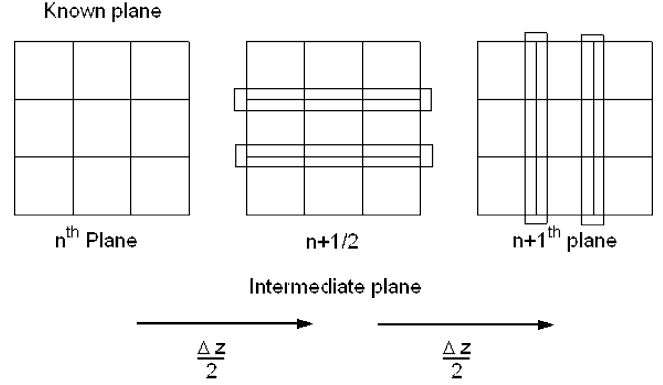Fig. 2.   The marching planes of the three-dimensional Crank–Nicolson method.

Fig. 3.   The line by line decomposition of the planes using the ADI method.

Crank–Nicolson method by adding $\left(r_x r_y/(4jk_o)^2\right)\delta_x\delta_y$ to (17)

$$
\left(1 - \frac{r_x}{4jk_o}\delta_x - \frac{r_y}{4jk_o}\delta_y + \frac{r_x r_y}{(4jk_o)^2}\delta_x\delta_y\right) u^{n+1}
$$
$$
= \left(1 + \frac{r_x}{4jk_o}\delta_x + \frac{r_y}{4jk_o}\delta_y + \frac{r_x r_y}{(4jk_o)^2}\delta_x\delta_y\right) u^n
$$
$$
+ \frac{r_x r_y}{(4jk_o)^2}\delta_x\delta_y \left(u^{n+1} - u^n\right)
$$
$$
+ O(\Delta z^3) + O(\Delta z \Delta x^2) + O(\Delta z \Delta y^2)
$$
$$
+ \boxed{O(\Delta z^3) \leftarrow \text{new   error   term}} \tag{20}
$$

where $O(*)$ represents the order of error. The error introduced by the new error term is $O(\Delta z^3)$ and can be ignored because it is of the same order as the truncation error. Equation (20) above can be re-written in factor form

$$
\left(1 - \frac{r_x}{4jk_o}\delta_x\right)\left(1 - \frac{r_y}{4jk_o}\delta_y\right) u^{n+1}
$$
$$
= \left(1 + \frac{r_x}{4jk_o}\delta_x\right)\left(1 + \frac{r_y}{4jk_o}\delta_y\right) u^n. \tag{21}
$$

We can split (21) in a way that allows us to solve for the unknown field line by line (direction by direction)

$$
\left(1 - \frac{r_x}{4jk_o}\delta_x\right)\tilde{u}^{n+1/2} = \left(1 + \frac{r_y}{4jk_o}\delta_y\right) u^n \tag{22}
$$
$$
\left(1 - \frac{r_y}{4jk_o}\delta_y\right) u^{n+1} = \left(1 + \frac{r_x}{4jk_o}\delta_x\right) \tilde{u}^{n+1/2}. \tag{23}
$$

Combined, (22) and (23) are known as the Peaceman–Rachford method [8], [9], [17] and is equivalent to (21) (easily verified by multiplying both sides by $(1 - (r_x/4jk_o)\delta_x)$). Fig. 3 shows schematics of the line by line decomposition of the planes within one propagation step. For this example, the unknowns of the intermediate plane can be solved using one N_x matrix and the unknowns of the $n+1$ plane can be solved using one N_y matrix.

One difficulty with the ADI technique, is that it has special conditions for boundary values in the $n+1/2$ plane. The n and the $n+1$ planes are physical planes and the intermediate $n+1/2$ plane may be considered a virtual plane which may not have the same boundary conditions as the physical plane. Adding (22) and (23), we arrive at an expression for the intermediate plane in terms of the physical planes

$$
\tilde{u}^{n+1/2} = \frac{1}{2}\left(1 - \frac{r_y}{4jk_o}\delta_y\right) u^{n+1} + \frac{1}{2}\left(1 + \frac{r_y}{4jk_o}\delta_y\right) u^n \tag{24}
$$
$$
u = \beta(x,y,z) = \text{boundary.} \tag{25}
$$

Equation (24) can only be satisfied if the boundary values are known for each propagation step. If we impose the same boundary conditions on the intermediate plane as the physical plane, then $\tilde{u}_{m,l}^{n+1/2} = \beta_{m,l}^{n+1/2} = \beta_{m,l}^n = \beta_{m,l}^{n+1}$, and the overall accuracy will be *first order* [9]. As with the Crank–Nicolson method, the ADI method is also unconditionally stable [9], [10], [17], [29].

Tunnels with rectangular cross sections are the simplest for ADI to handle because one matrix can be used to solve for the field along the x axis and one matrix for the field along the y axis. However, for a circular case, there will need to be (N_y-2) matrices to solve for the field along the x axis and $(N_x - 2)$ matrices to solve for the field along the y axis. The Taylor series approximation is used to approximate the curved boundary [10] and different ADI matrices must be used for each line. The size of the matrices will depend on the number of mesh points along a line of the circle.

Another complication arises when enforcing Neumann-type boundary conditions. Using the technique outlined in Morton [10], we can derive a first order normal derivative using interpolation in order to express boundary mesh points in terms of interior mesh points. As a result, the Neumann boundary condition may couple two lines in one dimension and increase our number of unknowns. This makes the order in which the line by line decomposition occurs important. For a circle, the line by line decomposition must begin at the center line where the boundary values are reflected inward and there is no coupling. This makes the complete solution of the center line possible without the introduction of new unknowns. The lines directly adjacent to the center line must be solved next and so on until the field along the plane is solved completely. In order to avoid increasing the number of unknowns and the size of the ADI matrices, the lines must be solved in successive order.

TABLE I
THE NORMALIZED RMS ERROR FOR THE RECTANGULAR, CIRCULAR AND SEMI-CIRCULAR
CYLINDRICAL WAVEGUIDES WITH DIRICHLET AND NEUMANN BOUNDARY CONDITIONS

Erms Error (%)		Rectangular WG		Circular WG		Semi-Circular WG	
$\Delta x, \Delta y$	Δz	Dirichlet	Neumann	Dirichlet	Neumann	Dirichlet	Neumann
0.8λ	$5\,\lambda$	11.9	10.3	11.4	25.2	12.1	56.4
0.8λ	$10\,\lambda$	13.7	12.2	13.2	24.2	14	55.1
0.8λ	$20\,\lambda$	19.5	18	18.7	21.9	19.7	51
0.4λ	$5\,\lambda$	4.9	4.7	5.0	12.9	5.2	29.1
0.4λ	$10\,\lambda$	7.3	7.1	7.0	11.9	7.6	27.5
0.4λ	$20\,\lambda$	14.4	14.2	13.8	12	14.6	24.3

VI. PEC WAVEGUIDE EXAMPLES USING THE ADI METHOD

In this section, the analytical solutions of simple PEC waveguides are used to measure the accuracy of the ADI approach. Our analysis will consider three test cases: the *(a)* square, *(b)* circular and *(c)* semi-circular cylindrical PEC waveguides.

All simulations are done using a unit strength Gaussian with 3.5λ standard deviation placed at the center of the transverse plane as the initial field and operating at a frequency of 3 GHz. The magnetic and electric scalar potentials are simulated by enforcing either the Dirichlet or Neumann boundary conditions. In test case *(a)*, the waveguide cross-section is $40\lambda \times 40\lambda$ and in test cases *(b)* and *(c)* the radius is 20λ. All test cases are simulated up to a distance of 100 m.

Under these parameters, only modes propagating within $\pm 15°$ make significant contributions and, therefore, the PE approximation is valid. Furthermore, because of the PE limitation, Nyquist's theorem restricts the descretizations, Δx and Δy, to be less than 1.9λ. This is shown by considering the transverse wavelength at $15°$ [7].

Table I displays the rms error

$$E_{\mathrm{rms}} = \frac{\sqrt{\frac{1}{N}\sum_m \sum_l \left| u_{m,l}^{\mathrm{FDM}} - u_{m,l}^{\mathrm{anal}} \right|^2}}{\sqrt{\frac{1}{N}\sum_m \sum_l \left| u_{m,l}^{\mathrm{anal}} \right|^2}} \qquad (26)$$

where $u_{m,l}^{\mathrm{FDM}}$ is the approximated discretized field, $u_{m,l}^{\mathrm{anal}}$ is the known analytical field and N is the total number of unknowns. The analytical solutions used in Sections VI-A–C are obtained in the traditional ways outlined by Harrington [1] and other texts.

A. Test Case (a): Rectangular Waveguide With Dirichlet and Neumann Boundary Conditions

Fig. 4(a)–(b) show the analytical and numerical solutions for the rectangular waveguide with Dirichlet boundary conditions. Fig. 4(c)–(d) show the analytical and numerical solutions for the rectangular waveguide with Neumann boundary conditions. It is clear from these figures that there is very good agreement between the analytical and simulated field patterns. Table I shows that for transverse descretizations, $\Delta x = \Delta y = 0.4\lambda$, and marching step size, $\Delta z = 5\lambda$, the rms error is within 5%.
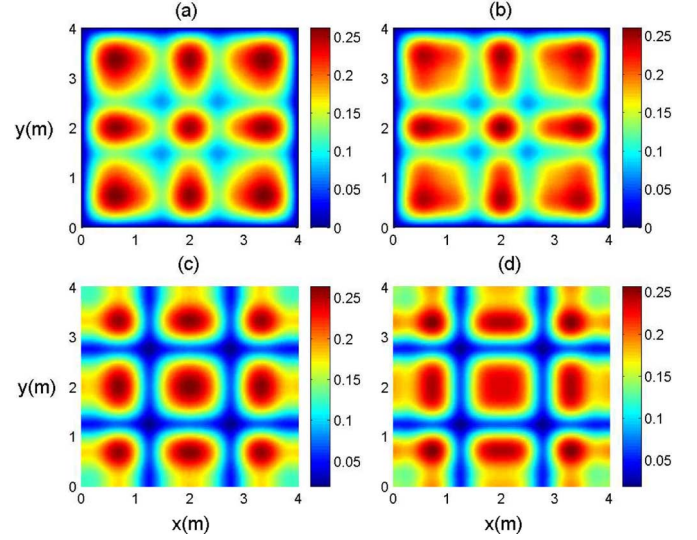

Fig. 4. The (a) analytical solution and (b) numerical approximation of the rectangular waveguide with Dirichlet boundary conditions (RMS error = 7.3%) and the (c) analytical solution and (d) numerical approximation of the rectangular waveguide with first order Neumann boundary conditions (RMS error = 7.1%).

B. Test Case (b): Circular Cylindrical Waveguide With Dirichlet and Neumann Boundary Conditions

Fig. 5(a)–(b) show the analytical and numerical solutions for the circular waveguide with Dirichlet boundary conditions. Again, there is good agreement between the analytical and numerical field patterns. Table I shows that for transverse descretizations, $\Delta x = \Delta y = 0.4\lambda$, and marching step size, $\Delta z = 5\lambda$, the rms error is within 5%. Fig. 5(c)–(d) show the analytical and numerical solutions for the circular waveguide with Neumann boundary conditions, using first order interior interpolation. There is good agreement between the analytical and numerical field patterns but the rms error increases to 12.9%. The rms error for the Neumann case is greater than the Dirichlet case because both the boundary conditions and the interpolations are first order.

C. Test Case (c): Semi-Circular Cylindrical Waveguide With Dirichlet and Neumann Boundary Conditions

Fig. 6(a)–(b) show the analytical and numerical solutions for the semi-circular waveguide with Dirichlet boundary conditions. As with the previous test cases, there is very good agreement between the analytical and simulated field patterns. Table I shows that for transverse descretizations,
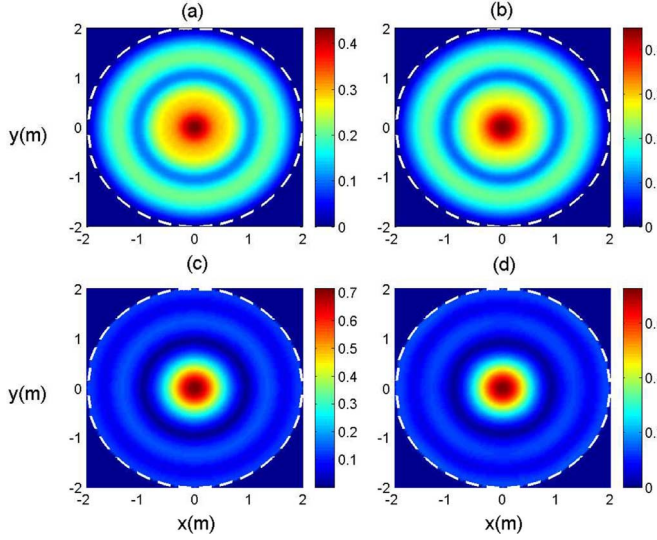
Fig. 5. The (a) analytical solution and (b) numerical approximation of the circular waveguide with Dirichlet boundary conditions (RMS error $= 7.0\%$) and the (c) analytical solution and (d) numerical approximation of the circular waveguide with Neumann boundary conditions (RMS error $= 11.90\%$).
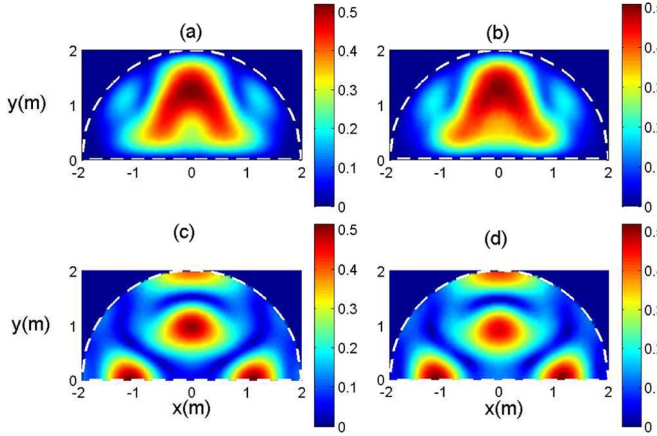

Fig. 6. The (a) analytical solution and (b) numerical approximation of the semicircular waveguide with Dirichlet boundary conditions (RMS error $= 7.6\%$) and the (c) analytical solution and (d) numerical approximation of the semicircular waveguide with Neumann boundary conditions (RMS error $= 27.5\%$).

$\Delta x = \Delta y = 0.4\lambda$, and marching step size, $\Delta z = 5\lambda$, the rms error is about 5.2%.

Fig. 6(c)–(d) show the analytical and numerical solutions for the semi-circular waveguide with Neumann boundary conditions. There is very good agreement between the field patterns in both cases. However, Table I shows for $\Delta x = \Delta y = 0.4\lambda$ and $\Delta z = 5\lambda$, the rms error is very large (29%). Fig. 7 shows the analytical (solid-line) and simulated (dashed-line) fields at $\phi = \pi/2$. As shown in the figure, the error is concentrated near $y = 0$ and the field pattern is preserved. Like in the circular Neumann case, the rms error can be improved by decreasing the mesh descretizations. Also, we can see from Table I the error grows slightly as the step size is decreased with fixed mesh descretizations. This is because the field is converging towards a field not exactly matching the analytical solution.
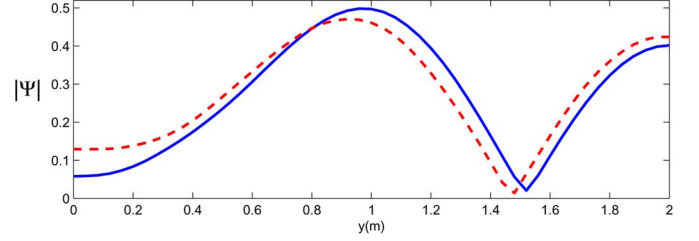
Fig. 7. The magnitude of the analytical (blue, solid) and simulated (red, dashed) field at $x = 0$ for PEC tunnel with semi-circular cross-section and Neumann boundary conditions.

Although the ADI method can produce larger errors than the CN method, for the examples considered, the fields generated by both codes are nearly identical. Keeping the descretizations the same, the error between the two methods is less than 1%. A discussion on the accuracy of the ADI method can be found in [30].

VII. IMPEDANCE WAVEGUIDE EXAMPLES USING THE ADI METHOD

Tunnels with impedance walls can be very difficult to solve and, aside from some special cases, closed form solutions may not exist [6], [14]. In Sections VII-A and B, we will consider lossy tunnels with known analytical solutions. We will consider two such cases, the rectangular tunnel with small surface impedance and the circular tunnel with a linear dipole located at its center.

A. Rectangular Tunnel

Exact analytical solutions for the fields in rectangular tunnels with lossy walls do not exist [6], [14]. In [6], a lossy tunnel is treated as an imperfect metal waveguide with the relative surface impedance of a good conductor

$$Z = Z_s = R_s + jX_s = \frac{1}{\sqrt{-j\sigma_r}}. \qquad (27)$$

If the magnitude of the relative surface impedance is much less than unity, then perturbation techniques can be used to derive approximate fields [6]. Unlike the perfect waveguide case, pure TE and TM modes will not always propagate within the imperfect waveguide. Instead, there will exist hybrid $(E_xH)_{m,n}$ and $(EH_x)_{m,n}$ modes that are coupled TE and TM modes. The $(E_xH)_{m,n}$ mode is a TE mode with a small TM component, and the $(EH_x)_{m,n}$ mode is a TM mode with a small TE component.

In the case of the rectangular tunnel, the impedance matrix $\bar{\bar{T}}_o\bar{\bar{G}}\bar{\bar{T}}_o$, shown in (15), becomes diagonal because the normal vectors, n_x and n_y, disappear alternatively on the tunnel wall. Therefore, the transverse reduced field components $U(x,y,z)$ and $V(x,y,z)$ in the orthogonal (x,y) plane are decoupled and can be solved independently [4]. The hybrid fields that are solved numerically will depend on the boundary conditions enforced on the waveguide walls.
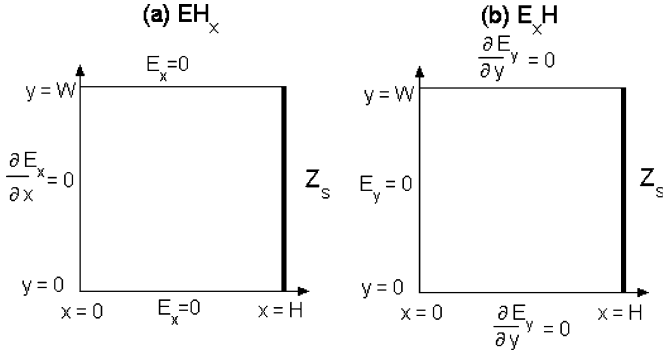
Fig. 8. Rectangular waveguide profiles displaying the boundary conditions for the E_x field of the EH_x mode and the E_y field of the E_xH mode in the transverse plane.

Fig. 9. The magnitudes of the analytical and numerical fields of the (a–c) EH_{x11} and (d–f) E_xH_{11} mode.

Consider the simple example of a rectangular waveguide $0 \leq x \leq H$, $0 \leq y \leq W$, with three PEC walls and one impedance wall located at $x = H$, where the normal vectors are $n_x = 1$ and $n_y = 0$. Fig. 8 shows the boundary conditions at the three PEC walls for the EH_x [Fig. 8(a)] and the E_xH [Fig. 8(b)] hybrid modes with the E_x and E_y fields given by [6, Eq. (36)].

Let us consider the case of the EH_{x11} mode propagating in the waveguide at a frequency of 1 GHz with a wall of impedance, $Z_s = 0.01 + j0.01$. Good conductors have large conductivity, and for this case the equivalent conductivity is 556 S/m. Fig. 9(a) shows the magnitude of the analytical solution of E_x in the origin plane of $z = 0$ and Fig. 9(b) shows the magnitude of the analytical solution of E_x at the distance of $z = 1$ km. Fig. 9(c) shows the magnitude of the simulated E_x, using the analytical field in the origin plane as the initial field. The discretizations along the transverse plane are $\Delta x = \Delta y = 0.27\lambda$, and along the propagation axis, $\Delta z = 11\lambda$. We can see that there is strong agreement between the analytical field and the simulated field in the transverse plane. The field pattern doesn't depend on distance because a single mode was used as the initial field. The ADI simulation produced the same pattern throughout the step by step simulation. For this case, this difference between the mode attenuation factors (MAFs) of the analytical and numerical solution is 2.36 dB/km.

Now, let us consider the case of the E_xH_{11} mode propagating in the waveguide at a frequency of 1 GHz with a wall of impedance, $Z_s = 0.3 + j0.3$. For this case the equivalent conductivity is 0.62 S/m. Fig. 9(d) shows the magnitude of the analytical solution of E_y in the origin plane of $z = 0$. Fig. 9(e) shows the magnitude of the analytical solution of E_y at the axial distance of $z = 5$ km. The distance of 5 km was chosen so that there would be noticeable attenuation along the axial direction. Fig. 9(f) shows the magnitude of the simulated E_y field, using the analytical field in the origin plane as the initial field. The discretizations along the transverse plane are the same as in the EH_{x11} example, $\Delta x = \Delta y = 0.27\lambda$ and $\Delta z = 11\lambda$. Again, as in the EH_{x11} example, we can see that there is strong agreement between the analytical and the simulated field patterns in the transverse plane. Also, the magnitudes of the analytical and simulated fields show that the simulated field captures the attenuation of the field along the z direction.
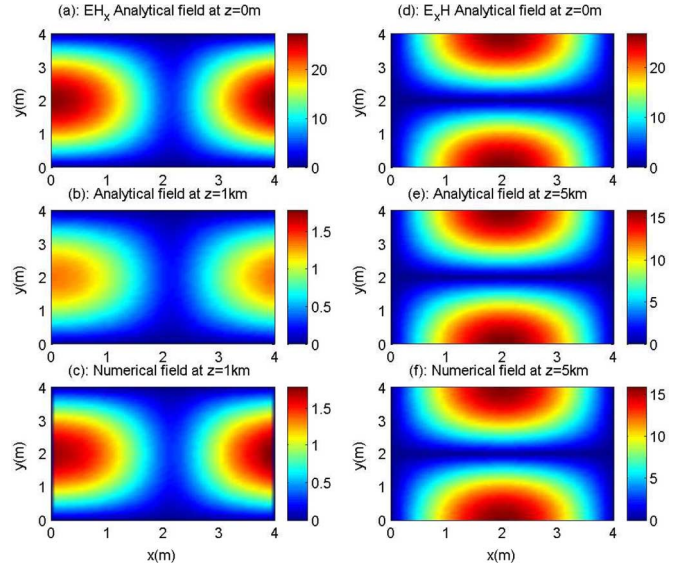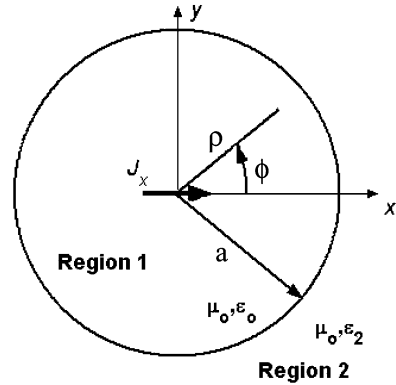

Fig. 10. Cross-section of a circular tunnel with lossy walls and a linear source located at the center.

The main advantage of the ADI method over the Crank–Nicolson method is the use of smaller ADI matrices. In the rectangular case, E_x and E_y fields are decoupled and each field can be treated as a scalar PE problem. As with the previous scalar PE problems, if there are N_x and N_y mesh points along the x and y dimensions, respectively, the Crank–Nicolson matrix will be a sparse matrix of rank $(N_xN_y - 4)$. However, the ADI method will only require 2 matrices of rank N_x and N_y, respectively.

B. Circular Tunnel

Next, we use the ADI-PE to solve for the field in a lossy tunnel with a circular cross-section of radius a (shown in Fig. 10). The tunnel is treated as a hole in a lossy dielectric medium where the interior is free space and the exterior is characterized by (μ_0, ϵ_2), with $\epsilon_2 = \epsilon_0 (\epsilon_r - j\sigma_r)$. Fig. 10 also shows the linear dipole current source with dipole moment P (in amp-meters), $J_x = P\delta(\phi)\delta(z)\delta(\rho)/\rho$, located at the center of the tunnel $(\rho = 0, \phi = 0)$ in the $z = 0$ plane. The derivation of the electric fields produced by this source is well known and the details are given in [14] and [15].
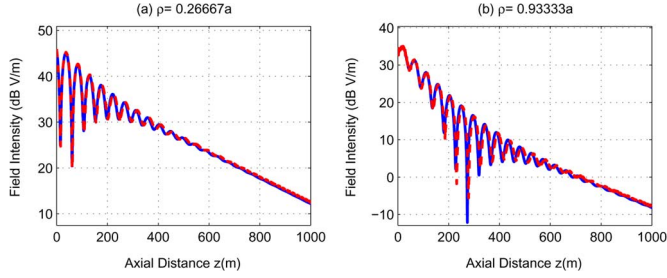
Fig. 11. (a)–(b) Axial distribution of the analytical (blue, solid) and simulated (red, dashed) E_x field intensity for the $HE_{1,1-2}$ modes; $a = 2$ m, $f = 1$ GHz, $P/a = 1$ amp, $\epsilon_r = 12$, $\sigma_o = 0.02$ S/m.

As with the imperfect rectangular waveguide, the lossy circular tunnel will produce hybrid modes. For the special case of the centered linear source, the only possible hybrid modes are EH_{1m} and HE_{1m} [14], [15]. The transverse electric field components are shown in [15, Eq. (95) and (96)].

For our ADI simulations, we consider a smooth, straight tunnel of radius 2 m and 1 km in length. We choose our electrical parameters to match the parameters studied in the published work of Dudley and Mahmoud [15]. We choose $\epsilon_r = 12$ and $\sigma_o = 0.02$ S/m and P/a = 1 amp. In this case, HE_{11} is the dominant mode and attenuates least over the axial distance of the guide. The MAF of the HE_{11} mode is 2.77 dB/100 m [14]. In a lossy tunnel, higher order modes will attenuate more than the dominant mode and, for large axial distances, the field intensity will correspond to the intensity of the HE_{11} mode.

Fig. 11(a)–(b) shows the analytical field intensity (in dB) as a function of axial distance at $\phi = \pi/2$ for about (a) $\rho = 0.25a$ and (b) $\rho = 0.9a$ (in blue). The first two modes ($HE_{1,1-2}$) are plotted because the angles of propagation, with respect to the z axis, are below the parabolic approximation limit of $\pm 15°$. The angles of the modes are calculated using

$$\cos\theta = \frac{Re(k_z)}{k_o}. \tag{28}$$

The complex k_z terms are calculated using the procedure outlined in [15, (Eq. 76)]. The ordering of the first three modes, according to angle, is $HE_{11}(3.3°)$, $HE_{12}(7.3°)$ and $HE_{13}(11.8°)$. We can see from Fig. 11 that the field intensity can be divided into a near-zone and a far-zone [14]. The near-zone is characterized by rapid variations due to higher mode interactions. The far-zone is smoother and more linear because the higher order modes disappear due to attenuation. In the far-zone the slope corresponds to the MAF of the HE_{11} mode. For our analysis we define the E_{rms} as a function of axial distance

$$E_{rms} = 20\log_{10}\left[\frac{\left|E_{x,anal} - Ue^{-jk_o z}\right|}{\left|E_{x,anal}\right|}\right]. \tag{29}$$

The analytical solution for the $HE_{1,1}$ and $HE_{1,2}$ modes at the $z = 0$ plane is used as the initial field for the ADI simulation and the discretizations along the transverse plane and the
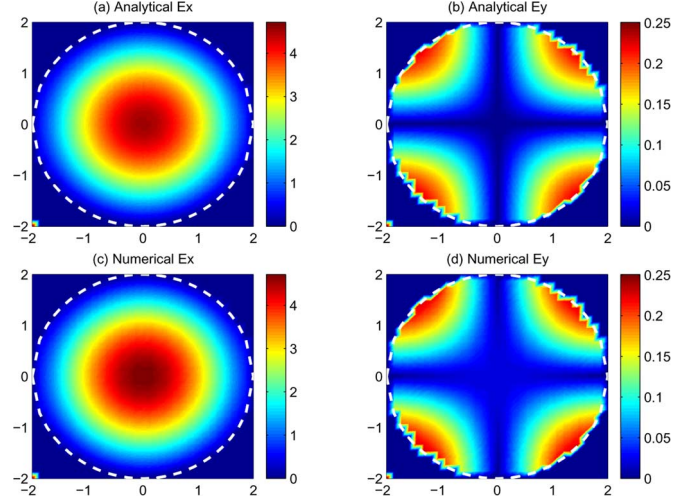

Fig. 12. (a)–(b) Analytical transverse E_x and E_y field distribution at a distance of 1 km for the $HE_{1,1-2}$ modes, respectively. (c)–(d) Numerical transverse E_x and E_y field distribution with $\Delta x = 0.444\lambda$, $\Delta y = 0.444\lambda$, $\Delta z = 1.6667\lambda$.

axial direction are $\Delta x = \Delta y = 0.444\lambda$ and $\Delta z = 1.667\lambda$. As shown in Fig. 11, the analytical and simulated results are in very good agreement. In the far-zone ($z > 600$ m), where the field becomes more linear the E_{rms} doesn't exceed -10 dB. As we can see from Fig. 11, the trend and shape of the analytical result is captured in the simulation. Fig. 12 compares the magnitudes of the E_x and E_y field distribution in the transverse plane. We can see that the magnitudes and field patterns are in close agreement between the analytical [Fig. 12(a)–(b)] and numerical [Fig. 12(c)–(d)] results.

Unlike the rectangular case, the impedance matrix $\bar{\bar{T}}_o\bar{\bar{G}}_o\bar{\bar{T}}_o$ (15), is not diagonal and the E_x and E_y fields have to be solved simultaneously. As a result, we have to solve a true vector PE and the size of both the Crank–Nicolson and ADI matrices increase. If there are N_x and N_y mesh points along the x and y dimensions, respectively, the Crank–Nicolson matrix will be a sparse matrix of rank $2 \times (N_x N_y - 4)$, double the size of the scalar PE case. The ADI method will require $N_y - 2$ matrices that are at most size $2 \times N_x$ and $N_x - 2$ matrices that are at most size $2 \times N_y$. When dealing with large problems, the memory required to perform calculations with the Crank–Nicolson matrix, even with use of the sparse command in MATLAB, might become too computationally intensive for an average PC.

VIII. COMPARING ADI SIMULATIONS WITH EXPERIMENTAL DATA

Finally, we consider the case of real tunnels and compare ADI simulations to measurements shown in published results. Our first example is the Massif Central tunnel in south-central France studied in the published work of Dudley, Lienard, Mahmoud, and Degauque [14]. The tunnel is straight and 3.5 km in length with smooth walls composed of large blocks of stone or concrete. The roughness is estimated to be in the order of a centimeter. The transverse dimensions of the tunnel are given in Fig. 13. The experiment performed by Dudley et al. consisted of a transmitting and receiving antenna placed vertically at a height of 2 m and horizontally at one-quarter the width of the
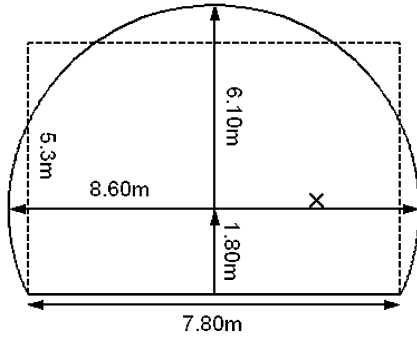
Fig. 13. The profile of the Massif Central tunnel.

Fig. 14. The electric-field intensity in dBm and the corresponding least square fit line of the (a) Massif Central tunnel (blue, solid), (b) the ADI solution using the equivalent rectangular profile with $\epsilon_r = 5$ and $\sigma_o = 0.01$ S/m (red, dashed), (c) the ADI solution using the arched profile with $\epsilon_r = 5$ and $\sigma_o = 0.01$ S/m (green, circle) and (d) the ADI solution using the arched profile with $\epsilon_r = 12$ and $\sigma_o = 0.01$ S/m (black, asterisk) as a function of axial distance and operating frequency of 450 MHz.

Fig. 15. The electric-field intensity in dBm and the corresponding least square fit line of the (a) Massif Central tunnel (blue, solid), (b) the ADI solution using the equivalent rectangular profile with $\epsilon_r = 5$ and $\sigma_o = 0.01$ S/m (red, dashed), and (c) the ADI solution using the arched profile with $\epsilon_r = 5$ and $\sigma_o = 0.01$ S/m (green, circle) as a function of axial distance and operating frequency of 900 MHz.

tunnel ($z = 2.15$ m), shown as an "X" in Fig. 13. The transmitting power was 34 dBm and the frequencies of 450 MHz and 900 MHz are studied. Half-wave vertical dipoles are used for 450 MHz, and vertically polarized wide-band horn antennas (with a gain of 7 dBi) are used for 900 MHz.

The research team of Dudley *et al.* [14] uses an equivalent rectangular tunnel (see Fig. 13) in order to characterize the Massif Central tunnel. The dimensions of the rectangular tunnel are shown in Fig. 13 and the electrical parameters are chosen to be $\epsilon_r = 5$ and $\sigma_o = 0.01$ S/m. The theoretical attenuation constant of the dominant mode of the equivalent rectangular tunnel is given by [13] and [14]

$$\alpha_{11} = \frac{2}{H}\left(\frac{\lambda}{2H}\right)^2 Re\left[\frac{1}{\sqrt{\epsilon_{rc} - 1}}\right]$$
$$+ \frac{2}{W}\left(\frac{\lambda}{2W}\right)^2 Re\left[\frac{\epsilon_{rc}}{\sqrt{\epsilon_{rc} - 1}}\right] \quad (30)$$

where H is the horizontal length and W is the vertical length, given by $H = 7.8$ m and $W = 5.3$ m. The attenuation of the dominate mode in the equivalent rectangular tunnel corresponds to the attenuation of the measured field in the Massif Central tunnel. Figs. 14 and 15 show the field intensity in dBm as a function of axial distance (in blue) as measured by the research team of Dudley *et al.* [14]. The MAF of the equivalent rectangular tunnel and the experimental data are shown in the first two rows of Table II.

The ADI simulations are done using the actual arched cross-section of the Massif Central tunnel and the equivalent rectangular tunnel (Fig. 13). The electrical parameters are chosen to match the parameters of the research team. At this point, it is important to discuss possible sources of error in the simulation of real tunnels. One possible error may be the incorrect prediction of electrical parameters of the tunnel walls. If a real tunnel is made up of dry cement and stone, the parameters will depend on the materials used to mix the cement and its percentage of water content. One source estimates the parameters of dry concrete to vary from $\epsilon_r = 4 - 10$ and $\sigma_o = 0.001 - 0.01$ S/m and for wet concrete, $\epsilon_r = 10 - 20$ and $\sigma_o = 0.01 - 0.1$ S/m [16]. In addition, the electrical parameters will also change with frequency. For the equivalent rectangle, this isn't a problem because the parameters have been fixed in [14].

The initial field used in the simulations may not represent the actual antenna field used in measurements. However, even with an incorrect initial field, the field in the far zone, where lower
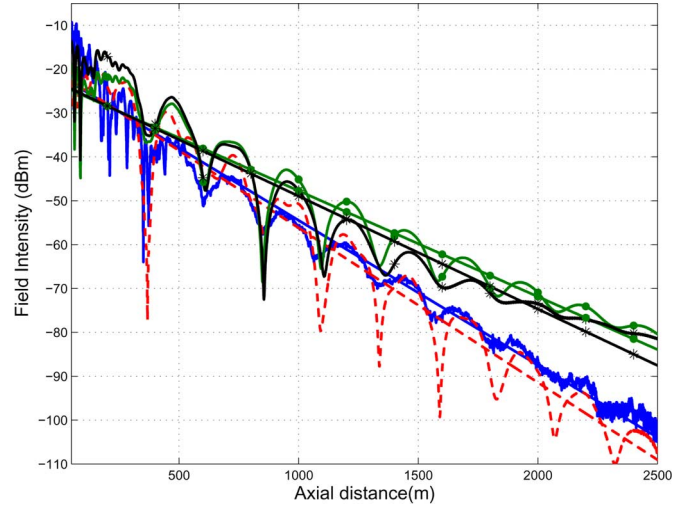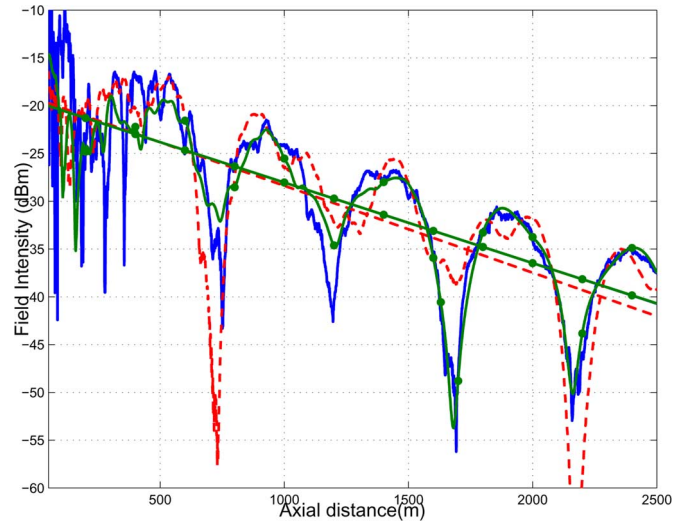
order modes dominate, the correct attenuation will be obtained. This allows us some flexibility when setting up our simulations. So long as the lower order modes are illuminated, different initial fields will yield the same MAFs in the far zone. This discrepancy is accounted for by offsetting the vertical axis of the simulation data so the least square fitted lines intersect at the far zone point. Instead of having the dipole inside the tunnel entrance, as in the Massif Central experiment, we set up the dipole 30 m away from the tunnel opening. This allows us to use the far field expressions for the dipole and avoid solving more complicated field patterns. We do not know the value of the field along the boundary wall in the initial plane. If we use the free

TABLE II
THE EXPERIMENTAL, THEORETICAL AND SIMULATED MODE ATTENUATION
FACTORS FOR THE MASSIF CENTRAL TUNNEL

Frequency (MHz) / Far zone range	450 (.25-2.5km)	900(0.5-2.5km)
$\text{MAF}_{data}(dB/km)$	33.0	8.5
$\text{MAF}_{equiv.rectangle}(dB/km)$	35.1	8.6
$\text{MAF}_{ADIArch}(dB/km)$	24	8.45
$\text{MAF}_{ADIrectangle}(dB/km)$	35.3	9.1

space values along the boundary, the error will be in the form of high oscillations in the MAFs in the far zone. We can eliminate these oscillations by filtering off the field at the boundary with a unit gaussian with $\sigma = 0.75$ m (450 MHz) and $\sigma = 1.5$ m (900 MHz). We don't expect an exact match between the simulated results and the measured results in the near zone where the parabolic approximation is not satisfied. However, we expect, in the far-zone, the E-field and the field attenuation to be correctly modeled by the simulation. Figs. 14–15 show the simulated field intensity in dBm of the tunnel with an arched cross section (in green, circle) and the equivalent rectangle (in red, dashed). The MAFs of the simulations are computed from the slope of the least square fit line using data in the far zone. The MAFs of the simulations and the far zone ranges are shown in Table II.

In Fig. 14, for the 450 MHz case, we can see that there is good agreement between the simulated rectangular tunnel and the measured data. Table II shows the discrepancies of the MAFs of the measured data, the equivalent rectangle and the simulated rectangle are about 2 dB/km. The discrepancy of the simulated results for the arched shape tunnel and the measured data is about 11 dB/km. This is believed to be the result of using an incorrect electrical parameter. Increasing the magnitude of the electrical parameters for the arched shape will increase the attenuation of the tunnel. This is shown in Fig. 14, where the black curve is the simulation for $\epsilon_r = 12$ and $\sigma_o = 0.01$ S/m. In Fig. 15, for the 900 MHz case, we see that there is more agreement among all the simulations. As Table II shows, the discrepancies among all the simulations are within 1 dB/km. The good agreement may be due to the frequency dependant nature of the electrical parameters. At 900 MHz, the electrical parameters used for the equivalent rectangle may be in better agreement with the actual electrical parameters of the tunnel wall.

Our second example is a railway tunnel in Japan studied in the published work of Chiba, Inaba, Kuwamoto, Banno, and Sato [12]. The tunnel is straight and 1.47 km in length and also made up of concrete. The cross-section of the tunnel is arched shaped and has two 3.9 m lanes separated by a notch. Fig. 16 shows the dimensions of the tunnel cross-section. The measurement team used half-wave dipole antennas for the transmitters and receivers and the antennas were placed at a height of 3.6 m above the ground and 30 m from the tunnel opening with a transmitting
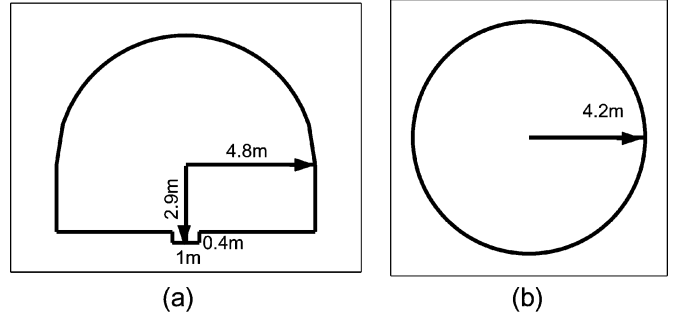

Fig. 16. The profiles of the (a) Japanese National Railway tunnel and (b) the equivalent circular tunnel.
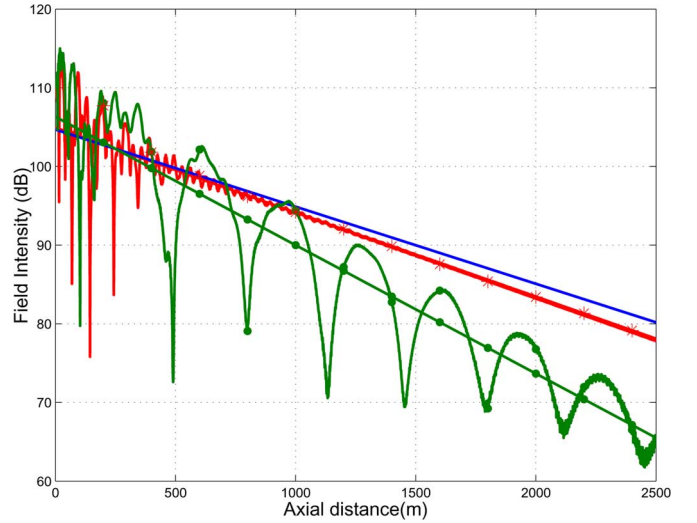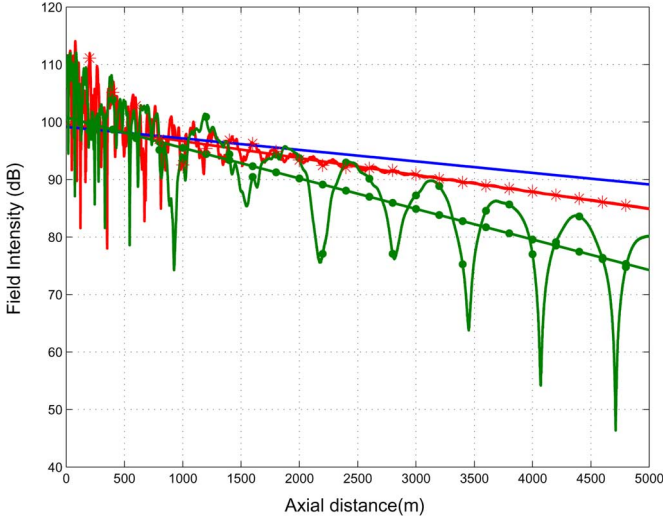

Fig. 17. The (a) MAF of the Japanese National Railway tunnel (blue, solid), (b) the electric-field intensity and least square fit line of the ADI solution using the equivalent circular profile (red, asterisk) and (c) the electric-field intensity and least square fit line of the ADI solution using the arched profile (green, circle) as a function of axial distance with an operating frequency of 470 MHz.

power of 1 W. The measurement team characterized the tunnel with an equivalent area circular cylindrical waveguide of radius 4.2 m. The electrical parameters of the equivalent circular cylindrical tunnel were chosen so that the attenuation of the dominant mode will correspond to the attenuation of the measured field. The theoretical attenuation constant is given by (31), shown at the bottom of the page, where u_{nm} is the root of the $(n-1)$th Bessel function. The MAF of the equivalent circular cylindrical tunnel is defined, $\epsilon_r = 5.5$ and $\sigma_o = 0.03$ S/m. Figs. 17 and 18 show the theoretical MAF of the dominant mode of the equivalent circular cylindrical tunnel (blue).

The ADI simulations are done using the arched shape cross section (Fig. 16) and the equivalent circular cross section. As

$$\alpha_{n1} = \left(\frac{u_{n1}}{2\pi}\right)^2 \frac{\lambda^2}{a^3} \left(\begin{array}{ll} \text{Re}\left[\frac{1}{\sqrt{\epsilon_{rc}^2-1}}\right] & \text{for } TE_{00} \\ \text{Re}\left[\left(\frac{1}{2}\right)\left(\epsilon_{rc}^2+1\right)\sqrt{\epsilon_{rc}^2-1}\right] & \text{for } EH_{01} \end{array} \right) \tag{31}$$

Fig. 18. The (a) MAF of the Japanese National Railway tunnel (blue, solid), (b) the electric-field intensity and least square fit line of the ADI solution using the equivalent circular profile (red, asterisk) and (c) the electric-field intensity and least square fit line of the ADI solution using the arched profile (green, circle) as a function of axial distance with an operating frequency of 900 MHz.

TABLE III
THE EXPERIMENTAL, THEORETICAL AND SIMULATED MODE
ATTENUATION FACTORS FOR THE RAILWAY TUNNEL

Frequency (MHz)	470 (.25-2.5km)	900(0.5-5km)
$\text{MAF}_{data}(dB/km)$	9.8	2.0
$\text{MAF}_{ADI equivalent circle}(dB/km)$	10.8	2.95
$\text{MAF}_{ADIArch}(dB/km)$	16.32	5.3

before, the electrical parameters are chosen to match the parameters of the research team. Figs. 17 and 18 show the simulated field intensity of the tunnel with an arched cross-section (in green, circle) and the equivalent circle (in red, asterisk). The field intensity is shown in dB such that $1 \ \mu V/m = 0$ dB.

In Fig. 17, for the 470 MHz case, we can see that there is reasonable agreement between the attenuation of the simulated equivalent circular cylindrical tunnel and the theoretical attenuation. As with the previous tunnel, the simulation is least accurate in this frequency range. As we increase the frequency there is greater agreement between the theoretical MAF and the simulated fields. As before, we can see from the figures that in the 470 MHz and 900 MHz cases, the two mode interactions are present in the far zone [14]. Table III summarizes the theoretical MAF, the simulated equivalent circular cylindrical tunnel and the tunnel with an arched cross section MAFs. The discrepancy between the theoretical MAF and the equivalent circular cylindrical tunnel is about 1 dB/km and lower for both frequencies. The discrepancy between the theoretical MAF and the tunnel with arched cross section about 6.5 dB/km for 470 MHz and 3.3 dB/km for 900 MHz.

A. Usage of CPU Time and Memory

In this section, we briefly examine the computation time and memory usage of the Crank–Nicolson and ADI method. Table IV shows a side by side comparison of the execution time and CPU memory of the Crank–Nicolson and ADI method

TABLE IV
THE CPU MEMORY AND COMPUTATIONAL TIME FOR $N_x = 70$ AND
2000 MARCHING STEPS FOR THE TUNNEL WITH RECTANGULAR
PROFILE AND DIRICHLET BOUNDARY CONDITIONS

Rectangle Dirichlet	ADI	CN
Execution Time (sec)	124 (2min)	3532 (1hr)
Memory	3.3KB (208 elements)	378.6KB (23662 elements)

for the case of a PEC tunnel with a rectangular profile with resolution $N_x = N_y = 70$ and using 2000 marching steps. The execution time refers to the time it take MATLAB to perform the one Backslash command and multiplied by the number of loops. This accounts for any variation in codes by only recording the time it takes to invert the matrices. For the Crank–Nicolson method, the Backslash command was performed after the memory saving Sparse command was used. As we can see from Table IV, ADI runs mush faster and takes significantly less memory than the Crank–Nicolson method.

To continue the comparison between the Crank–Nicolson method and the ADI, we will breifly address the issue of stability. Following the discussion in [29], on the stability of the ADI, solving for a step/wavenumber independent bound on the amplification matrix becomes difficult because the ADI-PE matrices contain off-diagonal terms that make finding eigenvalues difficult. For the PEC waveguide, numerical tests have shown that the ADI amplification matrix is normal and bounded by unity and the von Neumann condition is sufficient. When the impedance boundary condition is applied, the matrices are no longer normal, but the amplification matrix is still bounded by unity for various discretizations and steps. For examples considered in the paper, we have not encountered instability when applying the IBC to the ADI-PE. The CN is unconditionally stable and less sensitive to boundary conditions. However, for modest discretizations, we were able to get very good agreement between the CN and ADI solutions, which would imply that the ADI is also stable with the IBC.

IX. CONCLUSION

We have presented the ADI method for use in solving the parabolic equation for radiowave propagtion in tunnels. We have shown that because the ADI technique uses smaller matrices than the widely used Crank–Nicolson method, it reduces the computational labor of an average PC.

Using analytical models, we have shown that the ADI method, in combination with the parabolic approximation, can simulate the attenuation and field patterns in tunnels whose electrical parameters are known. Our simulation results also verify the use of the grazing angle impedance approximation on the tunnel walls.

In the case of actual tunnels, our ADI-PE approach compares well with published experimental data for the 900 MHz frequency in the far zone for the Massif Central tunnel. The tunnel's far zone is the region where rapid oscillations cease and the lowest order modes dominate. The descrepancies in measured and simulated results may be attributed to lack of knowledge of the tunnel's electrical parameters. Simulated ADI-PE results for equivalent tunnel profiles, where electrical parameters are defined, show high accuracy.

Future work will use the ADI-PE to study the cases of curved and branching tunnels with rough surfaces as well as making comparisons to experimental data.

ACKNOWLEDGMENT

REFERENCES

[1] R. F. Harrington, *Time-Harmonic Electromagnetic Fields*. New York: Wily-Interscience, 2001.

[2] M. Levy, *Parabolic Equation Methods for Electromagnetic Wave Propagation*. London, U.K.: Inst. Elect. Eng., 2000.

[3] A. V. Popov, V. A. Vinogradov, N. Y. Zhu, and F. M. Landstorfer, "3D parabolic equation model of EM wave propagation in tunnels," *Electron. Lett.*, vol. 35, pp. 880–882, May 1999.

[4] A. V. Popov and N. Y. Zhu, "Modeling radio wave propagation in tunnels with a vectorial parabolic equation," *IEEE Trans. Antennas Propag.*, vol. 48, pp. 1403–1412, Sep. 2000.

[5] N. Noori, S. Safavi-Naeini, and H. Oraizi, "A new three-dimensional vector parabolic equation approach for modeling radio wave propagation in tunnels," in *Proc. IEEE Antennas Propag. Society Int. Symp.*, 2005, vol. 4B, pp. 314–317.

[6] A. E. Karbowiak, "Theory of imperfect waveguides: The effect of wall impedance," *Proc. Inst. Elect. Eng.*, vol. 102, pp. 698–708, 1955.

[7] C. A. Zelly and C. C. Constantinou, "A three-dimensional parabolic equation applied to VHF/UHF propagation over irregular terrain," *IEEE Trans. Antennas Propag.*, vol. 47, pp. 1586–1596, Oct. 1999.

[8] D. W. Peaceman and H. H. Rachford, Jr. "The numerical solution of parabolic and elliptic differential equations," *J. Soc. Indust. Appl. Math.*, pp. 28–41, Mar. 1955.

[9] J. C. Strikwerda, *Finite Difference Schemes and Partial Differential Equations*, 2nd ed. Philadelphia, PA: SIAM, 2004.

[10] K. W. Morton and D. F. Mayers, *Numerical Solution of Partial Differential Equations*. New York: Columbia Univ. Press, 1994.

[11] G. D. Smith, *Numerical Solution of Partial Differential Equations: Finite Difference Methods*, 3rd ed. New York: Oxford Univ. Press, 1985.

[12] J. Chiba and T. Inaba, "Radio communication in tunnels," *IEEE Trans. Microw. Theory Tech.*, vol. MTT-26, pp. 439–443, 1978.

[13] A. G. Emslie, R. L. Lagace, and P. F. Strong, "Theory of the propagation of UHF radio waves in coal mine tunnels," *IEEE Trans. Antennas Propag.*, vol. AP-23, pp. 192–205, 1975.

[14] D. G. Dudley, M. Lienard, S. F. Mahmoud, and P. Degauque, "Wireless propagation in tunnels," *IEEE Antennas Propag. Mag.*, vol. 49, no. 2, pp. 11–26, 2007.

[15] D. G. Dudley and S. F. Mahmoud, "Linear source in a circular tunnel," *IEEE Trans. Antennas Propag.*, vol. 54, pp. 2034–2047, Jul. 2006.

[16] J. Arai, T. Mizobuchi, and K. Suda, "Study on measurement of chloride content using electromagnetic wave in reinforced concrete structures," presented at the Int. Symp. (NDT-CE), 2003.

[17] A. R. Mitchell and D. F. Griffiths, *The Finite Difference Method in Partial Differential Equations*. New York: Wiley, 1980.

[18] R. Janaswamy, *Radiowave Propagation and Smart Antennas for Wireless Communications*. New York: Springer, 2000.

[19] G. Fairweather and A. R. Mitchell, "A new computational procedure for ADI methods," *SIAM J. Numer. Anal.*, vol. 4, no. 2, pp. 163–170, 1967.

[20] S. Mckee, D. P. Wall, and S. K. Wilson, "An alternating direction implicit scheme for parabolic equations with mixed derivative and convective terms," *J. Computat. Phys.*, vol. 126, no. 0120, pp. 64–76, 1996.

[21] R. K. Mohantay and M. K. Jain, "High accuracy difference schemes for the systems of two space nonlinear parabolic differential equations with mixed derivatives and variable coefficients," *J. Computat. Appl. Math.*, vol. 70, no. 1, pp. 15–32, 1996.

[22] J. Douglas, Jr and H. H. Rachford, Jr. "On the numerical solution of heat conduction problems in two and three space variables," *Trans. Amer. Mathem. Society*, vol. 82, no. 2, pp. 421–439, 1956.

[23] T. Namiki, "A new FDTD algorithm based on alternating direction implicit method," *IEEE Trans. Microw. Theory Tech.*, vol. 47, pp. 2003–2007, 1999.

[24] C. Ma, Z. Chen, and A. Zhao, "Development of an unconditionally stable full-wave 2D ADI-FDTD method for analysis of arbitrary wave guiding structures," in *IEEE MTT-S Digest*, 2002, vol. 3, pp. 2049–2052.

[25] X. T. Dong, N. V. Venkatarayalu, B. Guo, W. Y. Yin, and Y. B. Gan, "General formulation of unconditionally stable ADI-FDTD method in linear dispersive media," *IEEE Trans. Microw. Theory Tech.*, vol. 52, no. 1, pp. 170–174, 2004.

[26] A. V. Popov, "Radio pulse propagation in a smoothly bent oversized waveguide," in *Proc. Day on Diffraction Int. Seminar*, 2003, pp. 175–182.

[27] T. B. A. Senior, "Impedance boundary conditions for imperfectly conducting surfaces," *Appl. Sci. Res.*, vol. B, pp. 418–436, 1960.

[28] A. V. Popov, "Parabolic equation method for electromagnetic guiding structures," in *Proc. 2001 3rd Int. Conf. Transparent Opt. Netw.*, pp. 42–46.

[29] S. Ogurtsov, G. Pan, and R. Diaz, "Examination, clarification, and simplification of stability and dispersion analysis for ADI-FDTD and CNSS-FDTD schemes," *IEEE Trans. Antennas Propag.*, vol. 55, pp. 3595–3602, 2007.

[30] S. G. Garcia, T.-W. Lee, and S. C. Hagness, "On the accuracy of the ADI-FDTD method," *IEEE Trans. Antennas Propag.*, vol. 1, pp. 31–34, 2002.

Richard Martelly ████████████████ ████████████. He received the B.E. degree in engineering physics from Stevens Institute of Technology, Hoboken, NJ, in 2000 and the M.S. degree in electrical engineering from the Polytechnic University, Brooklyn, in 2004. He is currently working toward the Ph.D. degree at the University of Massachusetts, Amherst.

In Fall 2004, he joined the Antenna and Propagation Laboratory, Department of Electrical and Computer Engineering, University of Massachusetts.

Ramakrishna Janaswamy (F'03) received the Ph.D. degree in electrical engineering from the University of Massachusetts, Amherst, in 1986.

From August 1986 to May 1987, he was an Assistant Professor of electrical engineering at Wilkes University, Wilkes Barre, PA. From August 1987 to August 2001, he was on the faculty of the Department of Electrical and Computer Engineering, Naval Postgraduate School, Monterey, CA. In September 2001, he joined the Department of Electrical and Computer Engineering, University of Massachusetts, Amherst, where he is a currently a Professor. He is the author of the book *Radiowave Propagation and Smart Antennas for Wireless Communications*, (Kluwer Academic Publishers, November 2000) and a contributing author in *Handbook of Antennas in Wireless Communications* (CRC Press, August 2001) and *Encyclopedia of RF and Microwave Engineering* (Wiley, 2005). His research interests include deterministic and stochastic radio wave propagation modeling, analytical and computational electromagnetics, antenna theory and design, and wireless communications.

Prof. Janaswamy is a Fellow of IEEE. He is an elected member of U.S. National Committee of International Union of Radio Science, Commissions B and F. He was the recipient of the R. W. P. King Prize Paper Award of the IEEE Transactions on Antennas and Propagation in 1995. For his services to the IEEE Monterey Bay Subsection, he received the IEEE 3rd Millennium Medal from the Santa Clara Valley Section in 2000. He served as an Associate Editor of *Radio Science* from January 1999 to January 2004 and as an Associate Editor of the IEEE TRANSACTIONS ON VEHICULAR TECHNOLOGY.

Transitional probabilities for the four-state random walk on a lattice in the presence of partially reflecting boundaries

R. Janaswamy[a]

*Department of Electrical and Computer Engineering, University of Massachusetts, 100
Natural Resources Road, 215-D Marcus Hall, Amherst, Massachusetts 01003, USA*

The four-state random walk (4RW) model, wherein the particle is endowed with two states of spin and two states of directional motion in each space coordinate, permits a stochastic solution of the Schrödinger equation (or the equivalent parabolic equation) without resorting to the usual analytical continuation in complex space of the particle trajectories. Analytical expressions are derived here for the various transitional probabilities in a 4RW by employing generating functions and eigenfunction expansions when the particle moves on a $1+1$ space-time lattice with two-point boundary conditions. The most general case of dissimilar boundaries with partially reflecting boundary conditions is treated in this paper. The transitional probabilities are all expressed in terms of a finite summation involving trigonometric functions and/or Chebyshev polynomials of the second kind that are characteristics of diffusion and Schrödinger equations, respectively, in the 4RW model. Results for the special case of perfectly absorbing boundaries are compared to numerical values obtained by directly counting paths in the random walk simulations. © *2009 American Institute of Physics.* [DOI: 10.1063/1.3122768]

I. INTRODUCTION

The four-state random walk (4RW) model, wherein a particle undergoing random walk is endowed with two states of direction (in a one-dimensional case) and two states of spin or parity, was considered by Ord and Deakin[1] to arrive at a macroscopic model for the Schrödinger equation and physically interpret its wavelike solutions. It was shown in that paper that both the traditional diffusion equation as well as the Schrödinger equation were embedded in the same physical model. The usual diffusion process is contained in the overall sum of all particle paths irrespective of their direction and parity, while the wavelike behavior of the Schrödinger equation is contained in the differences in densities of the right-going particles or left-going particles with opposite parity. The 4RW model owes its existence to the Feynman chessboard model as elaborated in Ref. 2 and is also useful in solving practical electromagnetic, acoustic, and optical boundary value problems for the complex field amplitude when a stochastic approach is used to treat the governing *parabolic equation*. (In the applied sciences area, the parabolic equation is sometimes referred to as the parabolic wave equation.) The standard parabolic equation used in such time-harmonic problems contains partial derivatives with respect to the spatial coordinates only, where the spatial coordinate along the axial direction takes the place of the time variable in the time-dependent Schrödinger equation. Furthermore, the potential function present in the Schrödinger equation is replaced by the medium refractive-index term in the parabolic equation. The parabolic equation is obtained when the Helmholtz equation describing the true field is subject to a one-way propagation with a subsequent application of the paraxial approximation.[3,4] Normally one needs to resort to analytical continuation of boundary data, as is done in Ref. 5, when the parabolic equation is

---

[a]Electronic mail: janaswamy@ecs.umass.edu.

50, 053301-1

solved numerically using a stochastic approach. The resulting random walks will then traverse a complex-valued space, which, in turn, calls for analytical continuation of boundary data and the spatial geometry.[6] However, the 4RW model permits a solution to these problems without such analytical continuations.

In a previous paper,[7] the author developed expressions for the various transitional probabilities for the 4RW on a discrete lattice for spatially unbounded case. In addition to detailing a method for arriving at the transitional probabilities, the results presented therein could also be useful in determining other stochastic quantities of interest such as the first passage time probabilities, expected number of visits to a given site, and maximum excursions of a random walk on a line for various linear combinations of these probabilities. In developing numerical schemes for solving boundary value problems with complex geometries, it is desirable to have analytical solutions for simpler geometries to facilitate validation against benchmark problems.[8] The traditional way to discretize the Schrödinger equation or the diffusion equation for numerical treatment by the finite difference method is to employ a central difference formula in the spatial coordinates. An example of this is the implicit Crank–Nicolson scheme, which, for the diffusion equation, can be identified with the traditional two-state random walk, where the particle is endowed with two directions of motion only. Analytical results for the traditional two-state random walk with perfectly absorbing and/or reflecting boundaries have been treated in number of works including Refs. 9 and 10. Separately, the case of the telegraph equation with partially reflecting boundaries is studied in Ref. 11. No such analytical results are yet available for the 4RW model and it is the purpose of the present paper to provide analytical results for a benchmark initial-boundary-value problem in 1 +1 space-time dimension for the model. To this end, we extend the results in Ref. 7 by considering two-point boundary conditions for the 4RW model and derive analytical expressions for various transitional probabilities. Setting aside the fact that the 4RW model has a physical basis in the Feynman chessboard model and that various transitional probabilities are related to the solution of the continuous Schrödinger equation, it is not at all obvious at the outset from the governing difference equations that an analytical solution is possible for the said boundary value problem, particularly for the wavelike solutions. The transform approach utilized in this paper will reveal the presence of the discrete Laplacian operator that is embedded in these equations and will clearly demonstrate why such a solution is still possible, while paving the way for eigenfunction expansion. This will be elaborated in Secs. II and III. The most general case of partially absorbing and dissimilar boundaries is considered in this paper. Results for the special cases of perfectly absorbing and perfectly reflecting boundaries are also provided in the paper. The results presented here correspond to the solution of the discrete form of the diffusion equation as well as to the real and imaginary parts of the discrete Schrödinger equation.

In Sec. II, the 4RW model is briefly reviewed, and the problem under investigation is defined. In Sec. III, the solution to the 4RW model subject to the general boundary conditions is developed using the concept of generating functions and eigenfunction expansion. Expressions are provided for the special cases of perfectly reflecting and perfectly absorbing boundaries and the results for the latter are compared to numerical simulations obtained by directly counting paths. Finally, conclusions and topics of further research are given in Sec. IV. It may be noted parenthetically that it is not our purpose here to evaluate other various models that have been put forward to physically interpret the Schrödinger equation, a topic that is immensely interesting in its own right.

II. 4RW MODEL

For a particle moving on a discrete lattice and subject to random collisions, the transitional probabilities considered in Ref. 7 at the discrete space-time point $(x=m\Delta, t=s\epsilon)$ are of the form

$$E_t \begin{pmatrix} w_1 \\ w_2 \end{pmatrix} = \frac{1}{2} \begin{pmatrix} (E_x + E_x^{-1}) & -(E_x - E_x^{-1}) \\ 0 & 0 \end{pmatrix} \begin{pmatrix} w_1 \\ w_2 \end{pmatrix}, \tag{1}$$

$$E_t \begin{pmatrix} q_1 \\ q_2 \end{pmatrix} = \frac{1}{\sqrt{2}} \begin{pmatrix} E_x^{-1} & -E_x \\ E_x^{-1} & E_x \end{pmatrix} \begin{pmatrix} q_1 \\ q_2 \end{pmatrix},$$

(2)

where $q_1(m\Delta, s\epsilon) = 2^{s/2}[p_1(m\Delta, s\epsilon) - p_3(m\Delta, s\epsilon)]$, $q_2(m\Delta, s\epsilon) = 2^{s/2}[p_2(m\Delta, s\epsilon) - p_4(m\Delta, s\epsilon)]$, $w_1(m\Delta, s\epsilon) = [p_1(m\Delta, s\epsilon) + p_2(m\Delta, s\epsilon) + p_3(m\Delta, s\epsilon) + p_4(m\Delta, s\epsilon)]$, $w_2(m\Delta, s\epsilon) = [p_1(m\Delta, s\epsilon) + p_3(m\Delta, s\epsilon)] - [p_2(m\Delta, s\epsilon) + p_4(m\Delta, s\epsilon)]$, and $p_\mu(m\Delta, s\epsilon)\Delta$, $\mu = 1, \ldots, 4$, is the probability that a particle is in state μ at the space-time point $(m\Delta, s\epsilon)$, $m = 0, \pm 1, \pm 2, \ldots$, $s = 0, 1, \ldots$. The particle changes its direction of motion with every collision, but changes its parity or spin at every other collision. The combination of two directions of motion and two states of spin constitute the four states in the model. It has been shown in Refs. 1 and 12 that such a four-state random walk simultaneously encompasses the diffusion as well as Schrödinger equations. The quantities w_1 and w_2 pertain to the diffusion process, while q_2 and q_1 correspond to the real and imaginary parts of the Schrödinger wave function in the discrete case. We will refer to (1) as the diffusion equation and to (2) as the Schrödinger equation even though they are really the respective discrete counterparts of the traditional diffusion and Schrödinger equations. The operators E_x and E_t are, respectively, the spatial and temporal advancing operators and are defined mathematically as $E_x^{\pm 1} p_\mu(m\Delta, s\epsilon) = p_\mu[(m \pm 1)\Delta, s\epsilon]$ and $E_t p_\mu(m\Delta, s\epsilon) = p_\mu[m\Delta, (s+1)\epsilon]$. It is assumed in Eqs. (1) and (2) that the probability that a particle maintains its direction at the next time step remains the same as the probability that it will change its direction at the next time step and that the probability of remaining at the same location at the next time step is zero. If the number of right-going particles is the same as those going to the left at time $t = 0$, then $w_2 \equiv 0$ and Eq. (1) reduces to the simpler equation

$$E_t w_1 = D_x w_1,$$

(3)

where $D_x = (E_x + E_x^{-1})/2$ is the discrete averaging operator. The averaging operator in (3) owes its existence to the presence of the Laplacian operator in the continuous diffusion equation $\partial w_1/\partial t = D_1 \partial^2 w_1/\partial x^2$ when the spatial and temporal step sizes are subject to the condition $\Delta = \sqrt{2\epsilon D_1}$. As such, most of the well-posed issues that pertain to the continuous case[13] will be carried over to the discrete case. In particular, Eq. (3) will be well posed with two-point Robin type of boundary conditions and the solution will exist.

The difference equations (1) and (2) are assumed to be valid in the region $0 < m < \ell$ and $s > 0$ and they are supplemented by an initial condition at $s = 0$ and boundary conditions at $m = 0, \ell$. We will adopt the abbreviation $v(m, s)$ to denote the discrete function $v(m\Delta, s\epsilon)$. The boundary conditions we are interested in are of the form

$$p_j(0, s) - \alpha_1 p_j(1, s) = 0 \quad \text{and} \quad p_j(\ell, s) - \alpha_2 p_j(\ell - 1, s) = 0, \quad j = 1, \ldots, 4,$$

(4)

where the constants α_1 and α_2 are assumed to be real and positive. These are the discrete versions of the general Robin type of boundary conditions for the continuous case. The case of purely absorbing boundaries at $m = 0, \ell$ is characterized by $\alpha_i = 0$, $i = 1, 2$, while the purely reflecting case is characterized by $\alpha_i = 1$, $i = 1, 2$.[9,14] The general case corresponds to partially absorbing and partially reflecting boundaries with different degrees of absorption at the two ends. Our interest is to obtain analytical solutions to (1) and (2) on a discrete space-time lattice $(m\Delta, s\epsilon)$ subject to the boundary conditions in (4). In contrast to the diffusion equation (3), it is not clear at the outset whether a solution will exist for (2) under the boundary condition (4), setting aside the fact that it is tied to the Schrödinger equation. This is because of the presence of the spatial shift operators that are neither symmetric (as in the operator D_x) nor asymmetric (as in an operator of the form $V_x = [E_x - E_x^{-1}]$). Recall, for instance, that the diffusion equation with a drift term, whose discrete counterpart will have neither a symmetric nor an asymmetric spatial operator, will not always have a solution even with Neumann type of boundary conditions. However, we will demonstrate in Sec. III that the temporally transformed equation corresponding to (2) will indeed contain the averaging operator and the existence question will be set to rest. Because of the linearity of Eqs. (1) and (2),

a convenient solution can be obtained by using generating function and integral transform techniques as outlined in Refs. 7 and 15.

III. SOLUTION BY GENERATING FUNCTIONS

In the following, we assume complete symmetry between the right-moving and left-moving particles so that $w_2 \equiv 0$. Consider a function $v(m\Delta, s\epsilon)$ and its temporal transform $\hat{v}(m\Delta, z)$ as defined in Ref. 7,

$$\hat{v}(m\Delta, z) = \sum_{s=0}^{\infty} v(m\Delta, s\epsilon)z^s \equiv \mathcal{T}v. \tag{5}$$

The quantity $\hat{v}(m\Delta, z)$ may be thought of as the discrete version of the Laplace transform of v and is simply referred to as the z-transform. The inverse relation is defined as

$$v(m\Delta, s\epsilon) = \frac{1}{2\pi i} \oint_{C_z} \frac{\hat{v}(m\Delta, z)}{z^{s+1}} dz \equiv \mathcal{T}^{-1}\hat{v}, \tag{6}$$

where C_z is a closed contour around the origin in the complex z-plane that encloses only the singularities at the origin, $i = \sqrt{-1}$, and the symbol $\mathcal{T}$ denotes the temporal transform. The transformed variable $\hat{v}(m\Delta, z)$ is also referred to as the *generating function* within the random walk community.[9] Applying the temporal transform to (2) and (3) and making use of the shift property of the $\mathcal{T}$ transform ($\mathcal{T}[E_t v_1] = z^{-1}[\hat{v}_1(m\Delta, z) - v_1(m,0)]$) and carrying out some simplifications, we arrive at the following equations for various generating functions in terms of the initial conditions:

$$[1 - zD_x]\hat{w}_1(m\Delta, z) = w_1(m,0), \tag{7}$$

$$[1 - \sqrt{2}zD_x + z^2]\hat{q}_1(m\Delta, z) = q_1(m,0) - \frac{z}{\sqrt{2}}E_x[q_2(m,0) + q_1(m,0)], \tag{8}$$

$$[1 - \sqrt{2}zD_x + z^2]\hat{q}_2(m\Delta, z) = q_2(m,0) - \frac{z}{\sqrt{2}}E_x^{-1}[q_2(m,0) - q_1(m,0)]. \tag{9}$$

The characteristic operators that appear on the left hand sides of (7)–(9) are generic to the diffusion and the Schrödinger equations under the 4RW model and are seen to be completely independent of the boundary conditions. A remarkable feature of the spatial dependence of these operators, which is not entirely evident in the initial Eq. (2) describing the transitional probabilities, is that they all involve only the averaging operator D_x that is the discrete counterpart of the Laplacian operator in the continuous case. Such a relation has already been alluded to in Sec. II. Both the diffusion and the Schrödinger equations contain the Laplacian operator as far as the spatial variables are concerned, and the transformation from the continuous case to the discrete case for a given order of accuracy is not unique. Employing a central difference formula for the spatial operator will lead to Crank–Nicolson type of discrete equations,[8] which, like the 4RW model, result in a spatially second order accurate schemes. The important point to note from (9) is that the unknown variable contains only the averaging operator D_x and that any other asymmetries that arise from E_x or E_x^{-1} alone are contained only on the right hand side, operating on the known initial conditions. A formal solution to Eqs. (7)–(9) can be affected by using the inverse relation (6) and evaluating the integrals in the complex z-plane after expanding the reciprocal of the characteristic operators in a Maclaurin series. [Recall that the contour integral in the inverse operator in (6) is a closed loop of vanishing size around the origin]. The procedure is similar to that outlined in Ref. 7 and will involve Chebyshev polynomials of the second kind for the wave functions q_1 and q_2. The result is

$$w_1(m,s) = D_x^s w_1(m,0), \tag{10}$$

$$q_1(m,s) = U_s\left(\frac{D_x}{\sqrt{2}}\right) q_1(m,0) - \frac{1}{\sqrt{2}} U_{s-1}\left(\frac{D_x}{\sqrt{2}}\right) E_x[q_2(m,0) + q_1(m,0)], \tag{11}$$

$$q_2(m,s) = U_s\left(\frac{D_x}{\sqrt{2}}\right) q_2(m,0) - \frac{1}{\sqrt{2}} U_{s-1}\left(\frac{D_x}{\sqrt{2}}\right) E_x^{-1}[q_2(m,0) - q_1(m,0)], \tag{12}$$

where $U_s(x)$ is Chebyshev polynomial of the second kind of order s and argument x. The formal solution given in (10)–(12) are general enough and are valid for all appropriate boundary conditions. The presence of the operator D_x^s in the diffusion variable $w_1(m,s)$ is not surprising at all. Indeed, in free space, (10) directly generates the *characteristic function* $\cos^s \theta$ of the probability w_1 when $w_1(m,0)$ is expanded in a Fourier series with transform variable θ. By the same token, the appearance of the polynomials $U_s(\cdot)$ and $U_{s-1}(\cdot)$ is intrinsic to the Schrödinger equation in the 4RW model, as already indicated previously. Note that the operators D_x (or any power of it) and E_x commute and the order of these terms on the right hand sides of (11) and (12) is not important. To complete the solution, we must now expand the unknown functions in terms of eigenfunctions of the D_x operator that are consistent with the boundary conditions at $m = 0, \ell$. In free space, the appropriate eigenfunctions are plane waves with a continuous wavenumber as adopted in Ref. 7 (or said in other words, the unknown function is represented in terms of its Fourier transform or series).

For the boundary conditions indicated as in (4), we seek an expansion of a spatial function $v(m)$ in terms of exponential and/or trigonometric functions. An exponential function of the form $v_0(m) = r^m$ is a valid eigenfunction provided that the base $r = \alpha_1^{-1} = \alpha_2$. Clearly this is only possible in the special case of $\sqrt{\alpha_1 \alpha_2} := \alpha_g = 1$, where α_g denotes the geometric mean of α_1 and α_2. In such a case, $D_x v_0(m) = 0.5(\alpha_1 + \alpha_2) v_0(m) := \alpha_a \cdot v_0(m)$, where α_a, being the arithmetic mean of α_1 and α_2, is the eigenvalue pertaining to $v_0(m)$. When $\alpha_g \neq 1$, such an exponential function will not exist. We will denote the presence of this exponential function by employing the Kronecker symbol $\delta_{\alpha_g}^1$. A harmonic function of the form

$$u_j(m) = A_j \sin(k_j m) + B_j \cos(k_j m), \quad j = 1, 2, \ldots \tag{13}$$

is also a valid eigenfunction provided that

$$B_j(1 - \alpha_1 \cos k_j) = A_j \alpha_1 \sin k_j \tag{14}$$

with the spatial frequency k_j given by

$$\sin(k_j \ell) - 2\alpha_a \sin[k_j(\ell - 1)] + \alpha_g^2 \sin[k_j(\ell - 2)] = 0. \tag{15}$$

Equations (14) and (15) are obtained by enforcing the boundary condition (4) at the two ends. A trivial solution of Eq. (15) is $k_j = 0$. There will be a total of $(\ell - 1)$ nontrivial solutions of (15), thus constituting a total of ℓ distinct eigenfunctions [including the function $v_0(m)$] to represent the solution of (9) and (12) at the points $m = 0, \ldots, \ell$. Making use of (14) in (13) allows us to extract a bare eigenfunction $v_j(m)$ (i.e., without the coefficient A_j and other common factors) in the form

$$v_j(m) = \sin(k_j m) - \alpha_1 \sin[k_j(m - 1)], \tag{16}$$

with the spatial frequency set by (15) for a given α_1, α_2, and ℓ. It can be easily verified that $D_x v_j(m) = \cos k_j \cdot v_j(m)$ so that the eigenvalue of $v_j(m)$ with respect to the averaging operator is $\cos k_j$. Furthermore, the eigenfunctions $v_j(m)$ with distinct k_j as well as $v_j(m)$ and $v_0(m)$ are mutually orthogonal, i.e.,

$$\sum_{m=1}^{\ell-1} v_i(m) v_j(m) = 0, \quad i,j = 1, \dots, \ell-1, \quad i \neq j, \tag{17}$$

$$\sum_{m=1}^{\ell-1} v_j(m) v_0(m) = 0, \quad j = 1, \dots, \ell-1. \tag{18}$$

The following normalization results can also be readily established for the functions $v_0(m)$ and $v_j(m)$:

$$\sum_{m=1}^{\ell-1} v_0^2(m) = \frac{\alpha_1^{-2(\ell-1)} - 1}{1 - \alpha_1^2} := 1/a_0 \tag{19}$$

and

$$\sum_{m=1}^{\ell-1} v_j^2(m) = \frac{\sin(k_j \ell)}{\sin k_j} \left[\alpha_1 \cos[k_j(\ell-2)] - \frac{1}{2}(1 + \alpha_1^2)\cos[k_j(\ell-1)] \right] + \frac{\ell(1 + \alpha_1^2)}{2} - \alpha_1 \ell \cos k_j$$
$$- \alpha_1^2 \sin^2[k_j(\ell-1)] := 1/a_j. \tag{20}$$

Gathering all of the above results, an arbitrary function $v(m)$ satisfying the boundary condition (4) will admit a spectral representation of the form

$$v(m) = A_0 v_0(m) \delta_{\alpha_g}^1 + \sum_{j=1}^{\ell-1} A_j v_j(m), \tag{21}$$

where the coefficients A_0 and A_j of the basis functions $v_0(m)$ and $v_j(m)$ can be obtained in terms of the function $v(m)$ via the orthogonality conditions and normalization relations (17)–(20),

$$A_0 = a_0 \sum_{m=1}^{\ell-1} v_0(m) v(m), \tag{22}$$

$$A_j = a_j \sum_{m=1}^{\ell-1} v_j(m) v(m), \quad j = 1, \dots, \ell-1. \tag{23}$$

With this spectral representation, it is clear that

$$D_x v(m) = A_0 \alpha_a \cdot v_0(m) \delta_{\alpha_g}^1 + \sum_{j=1}^{\ell-1} A_j \cos k_j \cdot v_j(m). \tag{24}$$

Hence, the presence of D_x in the spatial domain is accounted for by multiplying the spectral basis function term by its respective eigenvalue. In particular,

$$D_x^s v(m) = A_0 \alpha_a^s \cdot v_0(m) \delta_{\alpha_g}^1 + \sum_{j=1}^{\ell-1} A_j \cos^s k_j \cdot v_j(m) \tag{25}$$

and

$$U_s\left(\frac{D_x}{\sqrt{2}}\right) v(m) = A_0 U_s\left(\frac{\alpha_a}{\sqrt{2}}\right) \cdot v_0(m) \delta_{\alpha_g}^1 + \sum_{j=1}^{\ell-1} A_j U_s\left(\frac{\cos k_j}{\sqrt{2}}\right) \cdot v_j(m). \tag{26}$$

Having laid out the formulation for the general case, we will now consider two interesting special cases which will merit a separate discussion.

A. Totally absorbing boundaries

In this case $\alpha_1 = \alpha_2 = 0$, which precludes the exponential solution $v_0(m)$. Equation (15) implies a solution $k_j = \pi j / \ell$, $j = 1, \ldots, \ell - 1$. The eigenfunctions $v_j(m)$ will be reduced to $\sin(\pi j m / \ell)$ and $a_j = 2/\ell$ from (20). In this case, one gets the discrete sine transform[16] representation for a function satisfying Dirichlet boundary conditions,

$$v(m) = \sum_{j=1}^{\ell-1} A_j \sin\left(\frac{j\pi m}{\ell}\right), \quad A_j = \frac{2}{\ell} \sum_{m=1}^{\ell-1} v(m)\sin\left(\frac{j\pi m}{\ell}\right), \quad j = 1, \ldots, \ell - 1. \tag{27}$$

B. Totally reflecting boundaries

For totally reflecting boundaries at both ends, $\alpha_1 = \alpha_2 = 1$, which dictate that $\alpha_g = \alpha_a = 1$. Equation (15) indicates a solution $k_j = j\pi/(\ell - 1)$, $j = 1, \ldots, \ell - 1$. The exponential function now reduces to a constant function $v_0(m) = 1$. The normalization constants a_0 and a_j are obtained from (19) and (20) as

$$1/a_0 = (\ell - 1), \quad 1/a_j = 2(\ell - 1)\sin^2\left(\frac{\pi j}{2(\ell - 1)}\right). \tag{28}$$

An unknown function $v(m)$ satisfying perfectly reflecting conditions at the two ends can then be expressed as

$$v(m) = A_0 + \sum_{j=1}^{\ell-1} A_j \left[\sin\left(\frac{\pi j m}{\ell - 1}\right) - \sin\left(\frac{\pi j (m-1)}{\ell - 1}\right)\right] = A_0 + \sum_{j=1}^{\ell-1} 2A_j \sin\left(\frac{\pi j}{2(\ell - 1)}\right)\cos\left(\frac{\pi j\left(m - \frac{1}{2}\right)}{\ell - 1}\right)$$

$$:= A_0 + \sum_{j=1}^{\ell-1} C_j \cos\left(\frac{\pi j\left(m - \frac{1}{2}\right)}{\ell - 1}\right) \tag{29}$$

with the coefficients given by

$$A_0 = \frac{2}{\ell - 1} \sum_{m=1}^{\ell-1} v(m), \quad C_j = \frac{2}{\ell - 1} \sum_{m=1}^{\ell-1} \cos\left(\frac{\pi j\left(m - \frac{1}{2}\right)}{\ell - 1}\right) v(m), \quad j = 1, \ldots, \ell - 1. \tag{30}$$

Equations (29) and (30) constitute the discrete-cosine-transform (Ref. 16) representation of a function satisfying Neumann type of boundary conditions at the end points.

C. Solution for general case

The results given in (25) and (26) will now be used to determine the Green's function[13] of the diffusion equation (10) and the Schrödinger equations (11) and (12). The linearity of the governing equations with respect to the initial conditions enables the solution to arbitrary initial conditions in terms of this Green's function. To this end we consider initial conditions of the form $p_\mu(m,0)\Delta = P_{\mu 0}\delta_m^{m_0}$, $1 \le m_0 \le \ell - 1$, where $\Sigma_{\mu=1}^4 P_{\mu 0} = 1$. This initial condition corresponds to the case where the particles are released from the location m_0 in a state μ with probability $P_{\mu 0}$. Letting $\Gamma_1 = (P_{10} - P_{30})/\Delta$ and $\Gamma_2 = (P_{20} - P_{40})/\Delta$, it is clear from the definitions that $w_1(m,0) = \delta_m^{m_0}$, $q_1(m,0) = \Gamma_1 \delta_m^{m_0}$, and $q_2(m,0) = \Gamma_2 \delta_m^{m_0}$. Using the spectral representation given in (21)–(23) for the functions $w_1(m,0)$, $q_1(m,0)$, and $q_2(m,0)$, we arrive at

$$w_1(m,0) = a_0 v_0(m_0) v_0(m) \delta_{\alpha_g}^1 + \sum_{j=1}^{\ell-1} a_j v_j(m_0) v_j(m), \tag{31}$$

$$q_1(m,0) = a_0\Gamma_1 v_0(m_0)v_0(m)\delta_{\alpha_g}^l + \Gamma_1 \sum_{j=1}^{\ell-1} a_j v_j(m_0)v_j(m), \tag{32}$$

$$q_2(m,0) = a_0\Gamma_2 v_0(m,0)v_0(m)\delta_{\alpha_g}^l + \Gamma_2 \sum_{j=1}^{\ell-1} a_j v_j(m_0)v_j(m). \tag{33}$$

Substituting (31)–(33) into (10) and (11) and recalling relations (25) and (26), we arrive at the solution for the general boundary conditions as

$$w_1(m,s) = a_0\alpha_a^s v_0(m_0)v_0(m)\delta_{\alpha_g}^l + \sum_{j=1}^{\ell-1} a_j \cos^s(k_j)v_j(m_0)v_j(m) \tag{34}$$

and

$$q_1(m,s) = a_0 v_0(m_0)\delta_{\alpha_g}^l\left[\Gamma_1 U_s\left(\frac{\alpha_a}{\sqrt{2}}\right)v_0(m) - \frac{\Gamma_2+\Gamma_1}{\sqrt{2}}U_{s-1}\left(\frac{\alpha_a}{\sqrt{2}}\right)v_0(m+1)\right] + \sum_{j=1}^{\ell-1} a_j v_j(m_0)$$
$$\times\left[\Gamma_1 U_s\left(\frac{\cos k_j}{\sqrt{2}}\right)v_j(m) - \frac{\Gamma_2+\Gamma_1}{\sqrt{2}}U_{s-1}\left(\frac{\cos k_j}{\sqrt{2}}\right)v_j(m+1)\right], \tag{35}$$

$$q_2(m,s) = a_0 v_0(m_0)\delta_{\alpha_g}^l\left[\Gamma_2 U_s\left(\frac{\alpha_a}{\sqrt{2}}\right)v_0(m) - \frac{\Gamma_2-\Gamma_1}{\sqrt{2}}U_{s-1}\left(\frac{\alpha_a}{\sqrt{2}}\right)v_0(m-1)\right] + \sum_{j=1}^{\ell-1} a_j v_j(m_0)$$
$$\times\left[\Gamma_2 U_s\left(\frac{\cos k_j}{\sqrt{2}}\right)v_j(m) - \frac{\Gamma_2-\Gamma_1}{\sqrt{2}}U_{s-1}\left(\frac{\cos k_j}{\sqrt{2}}\right)v_j(m-1)\right]. \tag{36}$$

D. Solution for totally absorbing case

We will now provide some numerical results for the special case of totally absorbing boundaries at the two ends. In this case, Eqs. (34)–(36) will be reduced to

$$w_1(m,s) = \frac{2}{\ell}\sum_{j=1}^{\ell-1} \sin\left(\frac{\pi j m_0}{\ell}\right)\sin\left(\frac{\pi j m}{\ell}\right)\cos^s\left(\frac{\pi j}{\ell}\right), \tag{37}$$

$$q_1(m,s) = \frac{2}{\ell}\sum_{j=1}^{\ell-1} \sin\left(\frac{\pi j m_0}{\ell}\right)\left[\Gamma_1 U_s\left(\frac{\cos\left(\dfrac{\pi j}{\ell}\right)}{\sqrt{2}}\right)\sin\left(\frac{\pi j m}{\ell}\right)\right.$$
$$\left. - \frac{\Gamma_2+\Gamma_1}{\sqrt{2}}U_{s-1}\left(\frac{\cos\left(\dfrac{\pi j}{\ell}\right)}{\sqrt{2}}\right)\sin\left(\frac{\pi j(m+1)}{\ell}\right)\right], \tag{38}$$
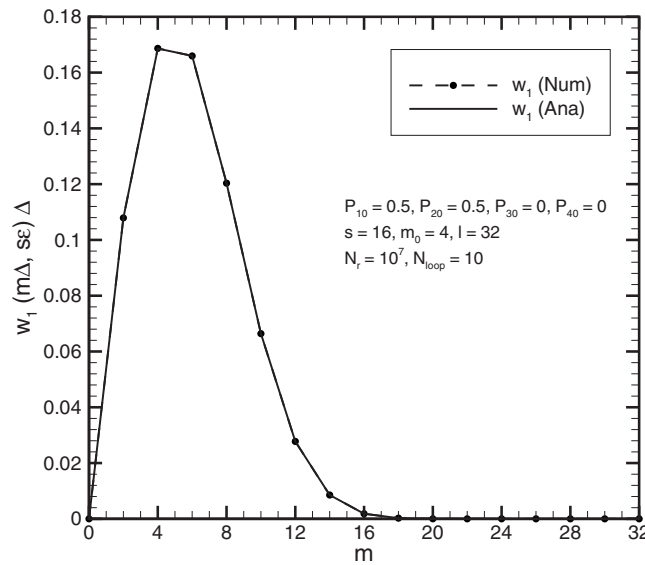
FIG. 1. Comparison of analytical solution for $w_1(m\Delta, s\epsilon)\Delta$ with that obtained from counting paths in random walk simulations for totally absorbing boundary conditions.

$$q_2(m,s) = \frac{2}{\ell}\sum_{j=1}^{\ell-1}\sin\left(\frac{\pi j m_0}{\ell}\right)\left[\Gamma_2 U_s\left(\frac{\cos\left(\frac{\pi j}{\ell}\right)}{\sqrt{2}}\right)\sin\left(\frac{\pi j m}{\ell}\right)\right.$$

$$\left. -\frac{\Gamma_2-\Gamma_1}{\sqrt{2}}U_{s-1}\left(\frac{\cos\left(\frac{\pi j}{\ell}\right)}{\sqrt{2}}\right)\sin\left(\frac{\pi j(m-1)}{\ell}\right)\right]. \tag{39}$$

Because the Green's functions satisfy reciprocity conditions, it is permissible to interchange m and m_0 in the above expressions without changing the field values. The solution for a continuous space can be obtained by carrying out the same limiting process as outlined in Ref. 7. For example, Eq. (37) reduces to the expression for the probability density function of the diffusion process with a diffusion constant D with two totally absorbing points at $x=0$ and $x=L$ and an impulsive initial condition at $x=x_0$,

$$p(x,t) = \frac{2}{L}\sum_{j=1}^{\infty}\sin\left(\frac{\pi j x_0}{L}\right)\sin\left(\frac{\pi j x}{L}\right)\exp\left(-\frac{\pi^2 j^2 D t}{2L^2}\right), \tag{40}$$

a result that is found in many texts including Ref. 9. The results given in (34)–(39) are exact, and as such, no validation is necessary. Nevertheless, it is interesting to compare the numerical data they generate with those generated through direct random walk simulations, as the latter will more likely be employed for more complicated time-dependent boundaries. In such cases, the analytical results developed here will serve more as a validation check for the numerical results generated through random walk simulations. The analytical results (labeled "Ana" in the figures) and the results obtained by counting the fractional number of paths (labeled "Num" in the figures) in the 4RW simulations with initial conditions set at $P_{10}=0.5=P_{20}$ from the location $m_0=4$ are shown in Figs. 1 and 2 at $s=16$ and for $\ell=32$. For reference, the solution for Schrödinger equation in free space is also shown in Fig. 2. For the parameters chosen in Fig. 2, the solution with boundaries will differ from the free-space case only for $0 \le m \le 12$, as is clearly seen in the figure. A large number of realizations (about 10^8) was needed to arrive at numerically converging results, particularly for the Schrödinger equation whose solution involves difference in probabilities. Both
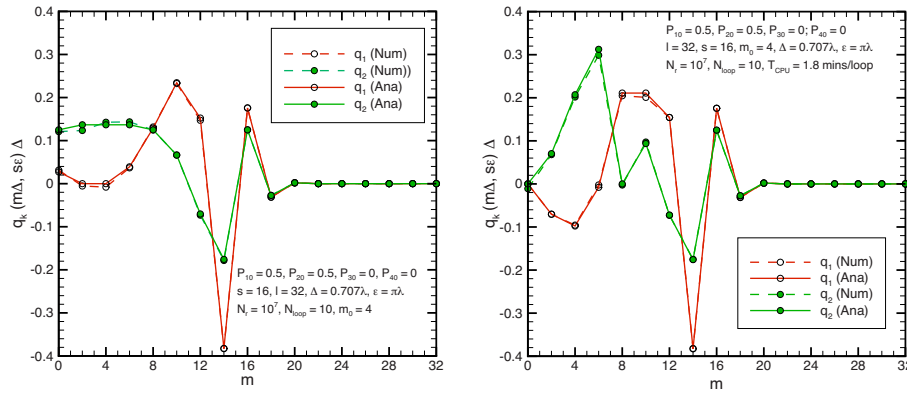
FIG. 2. (Color online) Comparison of the exact solution of Schrödinger equation with that obtained through counting paths in random walk simulations.

figures reveal that the numerical simulated results closely mimic the analytical formulas derived here. The numerical results also underscore the importance of a good numerical random number generator, particularly needed for large s, as the sample size grows exponentially with s. The use of entwined paths described in Ref. 17 is a possible means of getting around this difficulty, although details have only been demonstrated there for the relativistic case of bounded particle speed.

E. Appropriateness of the 4RW model to wave propagation problems

It might be worthwhile to comment a little on the relationship between the 4RW model and the continuous parabolic equation for which the former is being targeted in numerical computations. For the parabolic equation encountered in a number of wave propagation problems such as in underwater acoustics, radio wave propagation, and optical wave propagation in fibers, the governing equation for the field variable ψ in a homogeneous medium with time-harmonic excitation is of the form

$$\frac{\partial \psi}{\partial t} = \frac{i}{2k_0}\frac{\partial^2 \psi}{\partial x^2}, \tag{41}$$

where the independent variable t denotes the axial spatial coordinate and the variable x denotes the lateral spatial coordinate, $k_0 = 2\pi/\lambda$ is the wavenumber in the medium, and λ is the wavelength of the time-harmonic excitation. Equation (41) describes two-dimensional wave propagation in the t-x-plane subject to the approximation that all waves travel within an angle of $\theta = \pm 15°$ about the axial direction.[3] It can be shown that the maximum step size Δ in the lateral direction is restricted by $\Delta \lesssim \lambda/(2 \sin \theta_{max})$, where θ_{max} is the maximum angle of propagation with respect to the t-axis. As θ is restricted to a value less than 15° for the parabolic approximation to be valid, we may take $\sin \theta_{max} \approx \tan \theta_{max} \approx \Delta/\epsilon$. We then get the approximate relation

$$\pi\epsilon \gtrsim k_0\Delta^2. \tag{42}$$

It may be remarked parenthetically that the inequality (42) translates to the condition that the Schrödinger equation is valid for describing particle motion for nonrelativistic particle speeds with the normalized speed $v/c \lesssim \tan \theta_{max} \approx 0.27$ for $\theta_{max} = 15°$, where c is the speed of light in free space. In the 4RW model, the relation between the step sizes of the form $\epsilon = k_0\Delta^2$ is implied and this is consistent with the inequality (42) If $\Delta = \lambda/\sqrt{2}$, then this relation implies that $\epsilon = \pi\lambda$. Both of these values are well within the maximum values permitted by the parabolic equation approximation and it is believed that the 4RW model constitutes a very appropriate discretization scheme for numerically handling the parabolic equation.

IV. CONCLUSIONS

Analytical expressions have been provided for the transitional probabilities of a 4RW model on a lattice constrained in space with dissimilar boundaries and subject to partially reflecting boundary conditions. Special cases of perfectly absorbing boundaries and perfectly reflecting boundaries have been treated. Solution for the transitional probabilities evaluated at time s to the diffusion process is shown to involve sth power of the averaging operator D_x, whereas those of the Schrödinger equation involve Chebyshev polynomials of the second kind of order s and $s-1$ with argument $D_x/\sqrt{2}$. These are the general characteristics of diffusion and Schrödinger processes in the 4RW model irrespective of the boundary conditions. Different boundary conditions will dictate different choices of the eigenfunctions in which the initial probabilities at $s=0$ are expanded. The eigenfunctions in the most general case will involve exponential function as well as harmonic functions. The exponential function will only exist when the parameters present in the boundary conditions satisfy certain relationship. While the results presented in this paper should have a significance of their own for random walk with dissimilar boundaries, it is hoped that they will also serve as benchmark cases for numerical stochastic methods designed to solve more complicated situations. Although it had not been the major focus of the current paper, numerical implementation of the random walk solution necessitates the availability of an effective random number generator to sufficiently populate all portions of the sample space. This is particularly critical for field evaluated at large times. Extension of these results to higher dimensions and to situations with a potential field is a topic worthy of further study and will be taken up in the future.

[1] G. N. Ord and A. S. Deakin, J. Phys. A **30**, 819 (1997).

[2] G. N. Ord and J. A. Gualtieri, Phys. Rev. Lett. **89**, 250403 (2002).

[3] F. B. Jensen, W. A. Kuperman, M. B. Porter, and H. Schmidt, *Computational Ocean Acoustics* (Springer, New York, 1994).

[4] J. R. Kuttler and R. Janaswamy, Radio Sci. **37**, 5-1 (2002).

[5] R. Janaswamy, IEEE Applied Electromagnetics Conference, Kolkata, India, 2007, Vol. 1, Paper No. AEMC.2007.4638046, pp. 1–4; available online at http://ieeexplore.ieee.org/arnumber=4638046&isnumber=4637999&punumber=4629478.

[6] B. V. Budaev and D. B. Bogy, Q. J. Mech. Appl. Math. **55**, 209 (2002).

[7] R. Janaswamy, J. Phys. A: Math. Theor. **41**, 155306 (2008).

[8] J. C. Strikwerda, *Finite Difference Schemes and Partial Differential Equations*, 2nd ed. (Society of Industrial and Applied Math, Philadelphia, PA, 2004).

[9] G. H. Weiss, *Aspects and Applications of the Random Walk* (North-Holland, New York, NY, 1994).

[10] F. B. Knight, *Essentials of Brownian Motion and Diffusion* (American Mathematical Society, New York, NY, 1981).

[11] J. Masoliver, J. M. Porra, and G. H. Weiss, Phys. Rev. E **48**, 939 (1993).

[12] G. N. Ord, Ann. Phys. **250**, 51 (1996).

[13] G. Barton, *Elements of Green's Functions and Propagation* (Oxford University Press, New York, NY, 1989).

[14] W. Feller, *An Introduction to Probability Theory and Its Applications*, 2nd ed. (Wiley, New York, NY, 1970), Vol. 2.

[15] E. W. Montroll, J. Math. Phys. **6**, 167 (1965).

[16] S. A. Martucci, IEEE Trans. Signal Process. **42**, 1038 (1994).

[17] G. N. Ord, J. A. Gualtieri, and R. B. Mann, Found. Phys. Lett. **19**, 471 (2006).

Angular Correlation Properties With Random Multiple Scattering

Jie Xu, *Member, IEEE*, and Ramakrishna Janaswamy, *Fellow, IEEE*

Abstract—The angular correlation of received fields in multipath environments is studied. The focus is put on two-dimensional (2-D) cases, and the frequently used uncorrelated scattering assumption is tested through full-wave Monte Carlo simulations. The results show that this assumption is valid for the discrete finite spectra of the received waves when the scattering objects in the environments are distributed in complete randomness, either when they are surrounding the transmit/receive regions or in clusters away from them. The correlation among wave components from different angles increases only when the randomness of the scatterer deployment is reduced.

Index Terms—Angular correlation, discrete finite spectrum, random media, uncorrelated scattering assumption.

I. INTRODUCTION

THE angular spectrum of certain electromagnetic (EM) field in the presence of a multipath environment is the complex amplitude of the plane wave components that consist of the field arriving from different angles at a finite sized receive volume. Its properties are of special use to the determination of the multipath richness of the field, which in turn is crucial to the performance of either the simpler spatial diversity schemes [1] or the more advanced multiple-input-multiple-output (MIMO) systems [2]. The multipath richness depends not only on the angular spread within which waves are incident onto the receive volume, but also on the correlation between different angular wave components [3]. Generally speaking, the wider the angular spread and the less correlated the angular components are, the more multipath richness there is in the received field.

The uncorrelated scattering assumption is an *angular* correlation model frequently adopted by researchers for random multipath propagation studies [4]–[8]. The term "uncorrelated scattering" here is consistent with the one adopted by a recent study of Kennedy *et al.* [8], and it assumes that the scattered wave received from different angles are completely uncorrelated. Most of the time it is further assumed that the angular spectrum is also zero mean, which will be shown later in this study to be actually redundant. This uncorrelated angular scattering assumption is different from the wide sense stationary uncorrelated scattering

(WSSUS) assumption proposed by Bello [4] on a first look. However, it was pointed out in [3] that the WSSUS assumption can eventually lead to the uncorrelated angular scattering assumption, which is the subject of interest here. The mathematical tractability of this model makes it very popular in the literature when closed form conclusions and qualitative interpretations are sought after. Although most researchers agree that this assumption is only a convenient mathematical idealization, little work has been done to determine its validity and how well it represents a true random environment. Therefore, the objective of this work is to study the autocorrelation of the angular spectra of scattered EM waves in the presence of discrete random media, and to investigate the validity and applicability of the uncorrelated scattering assumption.

A majority part of this work is carried out by solving scattering problems that represent multipath environments through surface integral equation based full wave techniques [9], [10]. The operation frequency is chosen to be 3 GHz. For the 2-D systems under consideration, the scattering objects are modeled by lossy dielectric cylinders of different shapes. The complex dielectric constant is taken to be that of bricks at 3 GHz, $2.7 + i0.034$ [11], which can be used to approximate building structures in outdoor environments. Different or multiple dielectric constants could be used, and it will only influence the complexity of the numerical calculations. When either the real permittivity or the conductivity of the material varies, the corresponding wavelength changes, which requires different discretizations on different object surfaces. However, it is believed that the final conclusions of the study will be independent of specific values. As will be shown by the numerical results presented later, the validity of the uncorrelated scattering assumption is determined by the randomness of the scattering object placement. For more efficient solution of the problems, the fast multipole method (FMM) is used [12], [13], which can directly results in the angular spectra of the fields in a finite receive volume. To obtain the correlation information between different angular wave components, the Monte Carlo simulation technique is utilized, and the number of realizations that consist the sample pool is about 500 for every case studied.

The rest of the paper is structured as follows. Section II introduces the basic concepts and mathematical essentials of the study. Some important practical considerations concerning the angular spectra are pointed out in Section III. The angular correlation of the scattered waves is then studied through full wave Monte Carlo simulations, and the obtained results are presented and discussed in Section IV. Finally Section V concludes this study. Throughout the work, a 2-D time-harmonic propagation scenario is assumed. The $e^{-i\omega t}$ time convention is adopted, where ω is the radian frequency of the waves.

The authors are with the Department of Electrical and Computer Engineering, University of Massachusetts Amherst, Amherst, MA 01003 USA (e-mail: jixu@ecs.umass.edu; janaswamy@ecs.umass.edu).

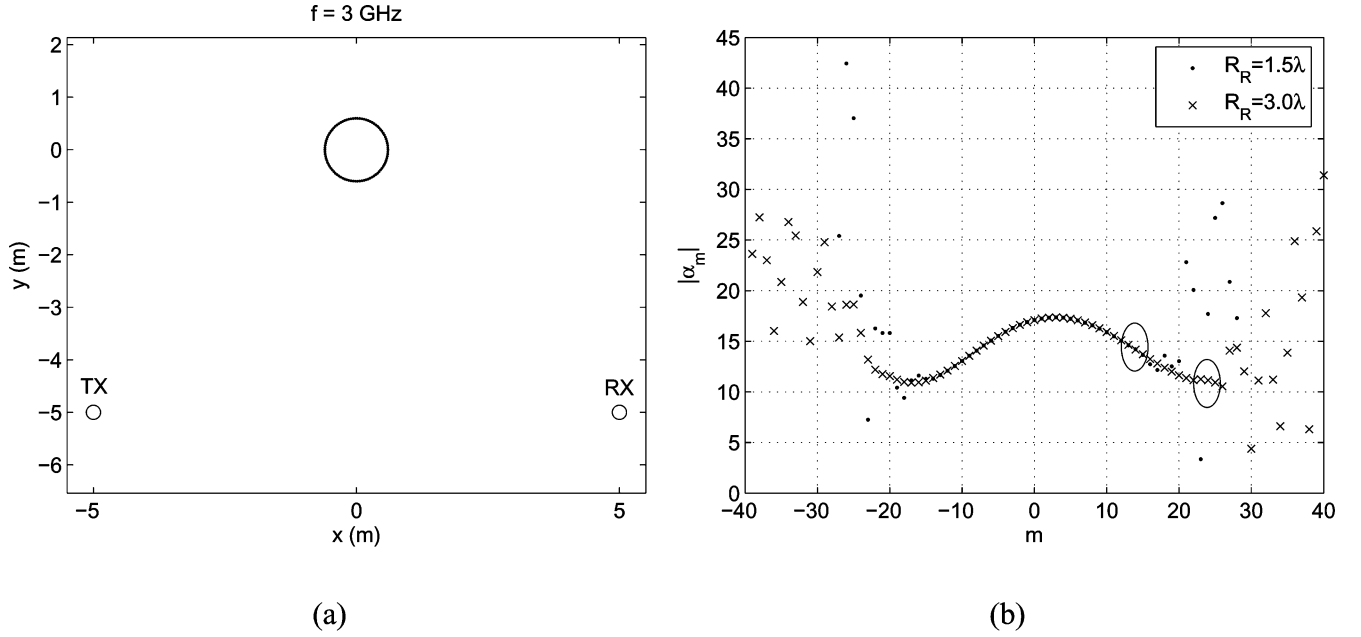Fig. 1.   Errors in $\{\alpha_m\}$ due to ill-posedness of numerical computation. (a) Configuration of a scattering system. (b) Computed coefficients.

II. THEORY

A. Angular Spectrum

Consider a finite obstacle free receive volume V_R in two dimensions, and assume that it can be enclosed by an imaginary circle of radius R_R, which is also obstacle free. It is well known that the scattered field, which satisfies the 2-D homogeneous Helmholtz equation, takes the form

$$\psi_s(\boldsymbol{\rho}) = \sum_{m=-\infty}^{\infty} \alpha_m J_m(k_0\rho)e^{im\phi}$$
$$\approx \sum_{m=-M_R+1}^{M_R} \alpha_m J_m(k_0\rho)e^{im\phi} \qquad (1)$$

in the circular area irrespective of the sources and scattering objects outside [14]. In (1), $J_m(\cdot)$ is the Bessel function of the first kind and of order m, $\boldsymbol{\rho} = (\rho, \phi)$ is the local cylindrical coordinate of the observation point with respect to the center of the circle, $k_0 = (2\pi/\lambda)$ is the wavenumber in the background medium (λ is the wavelength), and α_m is the expansion coefficient for the mth cylindrical harmonic. For a given accuracy requirement, the series can be truncated into a finite length $M_R = \sigma k_0 R_R$, where the factor σ is a constant number slightly greater than unity and controls the accuracy of the truncation. It is indicated in [15] that a sufficient condition to ensure the convergence of the truncated series is $\sigma \geq e/2$. Notice must be taken that for the series to converge, it does not require the coefficients α_m to approach zero when $|m| \to \infty$. As a matter of fact, it is the exponential decay property of high order $|J_m(k_0\rho)|$ that ensures the convergence [12], [15], [16].

By using the integral representation of the Bessel functions $J_m(z) = (1/2\pi)\int_0^{2\pi} e^{iz\cos\theta}e^{im(\theta-(\pi/2))}d\theta$, (1) can be rewritten as

$$\psi_s(\boldsymbol{\rho}) = \int_0^{2\pi} a(\theta)e^{ik_0\rho\cos(\theta-\phi)}d\theta$$
$$\approx \int_0^{2\pi} a_e(\theta)e^{ik_0\rho\cos(\phi-\theta)}d\theta \qquad (2)$$

where

$$a(\theta) \triangleq \frac{1}{2\pi} \sum_{m=-\infty}^{\infty} \alpha_m e^{im(\theta-(\pi/2))}, \qquad (3)$$

$$a_e(\theta) \triangleq \frac{1}{2\pi} \sum_{m=-M_R+1}^{M_R} \alpha_m e^{im(\theta-(\pi/2))}. \qquad (4)$$

act as the complex amplitudes of the plane wave components of the received scattered field, and will be distinguished from each other in this study as the true and effective finite angular spectra of the field, respectively. It is seen that both spectra are continuous functions of propagation angle θ, and all the plane wave components are considered to be propagating waves. Furthermore, the angular spectra are in the form of Fourier series whose coefficients are $\{i^{-m}\alpha_m/2\pi\}$, and it is straightforward to obtain the cylindrical harmonic coefficients $\{\alpha_m\}$ from the Fourier coefficients of $a(\theta)$ by

$$\alpha_m = i^m \int_0^{2\pi} a(\theta)e^{-im\theta}d\theta. \qquad (5)$$

Analogous to representing a periodic time domain signal in its Fourier series, the different coefficients $\{\alpha_m\}$ in (3) and (4) correspond to different *frequencies* consisting of the angular spectra. Clearly, the finite spectrum is obtained from the true one by neglecting all the high frequency contents, i.e., assuming $\alpha_m = 0$ for $|m| > M_R$. Since the actual values of
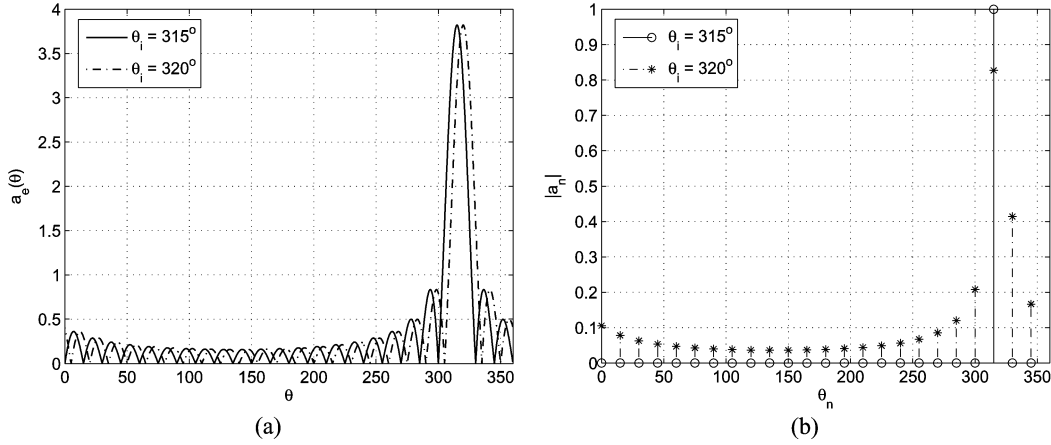
Fig. 2. Finite angular spectra. (a) Continuous spectra. (b) Discrete spectra.

α_m in this range may not be negligible, the finite spectrum is not necessarily a close approximation of the true one. However, because $J_m(\rho)$ decays exponentially when $n > \rho$, the two spectra produce practically the same field in the receive volume. Without causing any confusion, the term *frequency* will be used throughout the rest of this work referring to the frequency components of angular spectra.

The true angular spectrum of the scattered field is meaningful if all orders of $\{\alpha_m\}$ are available *a priori*. On the other hand, given the field in the finite receive volume only, it is extremely difficult, if not impossible, to obtain its true angular spectrum, because the high frequency components produce practically zero field in the volume and the inverse problem becomes ill-posed. Physically, a finite aperture only provides limited angular resolution [17], [18]. In order to appreciate the higher angular frequencies, the size of the aperture has to be increased. Due to this reason, what really matters for the scattered field in the receive volume is the finite spectrum.

B. Uncorrelated Scattering Assumption

In a random environment, the angular spectrum of the field in a finite receive volume is a random process. The autocorrelation function of this process is usually called the angular correlation of the field

$$R(\theta, \theta') \triangleq \mathcal{E}\{a(\theta)a^*(\theta')\} \tag{6}$$

where $\mathcal{E}\{\cdot\}$ represents expectation and * represents complex conjugate. The uncorrelated scattering assumption assumes that the scattered waves from different angles are completely uncorrelated, which can be represented mathematically as

$$\mathcal{E}\{a(\theta)a^*(\theta')\} = \mathcal{E}\{a(\theta)\}\mathcal{E}\{a^*(\theta')\}, \quad \theta \neq \theta' \tag{7}$$

for *nonzero* mean $a(\theta)$. By substituting (3) into both sides of (7), it is easy to arrive at

$$\mathcal{E}\{\alpha_m\alpha_n^*\} = \mathcal{E}\{\alpha_m\}\mathcal{E}\{\alpha_n^*\} \tag{8}$$

for any m and n. Then using (8) with $m = n$, one can find out that the variance of α_m is zero for any order m, i.e.,

$$\mathcal{E}\left\{|\alpha_m - \mathcal{E}\{\alpha_m\}|^2\right\} = 0, \ \forall \, m. \tag{9}$$

This suggests that the sequence of "random variables" $\{\alpha_m\}$ are actually constants with probability 1, and hence $a(\theta)$ becomes a deterministic function, which is contradictory to the starting point that angular spectrum is a random process. The only case of resolving this contradiction is when the spectrum is a *zero mean* process, for which the uncorrelated scattering assumption takes the form

$$\mathcal{E}\{a(\theta)a^*(\theta')\} = P(\theta)\delta(\theta - \theta') \tag{10}$$

where $P(\theta)$ is the angular power spectrum proportional to $\mathcal{E}\left\{|a(\theta)|^2\right\}$, and $\delta(\cdot)$ is the Dirac delta function. One can easily check (see the Appendix) that the sufficient and necessary condition for (10) is

$$\mathcal{E}\{\alpha_m\alpha_n^*\} = i^{(m-n)} \int_0^{2\pi} P(\theta)e^{-i(m-n)\theta}d\theta \tag{11}$$

which is a function of only the order difference $(m - n)$ related to the $(m - n)$th Fourier coefficient of the angular power spectrum. Now one can clearly see that the uncorrelated scattering assumption for the true angular spectrum (zero mean) of the received field is equivalent to a stationary coefficient correlation of its Fourier series expansion. It is also worth mentioning here that the Fourier coefficients of the angular power spectrum completely determines the spatial correlation of the field as suggested in [6].

From this alternative form of the uncorrelated scattering assumption, it can be deduced that the expansion coefficient α_m may not become negligibly small for large orders almost surely. Otherwise setting $m = n$ in (11) will lead to $\mathcal{E}\left\{|\alpha_m|^2\right\} = \mathcal{E}\left\{|\alpha_\infty|^2\right\} = 0$ for any finite m, which suggests a zero scattered field in the receive volume. However, it is reiterated here that even though the high frequency components of the true angular spectrum may have significant amplitudes when the uncorrelated scattering assumption is valid, they are of no practical relevance to the finite receive volume because of the resulting negligibly small field caused by higher order Bessel functions.

III. PRACTICAL CONSIDERATIONS

Given the field in a finite-sized receive volume, only the coefficients $\{\alpha_m\}$ roughly in the order range $|m| < M_R =$
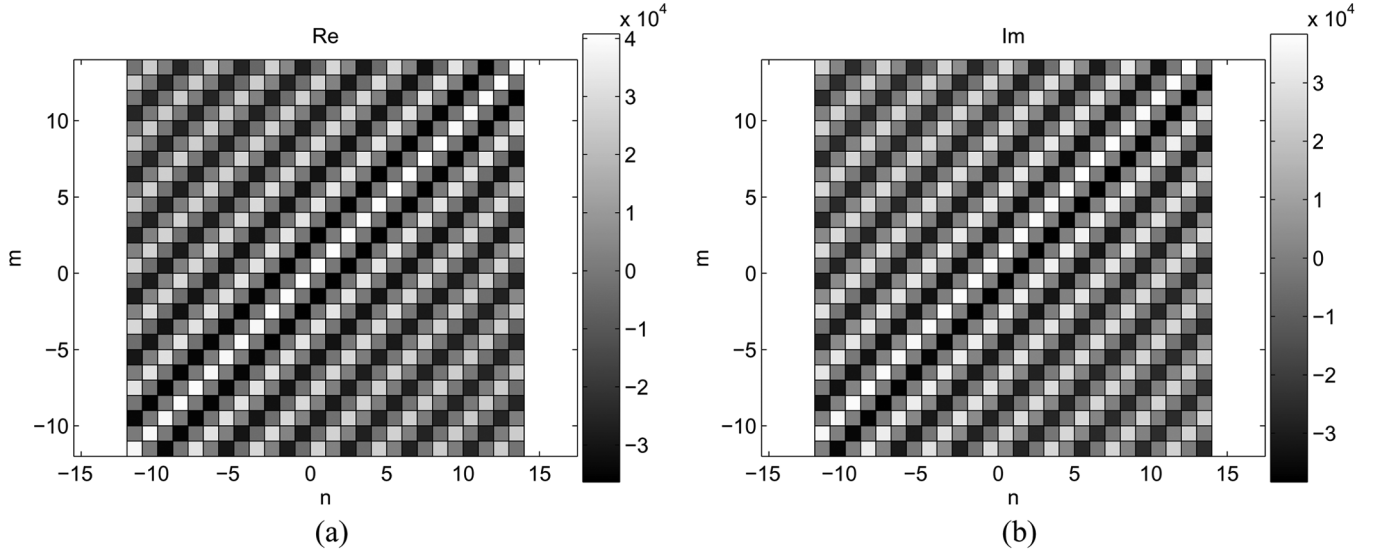
Fig. 3. $\mathcal{E}\{\alpha_m \alpha_n^*\}$ for systems where 51 cylinders are around the receive volume. (a) Real part. (b) Imaginary part.

$(e\pi R_R/\lambda)$ can be correctly computed with high confidence. Noise and numerical errors can easily blow up the higher orders during the inverse process due to their ill-posedness. One way of obtaining $\{\alpha_m\}$ is to solve the corresponding scattering problem by the means of surface integral equations [9], [10] and apply the fast multiple method (FMM) [12], [13], provided that all the scatterers are separated from the receive volume by at least a distance that is comparable to the size of the volume (to roughly ensure the physics of propagating plane waves). Fig. 1 shows a system with a single circular dielectric scattering cylinder and the computed coefficients $\{\alpha_m\}$. The radius of the cylinder is 6λ and its dielectric constant is $2.27 + i0.034$. The transmitter (TX) is a unit-amplitude electric line source, and the receive volume (RX) is a circular region whose radius is taken to be 1.5λ and 3.0λ for two cases. It can be seen from Fig. 1(b) that for both receive volume sizes the computed higher order coefficients deviate from the smooth curve formed by the lower ones, which is a manifestation of the errors incurred. The positions of the deviation are marked by two ellipses, which are around $|m| = 12$ and $|m| = 23$, respectively. These results suggest that it is unlikely to obtain the true angular spectra by manipulating the fields in a finite receive region.

In principle, the true spectra can be acquired by measurement provided that the equipment is ideal, i.e., the receive antenna has an infinitely narrow beam. However, any practical antenna only has a receive pattern with finite beam width, which makes it difficult to resolve the fast oscillating components of the angular spectra. Therefore, it is still difficult to get the true angular spectra, and the left-hand side (LHS) of (10) cannot be evaluated directly. To test the uncorrelated scattering assumption, one can only rely on the stationarity of (11) in the correctly computable low frequency range as a partial verification.

Due to this inability to determine the true angular spectra, it is more reasonable to focus on the finite spectra in (4), which produce practically the same field in the receive volume as do the true ones. Furthermore, since a finite spectrum excludes all the higher frequencies, it is also possible to approximate the
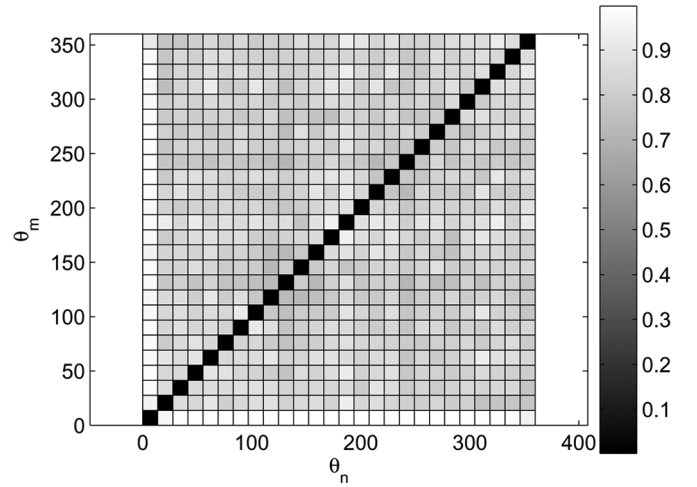

Fig. 4. $1 - |C_e(\theta_m, \theta_n)|$ for systems where 51 cylinders are around the receive volume.

corresponding integration in (2) as a summation of finite terms following the trapezoidal rule

$$\psi_s(\boldsymbol{\rho}) \approx \sum_{n=0}^{N_R-1} a_e(\theta_n) e^{ik_0 \rho \cos(\phi - \theta_n)} \Delta\theta \qquad (12)$$

where $\theta_n = (2n\pi/N_R)$, $n = 0, 1, \ldots, N_R - 1$ is a predefined uniform angular grid, $\Delta\theta = (2\pi/N_R)$ is the grid size, and $N_R = 2M_R$ is the grid number. The grid number here is taken to be the same as the number of observable frequency components in the spectrum, and the accuracy is assured as suggested by Rokhlin in his development of the FMM [12] and the bandwidth consideration mentioned by Chew [16]. The grid size $\Delta\theta$ can also be interpreted as the angular resolution of the receive volume, and (12) suggests that this resolution is fine enough to reconstruct the field everywhere inside the volume. If one further defines $a_n = a_e(\theta_n)\Delta\theta$, the sequence $\{a_n, n = $
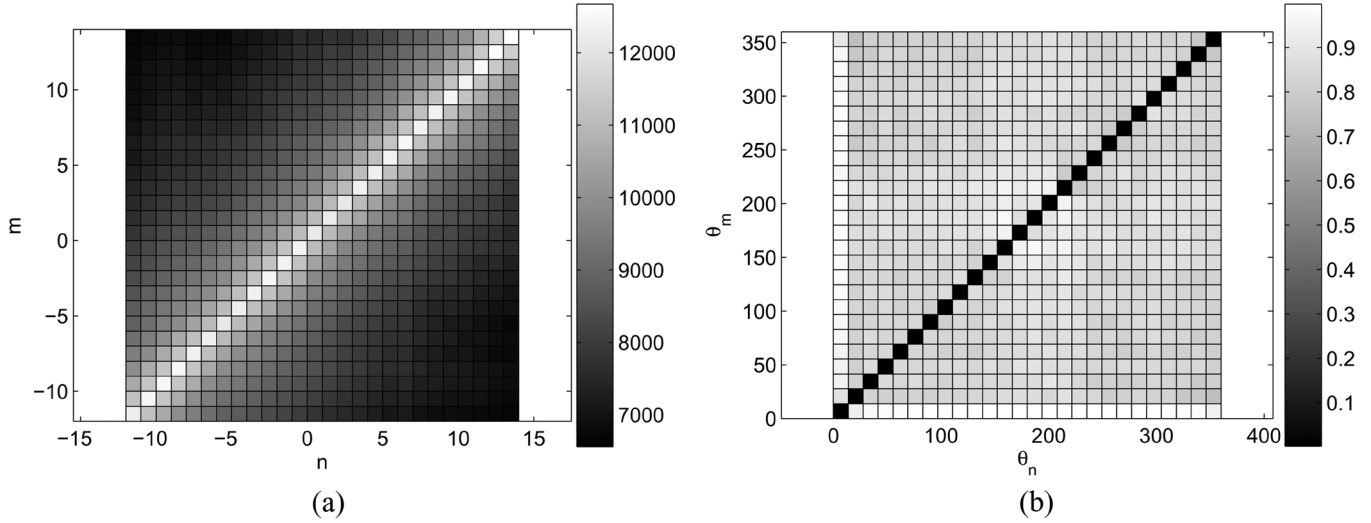
Fig. 5. System with four groups of three cylinders around the receive volume. (a) $|\mathcal{E}\{\alpha_m \alpha_n^*\}|$. (b) $1 - |C_e(\theta_m, \theta_n)|$.

$0, \ldots, N_R - 1\}$ constitutes a discrete finite spectrum of the received scattered field.

The finite spectrum does not satisfy the uncorrelated scattering assumption because it is easy to check that the correlation between its Fourier coefficients of various orders is not statistically stationary. Even so, it is still possible that two of its angular components that are separated far enough are uncorrelated or only weakly correlated, which mathematically means

$$\mathcal{E}\{a_e(\theta) a_e^*(\theta')\} \approx 0, \text{ for } \Theta \leq |\theta - \theta'| \leq 2\pi - \Theta \qquad (13)$$

with $\theta, \theta' \in [0, 2\pi]$. Furthermore, due to the limited angular resolution associated with the finite receive volume, it is unnecessary to seek for correlation between angles separated less than the resolution size $\Delta\theta$. Therefore, it would be interesting to test if (13) is true for $\Theta = \Delta\theta$. In the numerical results presented in Section IV, the angular correlation will only be evaluated among the discrete wave angles $\{\theta_n\}$. Moreover, for better illustration of the results, the normalized autocorrelation coefficient is considered

$$C_e(\theta_m, \theta_n) \triangleq$$
$$\frac{\mathcal{E}\{[a_e(\theta_m) - \mathcal{E}\{a_e(\theta_m)\}] [a_e^*(\theta_n) - \mathcal{E}\{a_e^*(\theta_n)\}]\}}{\sqrt{|a_e(\theta_m) - \mathcal{E}\{a_e(\theta_m)\}|^2 |a_e^*(\theta_n) - \mathcal{E}\{a_e^*(\theta_n)\}|^2}}. \qquad (14)$$

Another issue worth mentioning is the relation between the true and finite angular spectra. Compared to the true spectrum, even though the finite one ignores all the high frequency components a_m for $|m| > M_R$, which might actually have significant amplitude, it is still possible that the two resemble each other quite well (see the example that follows). When the discrete finite spectra are considered, the errors come not only from the frequency domain truncation, but also possibly from angle mismatching, which is also demonstrated by the following example.

When a single plane wave is incident upon a circular receive volume centered at the origin, the true angular spectrum is clearly nonzero for only one angle, i.e., $a(\theta) = \delta(\theta - \theta_i)$, where θ_i is the incident angle. The corresponding coefficients are $\{\alpha_m = i^m e^{-im\theta_i}\}$, which are of unit magnitude up to infinite order. Suppose the radius of the receive volume is 1.5λ, the

finite spectrum includes $N_R = 24$ low frequency components. Fig. 2 shows the continuous and discrete finite angular spectra $a_e(\theta)$ and a_n with incident angle $\theta_i = 315°$ and $\theta_i = 320°$. The ripples in the continuous finite spectra of Fig. 2(a) are obviously caused by ignoring the high frequency components. However, the strong peaks in the figure correctly identify the incident angles. For the discrete finite spectra in Fig. 2(b), when $\theta_i = 315°$, it is correctly indicated that there is only one angular component. However, when $\theta_i = 320°$, all the other components are also present. This is because $\theta_i = 315°$ is one of the pre-defined angles $\{\theta_n\}$ while $\theta_i = 320°$ is not. The mismatching between the incident angle and the uniform grid requires all angular components to appear as a compensation.

IV. SIMULATION RESULTS

This section studies a number of different scenarios and the validity of the uncorrelated scattering assumption is tested. In the first system studied, a line source transmitter and a circular receive volume of radius 1.5λ are separated by 100λ. Dielectric scattering cylinders of different shapes are randomly distributed in a circular ring around the receive volume in a nearly uniform way, with the only requirement being that the scatterers do not overlap with each other. The inner radius of the ring is 5λ and the outer radius is 65λ. The shapes of the cylinder can be circular, elliptical, or square, but they all have the same perimeter $6\pi\lambda$. Fig. 3 shows the grayscale plots of the real and imaginary parts of the correlation $\mathcal{E}\{\alpha_m \alpha_n^*\}$ when the number of cylinders is 51 (corresponding to a scatterer area density around 11.5%). It can be seen that $\mathcal{E}\{\alpha_m \alpha_n^*\}$ is only a function of the difference between the two indices m and n. This stationarity suggests that it is likely that the true angular spectra satisfy the uncorrelated scattering assumption. To accentuate high correlation with dark grayscale, Fig. 4 shows the amplitude of the simulated complementary angular correlation of the discrete finite spectra, i.e., $1 - |C_e(\theta_m, \theta_n)|$. For the complementary correlation coefficient, values close to zero indicate high correlation. The waves from two distinct discrete angles are seen to be almost uncorrelated, suggesting that (13) is valid. The few weakly correlated
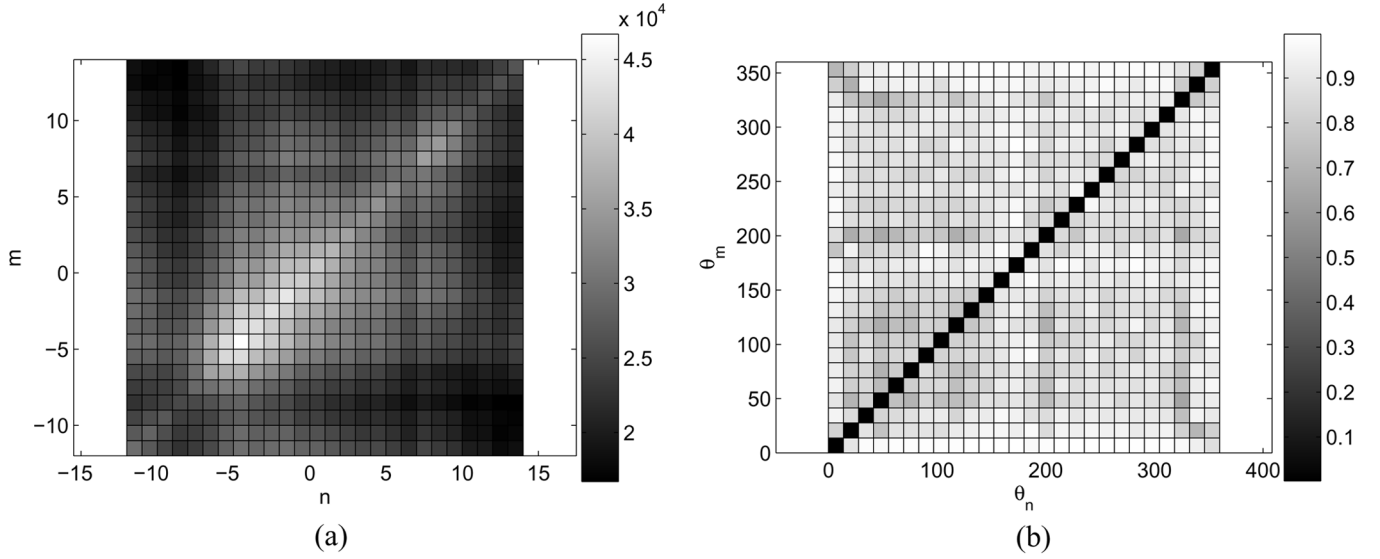
Fig. 6. System with 36 cylinders distributed around the receive volume in partial randomness. (a) $|\mathcal{E}\{\alpha_m \alpha_n^*\}|$. (b) $1 - |C_e(\theta_m, \theta_n)|$.
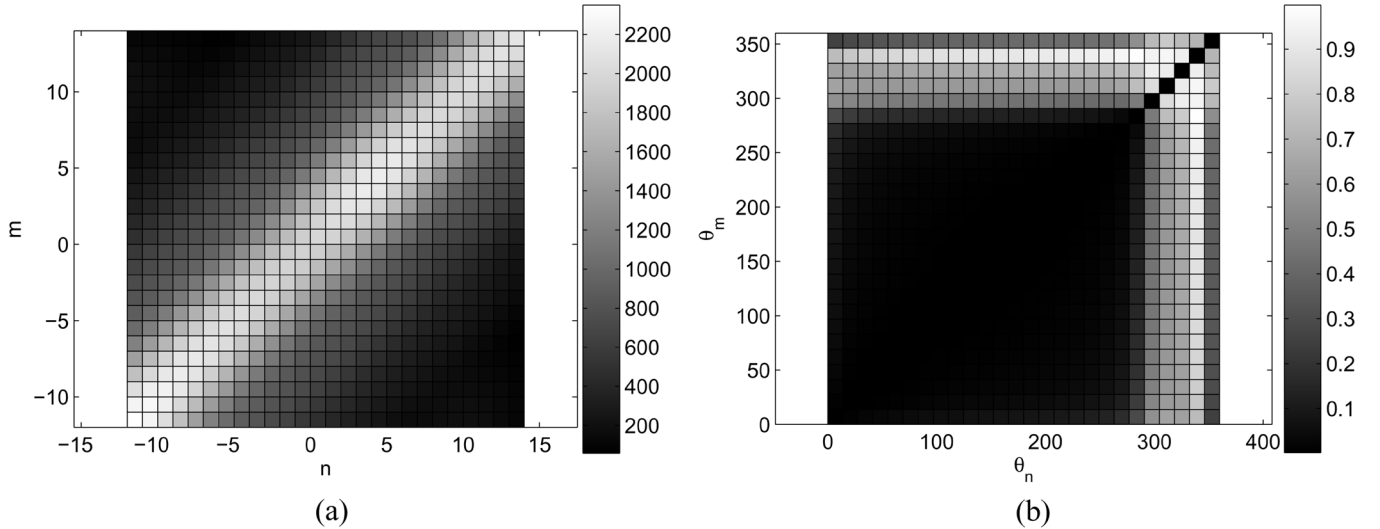

Fig. 7. System with 24 cylinders distributed in a cluster away from transmit and receive volumes. (a) $|\mathcal{E}\{\alpha_m \alpha_n^*\}|$. (b) $1 - |C_e(\theta_m, \theta_n)|$.

spots around the diagonal line may be due to the errors from the numerical calculation or insufficient number of realizations. Different number of cylinders are also used to see the effect of scatterer density. The results are similar to those in Figs. 3 and 4, suggesting that the uncorrelated scattering assumption is not strongly affected by the scatterer density of the system.

Next, one cylinder of each shape (3 total) are used to form a group, and such groups of cylinders are distributed in the scattering region. The relative positions of the cylinders within a group are fixed, but the groups can still be randomly located and orientated. Fig. 5 shows the results with 4 groups (12 cylinders), and similar observations to before can be made. For this case, each group can be viewed as one complicated scattering object.

Then, a system similar to the first one is considered, but the randomness of the cylinder placement is decreased. Fig. 6 shows the results with 36 cylinders surrounding the receive volume. However, among these cylinders, only half of them are ran-

domly distributed, with the other half taking fixed locations and orientations. It is observed that although the discrete angular spectrum still looks somehow uncorrelated, the correlation $\mathcal{E}\{\alpha_m \alpha_n^*\}$ is no longer a stationary function, and hence the uncorrelated scattering assumption is violated.

In another type of system, 24 scattering cylinders are placed in a circular cluster of 40λ radius separated from both the transmit and the receive volumes. The cluster is in the direction of $45°$ to the transmitter and $135°$ to the receiver, the same geometry as Fig. 1(a) with the single cylinder replaced by a cluster. The simulated results are presented in Fig. 7. It can be seen that the coefficients $\{\alpha_m\}$ satisfy the stationarity condition less as well as the previous cases. The finite discrete angular spectrum appears to be correlated in the angular range $0°$–$270°$ but uncorrelated from $270°$ to $360°$, which is about the angular range of the actual scattered waves from the cluster. Physically there should be no angular components whatsoever coming from the range $0°$–$270°$. It is believed that the seemingly
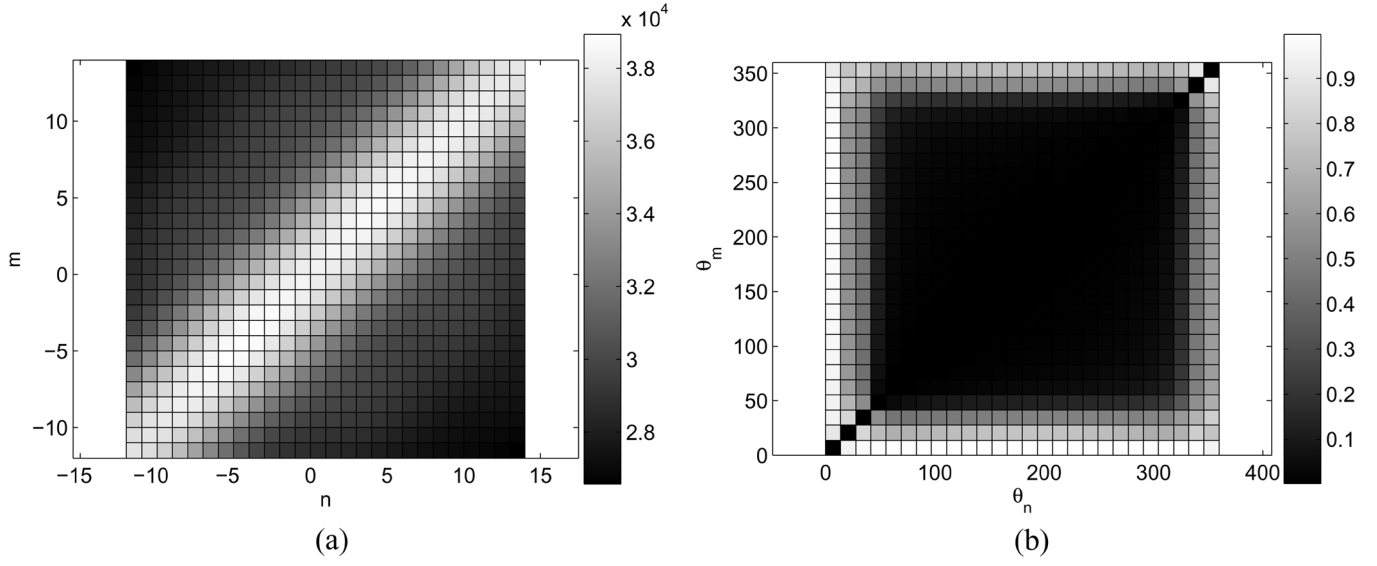
Fig. 8.   System with 51 cylinders around the transmitter. (a) $|\mathcal{E}\{\alpha_m \alpha_n^*\}|$. (b) $1 - |C_e(\theta_m, \theta_n)|$.
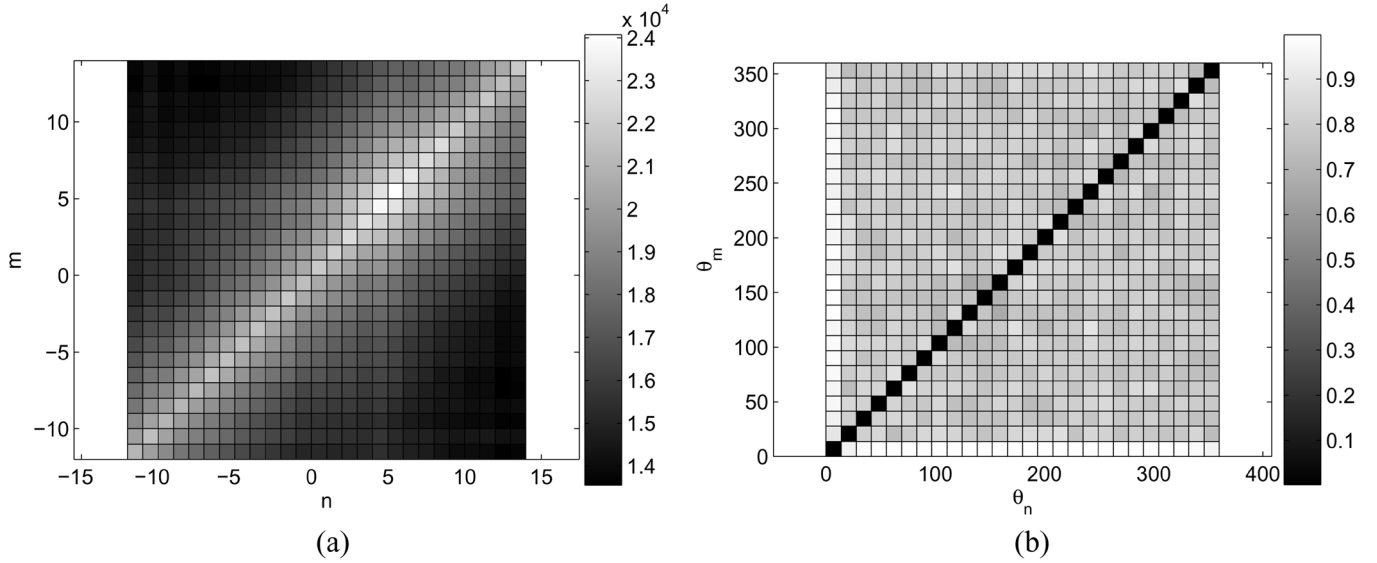

Fig. 9.   System with 24 cylinders around the transmitter and receiver, respectively. (a) $|\mathcal{E}\{\alpha_m \alpha_n^*\}|$. (b) $1 - |C_e(\theta_m, \theta_n)|$.

correlation in this range is due the errors introduced by truncating the series in (4) and angle mismatching discussed in the previous section. Hence, it is still possible that the uncorrelated scattering assumption is valid for the true spectrum, and (13) is true for the discrete finite spectrum.

Next, scatterers are distributed in a circular ring around the transmit volume instead of the receive volume. The size of the ring is the same as before. Fig. 8 shows the magnitudes of $\mathcal{E}\{\alpha_m \alpha_n^*\}$ and the complementary correlation coefficient $1 - |C_e(\theta_m, \theta_n)|$ with 51 cylinders as scatterers. Observations similar to the case of Fig. 7 are also made here, where the angular range of uncorrelated finite spectrum is correctly identified at around $-20°$–$20°$. The same arguments as the previous case can be made.

In the last system studied, 24 scatterers each are randomly distributed in circular rings around both the transmit volume and the receive volume. The results are shown in Fig. 9, and

the wave components from different angles are observed to be uncorrelated. A simple comparison with Figs. 4 and 8 reveals that the wave behavior of the received field in this system is dominated by the influence of the scatterers immediately around the receive volume, which is a very reasonable outcome.

V. Conclusion and Discussion

By studying the angular components of the scattered field in a finite-sized receive volume in the presence of various scattering environments, the validity of the uncorrelated scattering assumption is investigated numerically through rigorous full wave electromagnetic simulation. The results about the stationarity of the spectrum coefficients indicate that it is likely that the assumption is generally valid for the true spectra in systems where scattering objects can take their positions and orientations completely randomly, no matter they are around the receive volume, the transmitter, or in clusters separated

from them. In the meanwhile, the results of the correlation coefficients among the discrete plane wave components directly suggest that the discrete finite spectra are also likely to be uncorrelated when the scattering object placement is completely random. However, as soon as the randomness of the scatterer placement is decreased, the assumption is observed to break down in the sense that the correlation of the spectrum expansion coefficients is no longer stationary. Intuitively, there is a direct cause-effect relationship between the randomness of the scatterer deployment and the validity of the uncorrelated scattering assumption. In outdoor environments where a large number of objects can move around freely, this assumption might be a good model to describe the multipath wave propagation.

The case when the receiver is moving with constant velocity is of special interest when properties such as space-time cross correlation and space-frequency cross correlation are desired [19]. For such cases, the field as a function of the receiver location, which in turn is a function of time t, can be obtained from (2) as $\psi_s(t) = \int_0^{2\pi} a(\theta) e^{ik_0\rho_o \cos(\theta-\phi_o)} e^{i\omega_d t \cos(\theta-\alpha)} d\theta$, where (ρ_o, θ_o) is the initial location of the receiver, $\omega_d = k_0 v$ is the maximum Doppler frequency shift, and α is the direction angle in which the receiver moves at velocity v. Similar analysis can be carried out and the same conclusion about the angular correlation of the wave spectrum can be reached, provided that the receiver does not move out of the receive volume. Outside the volume, the starting (1) may not be valid.

Furthermore, even though the study presented here is only for the received field, the transmit side can be included simply by considering reciprocity of the systems, and the uncorrelated scattering assumption can be easily extended to the double-angular domain. Specifically, the field in the receive volume as the response to some source in the transmit volume can be expressed as a combination of plane waves arriving at the receive volume in different angles of arrival (AOA) due to a series of plane waves leaving the transmit volume in different angles of departure (AOD). When the scattering objects are distributed in complete randomness, the coefficients of all these plane wave components are uncorrelated pairwise. This extended assumption has been successfully applied in a recent work of the authors to develop a statistical propagation model between finite transmit and receive volumes [20].

APPENDIX
ALTERNATIVE FORM OF UNCORRELATED SCATTERING ASSUMPTION

It is proved here that the sufficient and necessary condition for the uncorrelated scattering assumption in (10) is (11). The necessity is shown first.

Necessity: By substituting (3) in the LHS of (10) and using the Fourier expansion of the Dirac delta function on the right-hand side (RHS), (10) becomes

$$\sum_{n=-\infty}^{\infty} \left[\left(\frac{1}{2\pi} \right)^2 \sum_{m=-\infty}^{\infty} \mathcal{E}\{\alpha_m \alpha_n^*\} e^{im(\theta-(\pi/2))} \right.$$
$$\left. \times e^{in(\pi/2)} \right] e^{-in\theta'} = \sum_{n=-\infty}^{\infty} \left[\frac{1}{2\pi} P(\theta) e^{in\theta} \right] e^{-in\theta'}. \quad (15)$$

Matching the Fourier coefficients on both sides and some simple manipulations will lead to

$$P(\theta) = \sum_{m=-\infty}^{\infty} \left[\frac{1}{2\pi} \mathcal{E}\{\alpha_m \alpha_n^*\} e^{-i(m-n)(\pi/2)} \right] e^{i(m-n)\theta} \quad (16)$$

which represents the power angular spectrum in a Fourier series. Using the standard way to calculate the Fourier coefficients, one arrives at the final form of (11)

$$\mathcal{E}\{\alpha_m \alpha_n^*\} = e^{i(m-n)(\pi/2)} \int_0^{2\pi} P(\theta) e^{-i(m-n)\theta} d\theta. \quad (17)$$

This completes the proof of necessity.

Sufficiency: The LHS of (10) can be represented as

$$\mathcal{E}\{a(\theta)a^*(\theta')\} = \left(\frac{1}{2\pi} \right)^2 \sum_{m=-\infty}^{\infty} \sum_{n=-\infty}^{\infty} \mathcal{E}\{\alpha_m \alpha_n^*\}$$
$$\times e^{im(\theta-(\pi/2))} e^{-in(\theta'-(\pi/2))}. \quad (18)$$

Substituting (17) into (18), one obtains

$$\mathcal{E}\{a(\theta)a^*(\theta')\} = \int_0^{2\pi} P(\theta_1) \left(\frac{1}{2\pi} \sum_{m=-\infty}^{\infty} e^{-im\theta_1} e^{im\theta} \right)$$
$$\times \left(\frac{1}{2\pi} \sum_{n=-\infty}^{\infty} e^{in\theta_1} e^{-in\theta'} \right) d\theta_1$$
$$= \int_0^{2\pi} P(\theta_1) \delta(\theta_1 - \theta) \delta(\theta_1 - \theta') d\theta_1$$
$$= P(\theta)\delta(\theta - \theta') \quad (19)$$

which is exactly (10). This completes the proof of sufficiency.

REFERENCES

[1] W. C. Jakes, *Microwave Mobile Communications*. Piscataway, NJ: IEEE, 1994.

[2] G. J. Foschini and M. J. Gans, "On limits of wireless communications in a fading enviroment when using multiple antennas," *IEEE J. Sel. Areas Commun.*, vol. 6, pp. 331–335, Mar. 1998.

[3] T. Betlehem and T. D. Abhayapala, "Spatial correlation for correlated scatterers," in *Proc. IEEE Int. Conf. Acoust., Speech, Signal Process. (ICASSP)*, Toulouse, France, May 2006.

[4] P. A. Bello, "Characterization of randomly time-variant linear channels," *IEEE Trans. Commun. Syst.*, vol. CS-11, pp. 360–393, Dec. 1963.

[5] J. D. Parsons, *The Mobile Radio Propagation Channel*. London, U.K.: Pentech, 1992.

[6] P. D. Teal, T. D. Abhayapala, and R. A. Kennedy, "Spatial correlation for general distributions of scatterers," *IEEE Signal Process. Lett.*, vol. 9, pp. 305–308, Oct. 2002.

[7] A. S. Y. Poon, R. W. Brodersen, and D. N. C. Tse, "Degrees of freedom in multiple-antenna channels: A signal space approach," *IEEE Trans. Inf. Theory*, vol. 51, pp. 523–536, Feb. 2005.

[8] R. A. Kennedy, P. S. Sadeghi, T. D. Abhayapala, and H. M. Jones, "Instrinsic limits of dimensionality and richness in random multipath fields," *IEEE Trans. Signal Process.*, vol. 55, pp. 2542–2556, Jun. 2007.

[9] D. Colton and R. Kress, *Integral Equation Methods in Scattering Theory*. New York: Wiley, 1983.

[10] F. Seydou, R. Duraiswami, and T. Seppänen, "A boundary element method for electromagnetic scattering by multiple cylinders," in *Proc. IEEE AP-S Int. Symp. Dig.*, Columbus, OH, Jun. 2003, vol. 3, pp. 516–519.

[11] R. V. Hippel, *Dielectric Materials and Applications*. Cambridge, MA: Mass. Inst. Technol. Press, 1954.

[12] V. Rokhlin, "Rapid solution of integral equations of scattering theory in two dimensions," *J. Comput. Phys.*, vol. 86, pp. 414–439, Feb. 1990.

[13] N. Engheta, W. D. Murphy, V. Rokhlin, and M. S. Vassiliou, "The fast multipole method (FMM) for electromagnetic scattering problems," *IEEE Trans. Antennas Propag.*, vol. 40, pp. 634–641, Jun. 1992.

[14] R. F. Harrington, *Time-Harmonic Electromagnetic Fields.* New York: McGraw-Hill, 1961.

[15] H. M. Jones, R. A. Kennedy, and T. D. Abhayapala, "On dimensionality of multipath fields: Spatial extent and richness," in *Proc. IEEE Int. Conf. Acoust., Speech Signal Process. (ICASSP)*, Orlando, FL, May 2002, pp. 2837–2840.

[16] , W. C. Chew, J. M. Jin, E. Michielssen, and J. M. Song, Eds., *Fast and Efficient Algorithms in Computational Electromagnetics.* Boston, MA: Artech House, 2000.

[17] O. M. Bucci and G. Franceschetti, "On the spatial bandwidth of scattered fields," *IEEE Trans. Antennas Propag.*, vol. 35, pp. 1445–1455, Dec. 1987.

[18] M. D. Migliore, "On the role of the number of degrees of freedom of the field in MIMO channels," *IEEE Trans. Antennas Propag.*, vol. 54, pp. 620–628, Feb. 2006.

[19] T. A. Lamahewa, T. D. Abhayapala, and R. A. Kennedy, "Space-time cross correlation and space-frequency cross spectrum in non-isotropic scattering environments," in *Proc. IEEE Int. Conf. Acoust., Speech Signal Process. (ICASSP)*, Toulouse, France, May 2006, vol. 4, pp. 609–612.

[20] J. Xu and R. Janaswamy, "A double-angular propagation model with cluster scattering," *IEEE Trans. Antennas Propag.*, vol. 57, pp. 1228–1240, Apr. 2009.

Jie Xu (S'05–M'08) He received the Ph.D. degree in electrical engineering in 2008 from the University of Massachusetts, Amherst, and the M.S. and B.S. degrees, both in electrical engineering, from Tianjin University, China, in 2003 and 2000, respectively.

Before he joined the University of Massachusetts during fall 2003, he worked as a software engineer with Zhongxing Telecommunications Equipment (ZTE) Corp., Shenzhen, China, for six months, where he took part in the design and implementation of the system software for IS-2000 CDMA cellular systems and was responsible for the radio frequency control part on the BS side. He is currently working as a Postdoctoral Research Fellow with the Massachusetts Biomedical Sensing and Signal Processing (BioSSP) Center in the UMass system and conducting research on cancer detections using microwave frequencies.

Ramakrishna Janaswamy (S'82–M'83–SM'93–F'03) received the Ph.D. degree in electrical engineering in 1986 from the University of Massachusetts, Amherst.

From August 1986 to May 1987, he was an Assistant Professor of electrical engineering at Wilkes University, Wilkes Barre, PA. From August 1987 to August 2001, he was on the faculty of the Department of Electrical and Computer Engineering, Naval Postgraduate School, Monterey, CA. In September 2001, he joined the Department of Electrical and Computer Engineering, University of Massachusetts, Amherst, where he is a currently a Professor. He is the author of the book *Radiowave Propagation and Smart Antennas for Wireless Communications* (Boston, MA: Kluwer Academic, November 2000) and a contributing author in the *Handbook of Antennas in Wireless Communications*, L. Godara, Ed., (Boca Raton, FL: CRC, August 2001) and the *Encyclopedia of RF and Microwave Engineering*, K. Chang, Ed., (New York: Wiley, 2005). His research interests include deterministic and stochastic radio wave propagation modeling, analytical and computational electromagnetics, antenna theory and design, and wireless communications.

Dr. Janaswamy was the recipient of the R. W. P. King Prize Paper Award of the IEEE TRANSACTIONS ON ANTENNAS AND PROPAGATION in 1995. For his services to the IEEE Monterey Bay Subsection, he received the IEEE 3rd Millennium Medal from the Santa Clara Valley Section in 2000. He is an elected member of the U.S. National Committee of International Union of Radio Science, Commissions B and F. He served as an Associate Editor of *Radio Science* from January 1999–January 2004 and as an Associate Editor of the IEEE TRANSACTIONS ON VEHICULAR TECHNOLOGY.

Modeling Radio Transmission Loss in Curved, Branched and Rough-Walled Tunnels With the ADI-PE Method

Richard Martelly, *Member, IEEE*, and Ramakrishna Janaswamy, *Fellow, IEEE*

Abstract—We discuss the use of the parabolic equation (PE) along with the alternate direction implicit (ADI) method in predicting the loss for three specialized tunnel cases: curved tunnels, branched tunnels, and rough-walled tunnels. This paper builds on previous work which discusses the use of the ADI-PE in modeling transmission loss in smooth, straight tunnels. For each specialized tunnel case, the ADI-PE formulation is presented along with necessary boundary conditions and tunnel geometry limitations. To complete the study, examples are presented where the ADI-PE numerical results for the curved and rough-walled tunnel are compared to known analytical models and experimental data, and the branched tunnel data is compared to the numerical solutions produced by HFSS.

Index Terms—Alternate direction implicit (ADI), parabolic equation, radiowave propagation, tunnels.

I. INTRODUCTION

THE alternate direction implicit (ADI) method coupled with the vector parabolic equation (PE) has previously been shown to model radiowave propagation in straight tunnels with smooth walls [1]. However, due to the rapid growth of telecommunication systems, different tunnel environments also need to be studied. Subway and underground road tunnels typically curve or branch out into side tunnels and have walls which are not smooth. These tunnel geometries are not always well described by analytical models and accurate numerical solutions become important. In real tunnels, it has been shown that, over a long distance, high order modes are heavily attenuated and low order modes dominate [3]. When tunnels are treated as imperfect waveguides, these fields represent waves which travel near the axis of propagation. The PE can accurately model low order modes for electrically large tunnels [1], [2]. The standard PE is an approximation of the Helmholtz equation that assumes fields travel within $\pm 15°$ to the axis of propagation. The PE lends itself to numerical discretization more easily than the Helmholtz equation but does not account for backscattered fields. Furthermore, the slow varying nature of low order modes implies the use of implicit finite difference (FDM) techniques where large discretizations along the axis of propagation are allowed.

The Crank-Nicolson method is an unconditionally stable implicit FDM that has been traditionally used to solve for the vector PE. However, the Crank-Nicolson method can also become computationally intensive when dealing with fine meshes or when a large number of propagation steps is required [1]. The alternate direction implicit (ADI) technique is a modification of the Crank-Nicolson method that reduces computational labor by solving for the fields one dimension at a time [1], [6]. The truncation error introduced by the ADI modification is of the same order as the error already introduced by the Crank-Nicolson method. Previous work has shown, for modest discretizations, the ADI and Crank-Nicolson solutions are nearly identical [1].

In this paper, we use the vector PE, following the formulation of Popov [2], to solve for fields in specialized tunnel environments. For each case, we briefly discuss the ADI formulation as well as the boundary conditions used to characterize the tunnel wall. In Section II we discuss the curving tunnel and compare the ADI-PE results to known analytical approximations and published experimental data [7]. In Section III, we study the branch tunnel and compare our ADI-PE numerical results to the numerical results obtained using HFSS [13] for a smaller sample problem. Finally, in Section IV, we formulate a model for tunnels with surface roughness and compare our ADI-PE results with known, experimentally verified, analytical solutions.

II. TUNNELS WITH SMOOTHLY CURVED AXIS

A. Curved Tunnel Propagation Model

Let us consider a tunnel with a curved axis. The geometry of a typical curved tunnel with a rectangular cross-section is shown in Fig. 1, where s is the curved axis, or range, and $\rho(s)$ is the range dependant radius of curvature. The vector PE was formulated by Popov and was shown to accurately model electromagnetic propagation in curved tunnels [2].

The vector PE for a tunnel with a smooth curve in the horizontal plane, as formulated in [2], (with $e^{j\omega t}$ time dependence, where ω is frequency and t is time) is

$$2k_o j \frac{\partial \overline{W}}{\partial s} = \frac{\partial^2 \overline{W}}{\partial x^2} + \frac{\partial^2 \overline{W}}{\partial y^2} - 2k_o^2 \frac{x}{\rho(s)} \overline{W} \qquad (1)$$
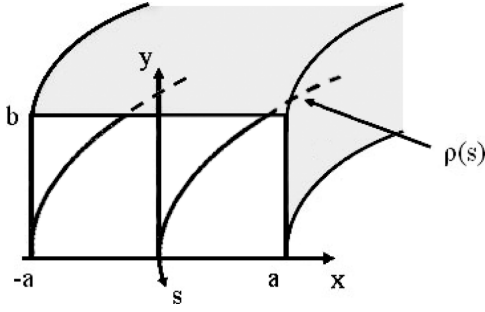
Fig. 1.   A typical tunnel with a curved axis.

where k_o is the free space wave number, and $\overline{W}$ is a vector function that is directly related to the transverse electric field. The relationship of $\overline{W}$ to the transverse electric field is given by

$$\overline{W} = (E_x, E_y)^T e^{jk_o s}. \qquad (2)$$

where E_x and E_y are the x and y components of the electric field, respectively. The vector PE is formulated using asymptotic analysis, where it is assumed that $\lambda/b \ll 1$ and $b/\rho(s) \ll 1$ (where λ is the wavelength), which means it is only valid for high frequency propagation and in tunnels with smooth axis of curvature.

Along the tunnel wall, the impedance boundary condition is enforced and the transverse fields become coupled, as shown by (3):

$$\overline{W} = \frac{j}{k_o} \begin{pmatrix} n_x & n_y \\ n_y & -n_x \end{pmatrix} \begin{pmatrix} \frac{1}{Z_s} & 0 \\ 0 & Z_s \end{pmatrix} \begin{pmatrix} n_x & n_y \\ n_y & -n_x \end{pmatrix} \frac{\partial \overline{W}}{\partial n} \quad (3)$$

where n_x and n_y are the x and y components of the unit normal vector at the boundary and Z_s is the normalized surface impedance [2]. For a wall with relative permittivity ϵ_r and conductivity σ_o (in S/m), we use the grazing angle approximation for surface impedance [1], [5]

$$Z_s = \frac{\sqrt{\epsilon_{rc} - 1}}{\epsilon_{rc}} \qquad (4)$$

where $\epsilon_{rc} = \epsilon_r - j\sigma_r$, and $\sigma_r = \sigma_o/\omega\epsilon_o$, is the complex permittivity and relative conductivity, respectively. The discretizations along the x, y and s axes are represented by Δx, Δy, and Δs, respectively.

A Peaceman-Rachford [6] ADI formulation of (1) can be summarized by

$$\left(1 + \frac{j\Delta s \delta_x}{4k_o \Delta x^2 A_m^n}\right)\overline{W}_{m,l}^{n+1/2}$$
$$= \left(1 - \frac{j\Delta s \delta_y}{4k_o \Delta y^2 B_m^n}\right)\overline{W}_{m,l}^n \qquad (5)$$

$$A_m^n \left(1 + \frac{j\Delta s \delta_y}{4k_o \Delta y^2 A_m^n}\right)\overline{W}_{m,l}^{n+1}$$
$$= B_m^n \left(1 - \frac{j\Delta s \delta_x}{4k_o \Delta x^2 B_m^n}\right)\overline{W}_{m,l}^{n+1/2} \qquad (6)$$

where $x = m\Delta x$, $y = l\Delta y$ and $s = s^n = n\Delta s$. The difference quotients are $\delta_x W_{m,l} = W_{m+1,l} - 2W_{m,l} + W_{m-1,l}$ and $\delta_y W_{m,l} = W_{m,l+1} - 2W_{m,l} + W_{m,l-1}$ and

$$A_m^n = \left(1 - \frac{jm\Delta x k_o \Delta s}{2\rho(s^n)}\right) \qquad (7)$$

$$B_m^n = \left(1 + \frac{jm\Delta x k_o \Delta s}{2\rho(s^n)}\right). \qquad (8)$$

Note that when $\rho(s) \to \infty$, A_m^n and B_m^n become unity and (5) and (6) reduces to the ADI formulation for the straight axis PE shown in [1, equations (22) and (23)]. The ADI equations in (5), (6) represents a marching technique where the transverse electric field is solved step by step within the tunnel domain [2]. Starting with the known initial field at the $n = 0$ plane, the fields of each successive plane is solved in consecutive order, at propagation steps of Δs, until the field at the desired range is solved.

B. Curved Tunnel Field Approximations

Approximate analytical solutions describing fields in curved tunnels with rectangular cross sections and constant curvature radii are well known and discussed in [3], [8]. At high frequency, $k_o a \gg 1$, and for large radii of curvature, $\rho \gg a$, the fields are best described in terms of Airy functions [3], [8]. As shown in (3), the n_x and n_y components of the normal vector vanishes alternatively on the vertical and horizontal walls in tunnels with rectangular cross sections. As a result, the components of the vector function $\overline{W}$ become decoupled and can be solved independently. The horizontal and vertical polarizations can now be solved separately by enforcing the decoupled impedance boundary conditions on all four walls. Following the derivation shown in [2], the vertical component, V, of the vector function is shown to be (keeping the same notation as [2]):

$$V(x, y, s) = \Omega(x)\Xi(y)e^{P_{22}s} \qquad (9)$$
$$\Omega(x) = C_1 Ai(t) + C_2 Bi(t) \qquad (10)$$
$$\Xi(y) = D_1 Ai(x_o) + D_2 Bi(x_o) \qquad (11)$$

where Ai and Bi are the Airy functions of the first and second kind, P_{22} is the propagation constant, $t = t_o + \left(2k_o^2/\rho\right)^{1/2} x$, t_o and x_o are constant eigenvalues to be found from the boundary conditions, given by

$$\left[V \pm \frac{Z_s}{jk_o}\frac{\partial V}{\partial x}\right]_{x=\pm a} = 0, \quad \left[V \mp \frac{1}{jk_o Z_s}\frac{\partial V}{\partial y}\right]_{y=0,b} = 0. \qquad (12)$$

For large curvature radii, the vertically polarized fields are

$$\Omega(x) \approx \sin\left[\frac{m\pi}{2}\left(1 - \frac{x}{a}\right)\right], \quad m = 1, 2, 3\ldots \qquad (13)$$

$$\Xi(y) \approx \sin\frac{n\pi y}{b}, \quad n = 1, 2, 3\ldots \qquad (14)$$

where the integers m and n physically represent field variations along the x and y axes and specifies a possible mode. The mode

TABLE I
ANALYTICAL AND NUMERICAL MAFs FOR THE CURVED TUNNEL WITH
RECTANGULAR CROSS SECTION FOR 950 MHz

f = 950 MHz		
ρ (m)	Analytical (dB/km)	ADI (dB/km)
∞	16.2	16.0
2533	17.3	18.1
1267	18.8	18.5
844	20.3	19.8
633	21.7	20.8
507	23.2	22.0

TABLE II
ANALYTICAL AND NUMERICAL MAFs FOR THE CURVED TUNNEL WITH
RECTANGULAR CROSS SECTION FOR 1.8 GHz

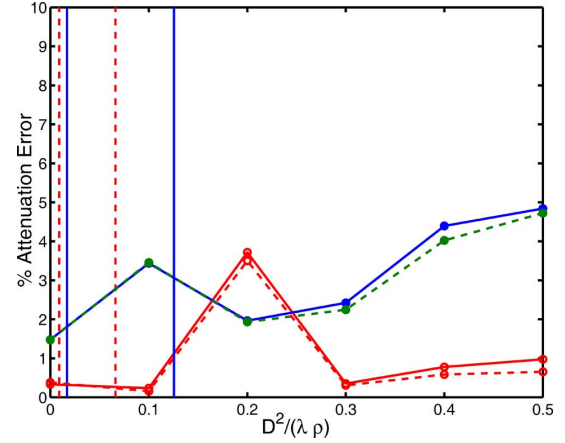| f = 1.8 GHz		
ρ (m)	Analytical (dB/km)	ADI (dB/km)
∞	4.5	4.5
4800	5.2	5.2
2400	6.0	6.2
1600	6.7	6.7
1200	7.5	7.5
960	8.2	8.2

Fig. 2. Percent error of the MAFs of the curved waveguide for 950 MHz (dot, solid) and 1.8 GHz (circle, solid) for $\Delta s = 3.75 \ \lambda$. The percent error of the MAFs for 950 MHz (dot,dashed) and 1.8 GHz (circle, dashed) for $\Delta s = 1.875 \ \lambda$. The vertical lines show the region where $t_o^+ = \pm 1$ for 950 MHz (solid) and 1.8 GHz (dashed).

attenuation per unit length can be found from the complex exponent, P_{22}, to be [2]

$$\alpha_z \left[\frac{\text{dB}}{\text{km}}\right] \approx 4343\lambda^2 Re\left(\frac{1}{Z_s}\right) + 4343\lambda^2 Re\left(Z_s\right)$$
$$\cdot \begin{cases} \frac{2}{\lambda^2 \rho} & t_o^+ \gg 1 \\ \left[\frac{m^2}{(2a)^3} + \frac{8(2a)^3(15-m^2\pi^2)}{3\pi^2(m\lambda)^4\rho^2}\right] & t_o^+ \ll -1 \end{cases} \quad (15)$$

where

$$t_o^+ \approx -\left(\frac{\pi m}{2q}\right)^2 + 5\left(\frac{q}{\pi m}\right)^4 - \frac{1}{3}\frac{q^4}{\pi^2 m^2}, \quad m = 1, 2, 3\dots$$
$$(16)$$

and $q = \left(2k_o^2/(\rho+a)\right)^{1/3} a$. The $t_o^+ \gg 1$ part of (15) describes small radii of curvature and the $t_o^+ \ll -1$ part describes large radii of curvature (or almost straight tunnels). Mahmoud and Wait [9] numerically calculated the attenuation factors for curved waveguides using more precise transcendental equations. As shown in [2, Fig. 3], the aysmptotic equation (15) is in very good agreement with Mahmoud and Wait's numerical solutions. We will use the aysmptotic equation to validate the numerical simulations of the ADI-PE.

C. Comparison of the ADI-PE to Analytical Solutions

In this sub-section, we validate the ADI-PE with numerical examples. We consider a rectangular tunnel with dimensions of 8 m × 4 m and walls with relative dielectric constant, $\epsilon_r = 5.5$, and conductivity, $\sigma_o = 0.01$ S/m. We used the dominant $m = 1, n = 1$, mode of the vertically polarized field, as shown by (13) and (14), as our initial field. The discretizations used for the 950 MHz case were $\Delta s = 3.73 \ \lambda$, $\Delta x = 0.84 \ \lambda$ and $\Delta y = 0.70 \ \lambda$; and the discretizations used for the 1.8 GHz simulations were $\Delta s = 3.75 \ \lambda$, $\Delta x = 0.80 \ \lambda$ and $\Delta y = 0.71 \ \lambda$.

The mode attenuations per unit length, or mode attenuation factors (MAFs), from (15) and the ADI-PE simulations are tabulated in Tables I and II for different curvature radii.

As shown in Tables I and II, the numerical MAFs closely follow the aysmptotic solutions over the range of curvature radii. Furthermore, as the curvature radii decreases, the number of reflections from the walls along the curved path increases and so does the loss. The percent error, defined by

$$\%\text{Attenuation Error} = \frac{\left|MAF_{ADI} - \alpha_z\left(\frac{\text{dB}}{\text{km}}\right)\right|}{\left|\alpha_z\left(\frac{\text{dB}}{\text{km}}\right)\right|} \quad (17)$$

is shown in Fig. 2 as a function of $D^2/\lambda\rho$, (where D is the length of the diagonal of the rectangular cross section) for 950 MHz (dot, solid) and 1.8 GHz (circle, solid). The figure also shows the results for smaller discretizations ($\Delta s = 1.875 \ \lambda$) with dashed curves to show that the solutions are convergent. The vertical lines in Fig. 2 show the region where $t_o^+ = \pm 1$ for the 950 MHz (solid) and 1.8 GHz (dashed) cases, respectively. The parameter, $D^2/\lambda\rho$, was selected from [2] because it is a wavelength dependent term that must be much less than unity to ensure accurate results. Furthermore, $D^2/\lambda\rho$, is the Fresnel number and is one of the parameters which govern the diffraction processes in the waveguide [2]. As Fig. 2 shows, there is less than 5% error in MAFs over the entire range of ρ considered; even when there are sharp bends and the condition, $D^2/\lambda\rho \ll 1$, is not satisfied. Finally, one of the important characteristics of the curved tunnel is the accumulation of the field near the concave wall at $y = -a$ (the whispering gallery mode). Fig. 3(a) shows the dominant $|V_{1,1}|$ field as defined by (13) and (14) across the initial $s = 0$ plane at 1.8 GHz. The whispering gallery mode feature can be seen in Fig. 3(b), where the field generated by the ADI-PE, at a range of 2000 m for $\rho = 2000$ m, has an accumulation along the $x = -4$ m wall.

D. Comparison of the ADI-PE to Ray Tracing Simulations

In this section, we compare the ADI-PE simulations to the ray tracing simulations shown in Wang *et al.* for a curved waveguide [7]. The geometry of the waveguide (top view) is shown in Fig. 4 and is comprised of two straight sections and a curved section.
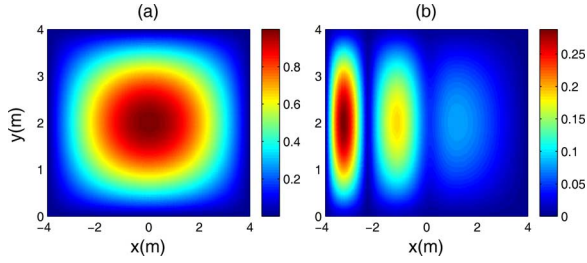
Fig. 3. The $|V_{11}|$ mode at (a) $s = 0$ m and at (b) $s = 2000$ m for $\rho = 2000$ m at 1.8 GHz.
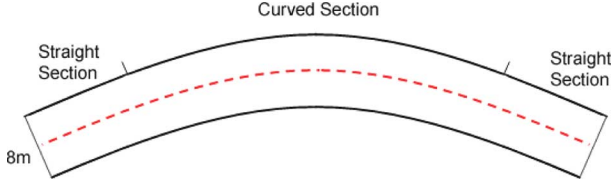

Fig. 4. Geometry of the curved tunnel with straight sections.

The axial length of the waveguide is 400 m and the length of the curved section is 200 m with a radius of curvature of 300 m. The cross-sectional dimensions of the waveguide are 8 m $\times$ 6 m. In [7], the transmitter and receivers are vertically polarized half-wave dipoles operating at a frequency of 1 GHz. The transmitter and receivers are located at the center of the waveguide at heights of 3 and 1.5 m.

To establish a basis of comparison, we first look at the straight waveguide. Fig. 5 shows the normalized received power of the ray tracing simulations (solid) and the ADI-PE simulations (dashed). The ADI-PE is simulated using the far field expressions of a half-wave dipole in free space placed 30 m outside the entrance as the initial field. The field is tapered by a unit Gaussian with standard deviation, $\sigma = 2.5 \lambda$ to minimize error associated with using incorrect field values at the walls [1]. The dielectric constant and conductivity of the waveguide walls are taken to be the typical values of 5 and 0.01 S/m, respectively. Simulations show that over the range of acceptable values of dielectric constants ($\epsilon_r = 5 - 12$), there is little change in the received power. The simulations are done with discretizations of $\Delta x = 0.67 \lambda$, $\Delta y = 0.74 \lambda$ and $\Delta s = 1.33 \lambda$. As the figure shows, the ADI-PE closely models the nulls in the received power generated from ray tracing simulations. The ADI-PE results are vertically offset so that the least squares fit line of the ADI-PE data and the experimental data (in the curved region) intersect at the start of the curved region (at 100 m).

As discussed in [1] and [3], propagation in straight tunnels can be characterized by a near and far zone. In the near zone, rays propagating at large angles make significant contributions to the field and take the form of rapid oscillations. In the far zone, these rays are severely attenuated and paraxial rays are dominant. In the near zone, the PE is not accurate, but so long as the low order modes are illuminated, the PE will be accurate in the far zone. The start of the far zone is determined by the size, shape and frequency of the tunnel [3]. The far zone can be found by calculating the attenuation constant of each mode. However, the attenuation constant and amplification term for each mode may not always be found analytically. If we summed
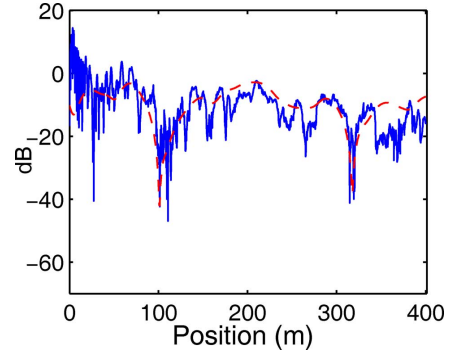

Fig. 5. Normalized received power from ray tracing (solid) and ADI-PE (dashed) along the axis of propagation for the straight tunnel.
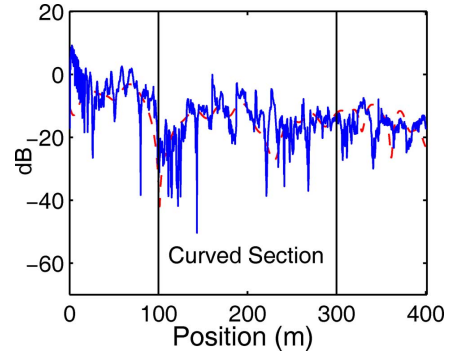

Fig. 6. Normalized received power from ray tracing (solid) and ADI-PE (dashed) along the axis of propagation for the curved tunnel.

the equally weighted first 100 modes for the rectangular waveguides using the propagation constant expressions defined by [3, Eqs. (54) and (55)], we can see that the region before 500 m is in the near zone. In the range considered here, the contributions of the high order modes account for the discrepancies in the ADI-PE and ray tracing results. These discrepancies are in the form of rapid oscillations in the experimental data along the axis of propagation. Fig. 6 shows the normalized received power for the curved waveguide. As shown in the figure, the ADI-PE closely tracks the received power of the ray tracing simulations within the curved section.

E. Comparison of the ADI-PE to Experimental Data

In this section, we compare the ADI-PE to experimental data for the Lin-sen subway tunnel, shown in [7, Fig. 6]. The Lin-sen subway is comprised of two curved sections with radii of curvature of 455.68 m and 354.74 m, respectively, separated by a straight section. The straight entrance and exit sections are not considered here because they do not lie within the same horizontal plane as the rest of the tunnel. The tunnel cross-section is approximately rectangular with dimensions of 6 m $\times$ 8 m. The transmitter is located outside the tunnel and is a vertically polarized Yagi-Uda antenna operating at 942 MHz. The receiver is placed off center at a height of 1.85 m above the ground.

Fig. 7 shows the received power from measurements (solid) and the ADI-PE simulations. As before, the dielectric constant and conductivity are assumed to be the typical values of 5 and 0.01 S/m. In this case, the field entering the horizontal section of the subway is unknown and represents a possible source of error.
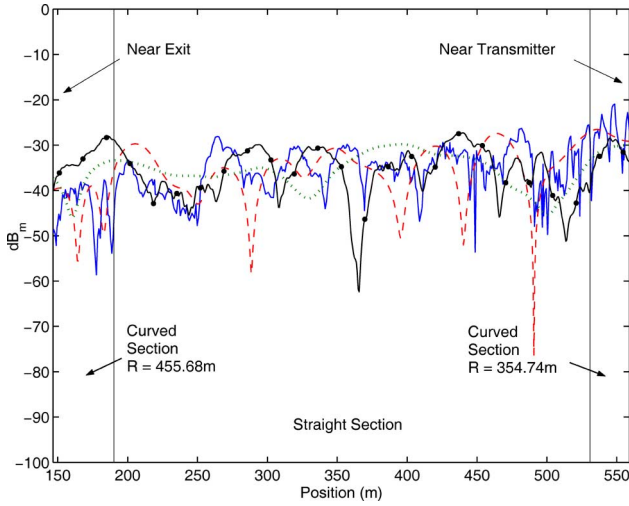
Fig. 7. Experimental data (solid) and ADI results with the HE_{21} (long-dashed), HE_{11} (short-dashed) mode and the half wave dipole (dot-solid) as the initial field for the Lin-sen subway tunnel.

However, we may choose a low order mode as our initial field because, at large distances, only low order modes dominate [1]. Simulations done for various initial fields show that the $m = 2, n = 1$ mode of the field (long-dashed), as defined by (13) and (14), produces solutions that best fits the experimental data. The discretizations are $\Delta x = \Delta y = 0.72\ \lambda$, and $\Delta z = 2.11\ \lambda$. As Fig. 7 shows for this initial field, even with our limitations, there is still good agreement between the ADI-PE solutions and the measured results. The ADI-PE models the nulls and overall trend of the received power. The figure also shows the field intensity when the $m = 1, n = 1$ mode (short-dashed) and the far field expressions for the half-wave dipole (dot-line) are used as initial field. What this shows is that the field intensity is very sensitive to the initial field. This is because we are dealing with a short curved section (approximately 50 m), and high order modes make significant contributions in to the straight section. As in the previous example, we are not operating in the far zone and high order modes make significant contributions. The high order modes are represented by the rapid fluctuations in the measured data. The PE approximation does not accurately model these modes and it is a source of error. These results were obtained in a matter of minutes using a typical PC (1 GB RAM). By comparison, a typical ray tracing code would require another simulator to generate the initial field and must track each reflection and diffraction for each ray and can become computationally intensive.

III. BRANCH TUNNELS

A. Branch Tunnel Model

Let us now consider the case of a straight tunnel that branches into a side tunnel. A typical branch tunnel geometry is shown in Fig. 8(a) and (b), where the main tunnel axis is shown as a solid bold line and the branch tunnel axis is shown as a long dashed line. The branch angle, θ_b, is the angle between the axes of the straight and branch tunnels. Fig. 8(a) and (b) show the incident and reflected rays as it enters the branch. The short dashed line marks the input plane of the branch tunnel. The grazing
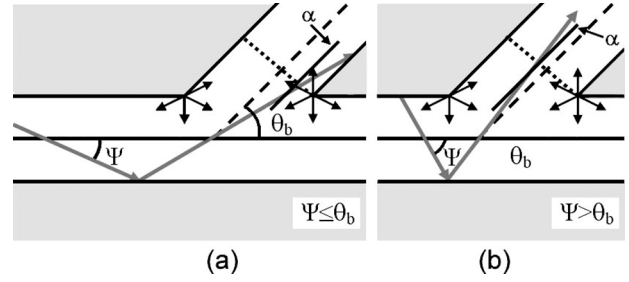

Fig. 8. The incident and reflected rays entering the branch tunnel when (a) $\Psi \leq \theta_b$ and (b) $\Psi > \theta_b$.

angle, Ψ, and the angle of the ray entering the branch, α, are also shown. In order for the PE approximation to be valid, the branch angle must be small enough. More precisely, the branch angle must be less than $30°$ to ensure reflected rays entering the branch are within our PE limit of $\pm 15°$. Also, considering the rays diffracted from the corners of the junction, we can arrive at a much more stringent requirement of $\theta_b < 15°$. Diffracted rays entering the main tunnel at angles greater than $15°$ will be weak when compared to reflected rays and will experience severe attenuation after the tunnel junction.

As in the previous section, we solve the vector PE shown in (1) with $\rho(s) \to \infty$. The slope of the branching wall is modeled using a staircase approximation (see Fig. 9(a)) and the impedance boundary condition is enforced on all four walls as outlined in [1] and [2]. The fields along the planes marking the entrance of the main tunnel (line C) and the branch tunnel (line B) are solved simultaneously and then used as the initial fields for the two separate diverging tunnels.

B. Comparison of ADI-PE Results to HFSS Simulations

In this section we validate the ADI-PE branch model with a numerical example. We simulate a 0.9 m × 1.0 m rectangular tunnel with a branch angle of $15°$ and operating at a frequency of 900 MHz. The initial field is a unit strength Gaussian field source in the far zone. The source, with standard deviation of $0.75\ \lambda$, is centered 5 m before the tunnel junction (only the region near the tunnel junction is shown in Fig. 9). This means we are only using the lowest order modes as our initial field [1], [3]. The fundamental mode propagates near our PE limit at an angle of $14°$ with respect to the axis of the main branch.

The ADI-PE simulations are done with discretizations (within the tunnel junction) of $\Delta x = 0.15\ \lambda$, $\Delta y = 0.14\ \lambda$ and $\Delta z = 0.13\ \lambda$. The cross-sectional coordinates are indicated by x and y, while the axial coordinate in the main tunnel is denoted by the z-axis. The z-axis discretizations are made small within the tunnel junction to ensure small step sizes for the staircase approximation. Outside the junction region, discretizations along the axis of propagation can be made as large as a few wavelengths [1]. To validate our results, we compare our solutions with HFSS [13] and plot the magnitude of the E_y field along the main and branch tunnel axes in Fig. 9(b). The HFSS simulations use radiation boundary conditions to terminate the tunnel and symmetry planes to reduce computational labor. HFSS is a full wave simulator and, unlike the ADI-PE, solves for backscattered waves as well as waves traveling in the
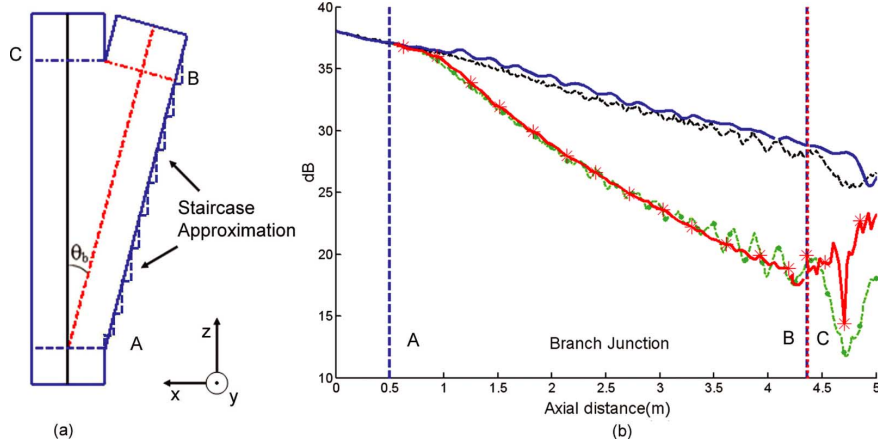
Fig. 9. (a) Geometry of the branch tunnel. (b) The axial field intensity of the main tunnel from ADI-PE (solid), HFSS (dashed), the branch tunnel from ADI-PE (asterisk) and HFSS (dashed).

forward direction. The backscattering is seen as fluctuations in the axial field in Fig. 9(b) near the diverging tunnels. The dielectric constant and conductivity of the tunnel walls is 5 and 0.1 S/m, respectively. A high conductivity is chosen so there is appreciable loss in the small tunnel dimensions allowed in HFSS. As we can see from Fig. 9(b), there is strong agreement in the axial field intensity along the main and branch tunnel axes between the ADI-PE and HFSS. The figure also shows there is about a 10 dB drop when going from the main to the branch tunnel (at the point marked C in Fig. 9(b)). Although the ADI-PE is used to simulate a tunnel with a relatively small electrical cross-section ($2.7 \ \lambda \times 3 \ \lambda$), it is capable of handling larger tunnels at higher frequencies without running into memory problems on an average (2 GB RAM) PC [1].

IV. ROUGH-WALLED TUNNELS

A. Rough-Walled Tunnel Model

So far we considered only tunnels with smooth walls, but in this section we investigate the effects of surface roughness. Surface roughness is the local variation of the tunnel wall relative to a mean surface level [4], [5]. In this study we consider random surface deviations in an otherwise smooth wall. For the purpose of numerical computations we assume the random deviations to be Gauassian distributed. A Gaussian distribution of the surface level can be characterized by a root-mean-square height deviation σ_h and correlation length, l [4], [5]. Smooth tunnels have a typical RMS height deviation of 0.01 m and rough surfaces, such as those found in coal mine tunnels, have a RMS height deviation of 0.1 m [4]. The excess loss of the E_x field due to roughness in a rectangular tunnel is given by (18)[4]

$$L_{\text{rough}} = 4.343\pi^2\sigma_h^2\lambda^2\left(\frac{1}{d_1^4} + \frac{1}{d_2^4}\right)z \quad \text{(dB)} \qquad (18)$$

where d_1 and d_2 are the tunnel dimensions in the x and y axes, respectively, and z is the range. The excess loss is derived by treating the rough surface as a random process and from ray tracing techniques, as outlined in [10] and [4]. Equation (18) is

shown in [4] to agree with experimental data taken for coal mine tunnels for frequencies ranging from $200 - 1000$ MHz.

In our model, we treat small scale roughness by replacing the rough surface with a flat impedance surface that produces an equivalent specular reflection coefficient. The equivalent impedance for horizontal and vertical polarization is shown in (19) and (20), [5]

$$Z_{eq}^H = \begin{cases} Z_s - j(k_o\sigma_h)^2\frac{\sqrt{\pi}}{2k_o l}, & k_o l \ll 1 \\ Z_s + (k_o\sigma_h)^2\sin\Psi, & k_o l \gg 1, \Psi \gg \frac{1}{\sqrt{k_o l}} \\ Z_s + (k_o\sigma_h)^2\Gamma\left(\frac{3}{4}\right)\sqrt{\frac{-2j}{\pi k_o l}}, & k_o l \gg 1, \Psi \ll \frac{1}{\sqrt{k_o l}} \end{cases}$$

$$(19)$$

$$Z_{eq}^V = \begin{cases} Z_s - j(k_o\sigma_h)^2\frac{\sqrt{\pi}\sin 2\Psi}{2k_o l}, & k_o l \ll 1 \\ Z_s + (k_o\sigma_h)^2\sin^3\Psi, & k_o l \gg 1, \Psi \gg \frac{1}{\sqrt{k_o l}} \\ Z_s + (k_o\sigma_h)^2\Gamma\left(\frac{1}{4}\right)\sqrt{\frac{-j}{8\pi(k_o l)^3}}, & k_o l \gg 1, \Psi \ll \frac{1}{\sqrt{k_o l}} \end{cases}$$

$$(20)$$

where Z_s is the surface impedance of the smooth wall, $\Gamma(\cdot)$ is the Gamma function, and Ψ is the grazing angle. When taking into account the effects of roughness, we substitute the surface impedance in (3) with the equivalent impedance of either (19) or (20).

Due to the PE angle limitation of $\pm 15°$, the maximum slope angle θ of the rough surface and the grazing angle must satisfy the following relationship

$$2\theta + \Psi \leq 15° \qquad (21)$$

where Ψ is defined as shown in Fig. 10. As we can see from Fig. 10, the angle of the specular reflection of the incident ray, denoted by ξ, depends on the height deviation of the roughness. The roughness angle is related to the RMS height and correlation length by
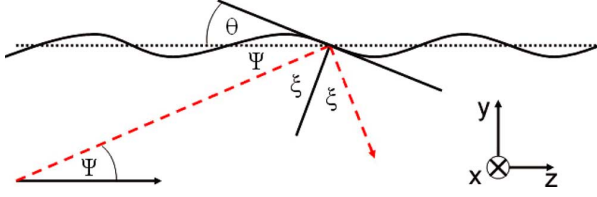
$$\tan\theta = \frac{\sigma_h}{l}. \qquad (22)$$

Fig. 10. The geometry of the rough surface.

TABLE III
ANALYTICAL AND NUMERICAL MAFs FOR THE RECTANGULAR TUNNEL

	Rectangular Tunnel (dB/km) 4.26 m × 2.10 m	
	Analytical	ADI-PE
w/o Roughness	31.0	29.8
Roughness	38.0	36.1
Excess Loss	7.0	6.3

TABLE IV
ANALYTICAL AND NUMERICAL MAFs FOR THE CIRCULAR TUNNEL

	Circular Tunnel (dB/km) Radius = 2.0 m	
	Analytical	ADI-PE
w/o Roughness	11.0	10.1
Roughness	27.0	26.1
Excess Loss	16.0	16.0

B. Comparison of Numerical and Analytical Solutions

We consider a rectangular 4.26 m × 2.10 m tunnel and a circular tunnel with radius of 2 m. The fundamental EH_{11}^x mode is used as the initial field of the rectangular tunnel and the fundamental TE_{01} mode generated by a loop ring excitation is used as the initial field for the circular tunnel. Both tunnels operate at a frequency of 1 GHz and the dielectric constant and conductivity of the tunnel walls are taken to be 12 and 0.02 S/m, respectively.

Tables III and IV summarize the mode attenuation factors (MAFs), or the loss in dB/km, of the smooth and rough tunnels with rectangular and circular cross-sections, respectively. In real tunnels, as in our simulations, the lowest order mode will determine the MAF over a long distance. We used (18) as our analytical loss factor for both the rectangular and circular tunnel. As we can see from (18), the loss due to roughness is a function of wavelength. To notice an appreciable loss at 1 GHz, we assume the walls are as rough as cave walls. Therefore, the RMS height is 0.1 m (0.33 λ) and correlation length is 2.5 m (8.33 λ) for both tunnels.

The grazing angle of the fundamental mode of the rectangular and circular tunnels is computed using the analytical expressions for the propagation constant, β (where $e^{-j\beta z}$ represents propagation in the positive z direction), outlined in [4] and [3]. The grazing angle is obtained from plane wave theory by [12]

$$\cos \Psi = \frac{Re(\beta)}{k_o} \qquad (23)$$

and is found to be 4.56° and 5.25° for the rectangular and circular tunnel, respectively. The roughness angle is found to be 2.29° from (22), and (21) is satisfied. The ADI is simulated using discretizations of $\Delta x = 0.284\,\lambda$, $\Delta y = 0.14\,\lambda$ and
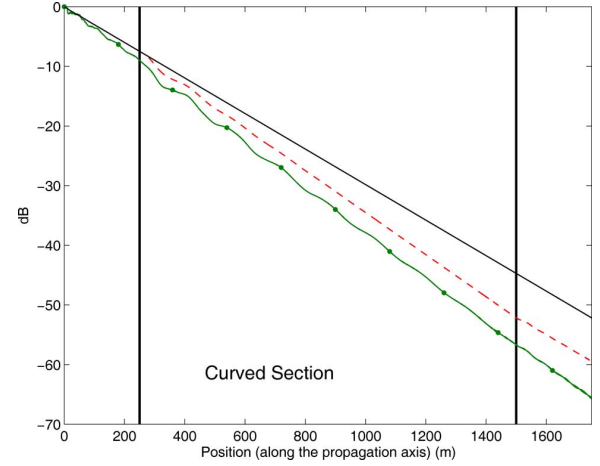

Fig. 11. The field intensity for the straight tunnel without roughness (solid), for the straight-curved-straight case (dashed), and for the straight-curved-straight case with roughness (dot-line).

$\Delta z = 4\,\lambda$ for the rectangular tunnel and $\Delta x = \Delta y = 0.44\,\lambda$ and $\Delta z = 1.67\,\lambda$ for the circular tunnel. As we can see from Table III, the excess loss due to roughness for the rectangular tunnel is about 7 dB when using either (18) and 6.3 dB when using ADI-PE. Simulations using a unit strength Gaussian initial field (where multiple modes are allowed) with $\sigma_x = \sigma_y = 2.5\,\lambda$ and $\sigma_x = \sigma_y = 1\,\lambda$ show much less than 1% difference in MAF. Table IV shows the same close agreement in numerical and theoretical excess loss for the tunnel with circular cross-section. In this case, the excess loss due to roughness is about 16 dB. The accuracy of the results suggests that the equivalent surface impedance, along with ADI-PE, is an adequate model for determining loss due to surface roughness. For completeness, we look at the case of the curved tunnel with roughness. Fig. 11 shows the E_x field intensity for the rectangular tunnel for the straight smooth case (solid), the curved smooth case (dashed) and the curved case with roughness (dot-line) with a radius of curvature of 1800 m. The curved section is in between two straight sections marked off by two vertical lines. The MAF of the curved section with roughness is about 37.7 dB/km. Tunnels with this type of configuration represents a topic of possible future work.

C. Comparison of the ADI-PE to Experimental Data

In this section, we examine a real underground tunnel with rough walls and a curving axis. The tunnel is approximately 3 m × 3 m and the walls are characterized by $\epsilon_r = 5.9$, $\sigma = 0.21$ S/m and with side wall roughness of $\sigma_h = 9.54$ cm [11]. The transmitter is placed at the entrance 1.71 m above the ground and the receivers are 2.73 m above the ground and operate at a frequency of 2.4 GHz. The data was recorded at every meter along the length of the tunnel. The curvature of the tunnel axis is shown in the boxed region in Fig. 12. The experimental data, shown as the solid line, was provided by the research team of Moutairou *et al.* [11].

The numerical simulations were done by computing the radii of curvature as a function of the tunnel axis and applying roughness for the side walls. A unit strength Gaussian with $\sigma_x = \sigma_y =$
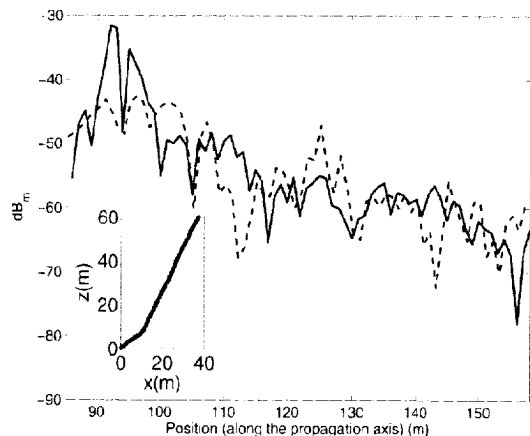
Fig. 12. The experimental axial field intensity of the rough-curved tunnel (solid), the ADI-PE simulations (dashed). (Boxed) The axial geometry of the rough-curved tunnel.

2.5 λ is used as the initial field. The correlation length was selected to be 0.5 m in order to avoid a steep slope in the wall irregularities. The discretizations are taken to be $\Delta x = 0.6\ \lambda$, $\Delta y = 0.69\ \lambda$. The equivalent impedance represents averaged values within one correlation length, so Δs is chosen to be 2 λ (0.25 m) (not much smaller than the correlation length). The ADI-PE results, shown as the dashed line, are shown in Fig. 12. In the simulations, a long straight section (85 m) precedes the tunnel in order to minimize the presence of higher order modes in the ADI-PE model. A sliding average with a window of 1 meter was used to match the resolution of the experimental data. As in previous cases, the overall trend is captured after the near zone region.

V. CONCLUSION

The ADI-PE method is used to investigate radiowave propagation in three specialized tunnel environments: curving tunnels, branch tunnels and rough-walled tunnels. We compared ADI-PE numerical examples to analytical and experimental data or to numerical data provided by HFSS. For the curved tunnel, there is good agreement between the ADI-PE and known analytical solutions for a wide range of curvature radii. For branch tunnels, even at the PE limit, there is good agreement between the ADI-PE and with commerical simulation codes such as HFSS. Also, the excess loss created by rough walls is accurately modeled using equivalent impedances. The ADI-PE method compares well with known theoretical loss factors for tunnels with either rectangular or circular cross-sections.

For each case, the ADI-PE method accurately models propagation in the tunnel environment, but only when there are limitations in the tunnel geometry. For curved tunnels, the curves must be smooth and propagation step sizes of 2 – 3 λ is adequate for accurate results. For the branch tunnels, the branch angle must be less than 15° to ensure accurate results. Within the tunnel junction, where the staircase approximation is used, propagation step sizes of less than 1 λ is recommended for accurate results. In rough tunnels, the maximum RMS height deviations and correlation lengths of the rough walls are limited.

The limitations are dependent on the grazing angle as well as on the ratio of the RMS height to the correlation length. In this case, simulation data suggests propagation step sizes of about 1.5 – 4 λ. As shown in previous work, the discretizations along the x and y axes must be less than 1.9 λ to satisfy Nyquist's theorem [1]. However, for the cases considered here, good results were obtained for discretizations less than 1 λ for the curved and rough-walled tunnels and less than 0.5 λ for the branch tunnel.

ACKNOWLEDGMENT

REFERENCES

[1] R. Martelly and R. Janaswamy, "An ADI-PE approach for modeling radio transmission loss in tunnels," IEEE Trans. Antennas Propag., vol. 57, pp. 1759–1770, Jun. 2009.
[2] A. V. Popov and N. Y. Zhu, "Modeling radio wave propagation in tunnels with a vectorial parabolic equation," IEEE Trans. Antennas Propag., vol. 48, pp. 1403–1412, Sep. 2000.
[3] D. G. Dudley, M. Lienard, S. F. Mahmoud, and P. Degauque, "Wireless propagation in tunnels," IEEE Antennas Propag. Mag., vol. 49, no. 2, pp. 11–26, Apr. 2007.
[4] A. G. Emslie, R. L. Lagace, and P. F. Strong, "Theory of the propagation of UHF radio waves in coal mine tunnels," IEEE Trans. Antennas Propag., vol. AP-23, pp. 192–205, Mar. 1975.
[5] R. Janaswamy, Radiowave Propagation and Smart Antennas for Wireless Communications. New York: Springer, 2000, pp. 26–31.
[6] J. C. Strikwerda, Finite Difference Schemes and Partial Differential Equations, 2nd ed. Philadelphia, PA: SIAM, 2004.
[7] T. Wang, "Simulations and measurements of wave propagations in curved road tunnels for signals from GSM base stations," IEEE Trans. Antennas Propag., vol. 54, pp. 2577–2584, Sep. 2006.
[8] S. F. Mahmoud, "Modal propagation of high frequency electromagnetic waves in straight and curved tunnels within the earth," J. Electromagn Waves Applicat., vol. 19, no. 12, pp. 1611–1627, May 2005.
[9] S. F. Mahmoud and J. R. Wait, "Guided electromagnetic waves in a curved rectangular mine tunnel," Radio Sci., vol. 9, no. 5, pp. 567–572, May 1974.
[10] P. Beckmann and A. Spizzichino, The Scattering of Electromagnetic Waves from Rough Surfaces. New York: MacMillan, 1963, pp. 72–81.
[11] M. Moutairou, G. Y. Delisle, H. Aniss, and M. Misson, "Wireless mesh networks performance assessment for confined areas deployment," Int. J. Comput. Sci. Netw. Security, vol. 8, no. 8, pp. 12–23, Aug. 2008.
[12] R. F. Harrington, Time-Harmonic Electromagnetic Fields. New York: Wily-Interscience, 2001.
[13] User's Guide: High Frequency Structure Simulator (HFSS) V. 9.2 Ansoft Corporation, 2003, Ansoft Documentation.

Richard Martelly (M'04) ████████████. ████████ He received the M.S. degree in electrical engineering from Polytechnic University, Brooklyn, in 2004, the B.E. degree in engineering physics from Stevens Institute of Technology, Hoboken, NJ, in 2000, and the Ph.D. degree in electrical engineering from the University of Massachusetts, Amherst, in 2010.

From September 2004 to November 2010, he worked in the Antenna and Propagation Laboratory in the Department of Electrical and Computer Engineering, University of Massachusetts. He is currently with The MITRE Corporation, Bedford, MA.

Ramakrishna Janaswamy (F'03) received the Ph.D. degree in electrical engineering from the University of Massachusetts, Amherst, in 1986.

From August 1986 to May 1987, he was an Assistant Professor of electrical engineering at Wilkes University, Wilkes Barre, PA. From August 1987-August 2001 he was on the faculty of the Department of Electrical and Computer Engineering, Naval Postgraduate School, Monterey, CA. In September 2001, he joined the Department of Electrical and Computer Engineering, University of Massachusetts, Amherst, where he is a currently a Professor. He is the author of the book *Radiowave Propagation and Smart Antennas for Wireless Communications,* (Kluwer Academic Publishers, November 2000) and a contributing author in *Handbook of Antennas in Wireless Communications* (CRC Press, August 2001) and *Encyclopedia of RF and Microwave Engineering* (Wiley, 2005). His research interests include deterministic and stochastic radio wave propagation modeling, analytical and computational electromagnetics, antenna theory and design, and wireless communications.

Prof. Janaswamy is a Fellow of IEEE. He was the recipient of the R. W. P. King Prize Paper Award of the IEEE TRANSACTIONS ON ANTENNAS AND PROPAGATION in 1995. For his services to the IEEE Monterey Bay Subsection, he received the IEEE 3rd Millennium Medal from the Santa Clara Valley Section in 2000. He is an elected member of U.S. National Committee of International Union of Radio Science, Commissions B and F. He served as an Associate Editor of *Radio Science* from January 1999-January 2004 and as an Associate Editor of the IEEE TRANSACTIONS ON VEHICULAR TECHNOLOGY.